

**NASA CONTRACTOR
REPORT**

NASA CR-1968



NASA CR-1968

C. I.

0061306

TECH LIBRARY KAFB, NM

**LOAN COPY: RETURN TO
AFWL (DOUL)
KIRTLAND AFB, N. M.**

**DESIGN AND EXPERIMENTAL RESULTS
OF A HIGHLY LOADED, LOW SOLIDITY,
JET FLAP ROTOR**

by James L. Bettner

Prepared by
GENERAL MOTORS CORPORATION
Indianapolis, Ind. 46206
for Lewis Research Center

NATIONAL AERONAUTICS AND SPACE ADMINISTRATION • WASHINGTON, D. C. • MARCH 1972



0061306

1. Report No. CR-1968	2. Government Accession No.	3. Recipient's Catalog No.	
4. Title and Subtitle DESIGN AND EXPERIMENTAL RESULTS OF A HIGHLY LOADED, LOW SOLIDITY, JET FLAP ROTOR		5. Report Date March 1972	
		6. Performing Organization Code	
7. Author(s) James L. Bettner		8. Performing Organization Report No. EDR 7045	
		10. Work Unit No.	
9. Performing Organization Name and Address General Motors Corporation Indianapolis, Indiana 46206		11. Contract or Grant No. NAS 3-12424	
		13. Type of Report and Period Covered Contractor Report	
12. Sponsoring Agency Name and Address National Aeronautics and Space Administration Washington, D.C. 20546		14. Sponsoring Agency Code	
15. Supplementary Notes Project Manager, Stanley M. Nosek, Fluid System Components Division, NASA Lewis Research Center, Cleveland, Ohio			
16. Abstract The overall performance of a single-stage turbine with a low solidity jet flap rotor blade assembly was tested over a range of cavity pressure ratios, equivalent speeds, and expansion ratios. The rotor blades were designed with negative hub reaction and a mean-line axial chord solidity of 0.922. The results of this investigation are compared with the performance of a modified jet flap rotor blade which was designed to similar velocity diagrams but with a mean-section, axial chord solidity of 1.541. Both rotors were tested with the same stator.			
17. Key Words (Suggested by Author(s)) Turbine aerodynamics High blade loading		18. Distribution Statement Unclassified - unlimited	
19. Security Classif. (of this report) Unclassified	20. Security Classif. (of this page) Unclassified	21. No. of Pages 116	22. Price* \$3.00

Rotor blades - aerodynamic characteristics



TABLE OF CONTENTS

Summary	1
Introduction	2
Symbols	4
Blade Design	7
Aerodynamic Design	7
Velocity Diagrams	7
Solidity Considerations	9
Airfoil Design	10
Blade Cavity Design	12
Mechanical Design	12
Stress Analysis	12
Blade Dynamic and Flutter Analysis	13
Comparison of Jet Flap Blade Designs	13
Apparatus and Instrumentation	14
Calculation Procedure	16
Overall Turbine Performance	16
Rotor Exit Survey	16
Experimental Results	18
Rotor Cavity Pressure Optimization Study	18
Turbine Overall Performance	24
Blade Surface Static Pressure and Rotor Exit Surveys	26
Summary of Results	29
References	31
Appendix	33

LIST OF TABLES

<u>Table</u>	<u>Title</u>	<u>Page</u>
I	Low solidity jet flap rotor design data	39
II	Jet flap blade section coordinates	40
III	Design operating point blade loads	46

LIST OF ILLUSTRATIONS

<u>Figure</u>	<u>Title</u>	<u>Page</u>
1	Jet flap blade velocity triangles with jet on	47
2	Jet flap turbine station nomenclature	48
3	Rotor wheel assembly schematic	49
4	Variation of jet flap blade slot coefficient with slot pressure ratio for lines of slot width	50
5	Jet flap turning and momentum characteristics and jet flap blading nomenclature	51
6	Jet flap blade hub section profile	52
7	Jet flap blade mean section profile	53
8	Jet flap blade tip section profile	54
9	Jet flap blade hub section surface critical velocity ratio with jet off	55
10	Jet flap blade mean section surface critical velocity ratio jet off	56
11	Jet flap blade tip section surface critical velocity ratio with jet off	57
12	Jet flap blade suction surface incompressible shape factor distribution with jet off	58
13	Jet flap blade suction surface wall shear stress distribution with jet off	59
14	Jet flap blade hub section surface critical velocity ratio with jet on	60
15	Jet flap blade mean section surface critical velocity ratio with jet on	61
16	Jet flap blade tip section surface critical velocity ratio with jet on	62
17	Jet flap blade suction surface incompressible shape factor distribution with jet on	63
18	Jet flap blade suction surface wall shear stress distribution with jet on	64
19	Jet flap blade mean section showing cavity geometry . .	65
20	Jet flap blade interior baffle arrangement	66
21	Low solidity jet flap flow distribution as shown by trailing edge tufts	67
22	Reference 2 jet flap flow pattern	68
23	Low solidity jet flap rotor vibrational characteristics .	69
24	Low solidity jet flap airfoil flutter analysis	70
25	Low solidity jet flap rotor assembly	71
26	Top and side views of original and modified jet flap rotor blades	72
27	Original and modified jet flap rotor blade profiles and channels	73

<u>Figure</u>	<u>Title</u>	<u>Page</u>
28	Schematic of test stand air supply system	74
29	Variation of primary flow with expansion ratio and cavity pressure ratio at design speed	75
30	Variation of percent jet flow with expansion ratio and cavity pressure ratio at design speed	76
31	Variation of equivalent jet flow rate with jet cavity- to-exit pressure ratio—comparison of bench test data with design value for low solidity jet flap blade	77
32	Variation of equivalent jet flow with expansion ratio and cavity pressure ratio at design speed	78
33	Variation of corrected torque with expansion ratio and cavity pressure ratio at design speed	79
34	Variation of corrected specific work with expansion ratio and cavity pressure ratio at design speed	80
35	Variation of absolute exit angle with expansion ratio and cavity pressure ratio at design speed	81
36	Radial variation of absolute exit angle with jet cavity pressure ratio at design speed and turbine ex- pansion ratio	82
37	Variation of average absolute exit angle with cavity pressure ratio at design speed and expansion ratio	83
38	Variation of average rotor exit relative gas angle with rotor cavity pressure ratio for two jet flap blade designs at design speed and expan- sion ratio	84
39	Comparison of jet deflection and momentum characteristics with design values for two jet flap blade designs with a relative exit Mach number of 0.7	85
40	Variation of static pressure through turbine with expansion ratio at design speed and zero jet flow	86
41	Variation of static pressure through turbine with expansion ratio at design speed and cavity pressure ratio equal to 0.6	87
42	Variation of static pressure through turbine with expansion ratio at design speed and with cavity pressure ratio equal to 1.0	88

<u>Figure</u>	<u>Title</u>	<u>Page</u>
43	Variation of static pressure through turbine with expansion ratio at design speed and with cavity pressure ratio equal to 1.2	89
44	Comparison of static pressure variation through turbine for two jet flap blade designs	90
45	Variation of thermodynamic efficiency with expansion ratio and cavity pressure ratio at design speed . .	91
46	Variation of base efficiency with expansion ratio and cavity pressure ratio at design speed	92
47	Variation of turbine efficiency with percent jet flow rate for two jet flap designs at design speed and expansion ratio	93
48	Variation of turbine efficiency with cavity pressure ratio for two jet flap designs at design speed and expansion ratio	94
49	Overall performance map for low solidity jet flap blade with 0.025 in. (0.064 cm) jet slot and $P_{T1}/P_{T0} = 1.0$	95
50	Variation of equivalent primary flow with expansion ratio and speed with $P_{T1}/P_{T0} = 1.0$ for low solidity jet flap turbine	96
51	Variation of jet flow with turbine expansion ratio and speed with cavity pressure ratio equal to unity	97
52	Variation of percent equivalent jet flow rate with expansion ratio and speed for low solidity jet flap with $P_{T1}/P_{T0} = 1.0$, $\overline{hb} = 0.025$ in. (0.064 cm)	98
53	Variation of equivalent torque with speed and expansion ratio for low solidity jet flap with $P_{T1}/P_{T0} = 1.0$, $\overline{hb} = 0.025$ in. (0.064 cm)	99
54	Variation of equivalent work with speed and expansion ratio for low solidity jet flap with $P_{T1}/P_{T0} = 1.0$, $\overline{hb} = 0.025$ in. (0.064 cm)	100
55	Variation of thermodynamic efficiency with jet speed ratio for low solidity jet flap turbine with $P_{T1}/P_{T0} = 1.0$, $\overline{hb} = 0.025$ in. (0.064 cm)	101
56	Mean section static pressure distributions on low solidity and modified jet flap blades	102
57	Turbine stage temperature ratio contours for low solidity jet flap blade at design speed and expansion ratio	103

<u>Figure</u>	<u>Title</u>	<u>Page</u>
58	Turbine stage temperature ratio contours for low solidity jet flap turbine at $Re_{TT} = 1.32$, $N/\sqrt{\theta}_{cr} = 65\%$	104
59	Turbine stage total pressure ratio contours for low solidity jet flap blade at design speed and ex- pansion ratio	105
60	Turbine stage total pressure ratio contours for low solidity jet flap blade at $Re_{TT} = 1.32$, $N/\sqrt{\theta}_{cr}$ $= 65\%$	106
61	Total-to-total efficiency contours—100% speed, $Re_{TT} = 2.01$	107
62	Total-to-total efficiency contours—65% speed, $Re_{TT} = 1.32$	108
63	Comparison of efficiency (based on temperature) for the modified and low solidity jet flap turbines with $P_{TI}/P_{T0} = 1.0$	109

DESIGN AND EXPERIMENTAL RESULTS OF A HIGHLY LOADED, LOW SOLIDITY, JET FLAP ROTOR

by

James L. Bettner

Detroit Diesel Allison, Division of General Motors

SUMMARY

A performance test of a single-stage turbine with a low solidity jet flap rotor blade was made over a range of equivalent speeds and expansion ratios. The mean section axial chord solidity was 0.922. One jet slot size of 0.025 in. (0.064 cm) was investigated. A rotor cavity pressure optimization test was conducted to determine the effect of jet flow on turbine performance. Based on these tests, a rotor cavity pressure ratio, P_{T1}/P_{T0} , of unity was selected and the overall turbine performance map was determined. The results of these tests were compared with the performance of a higher solidity modified jet flap blade which incorporated a 0.038 in. (0.097 cm) jet slot. The modified jet flap blade mean section axial chord solidity was 1.541. The low solidity and modified jet flap blades were designed to satisfy similar sets of negative hub reaction velocity diagrams. Both jet flap blades were tested with the same stator.

The low solidity jet flap performance map test produced a thermodynamic efficiency (which considers the ideal power of both the primary and jet flow stream) that was 83.4% when operating at design speed and expansion ratio and unity cavity pressure ratio. The design thermodynamic efficiency at these operating conditions was 86.7%. The thermodynamic efficiency of the modified jet flap blade when operating under the same circumstances was 85.4%. The low solidity jet flap blade developed a greater degree of negative hub reaction than the modified jet flap blade. At design speed and expansion ratio the hub reaction changed from negative to impulse at 3.8% jet flow for the modified jet flap. At the same operating point conditions, the low solidity jet flap blade hub reaction was negative for all jet flows investigated. The jet flow rate ranged up to 3.4% of the primary flow.

Blade surface static pressure measurements and rotor exit surveys of total pressure, total temperature, and gas angle showed that the decrease in performance, relative to the higher solidity modified jet flap blade was primarily due to high losses generated by suction surface flow separation in the outer half portion of the blade.

INTRODUCTION

The NASA Lewis Research Center has begun a series of experimental investigations of several advanced concepts designed to increase blade loading while maintaining good turbine performance. One of these concepts is the jet flap blade. The jet flap blade uses a high velocity jet which emanates from the trailing edge pressure surface. The interaction of this jet with the mainstream flow effects an acceleration on the suction surface and a deceleration on the pressure surface in the aft region of the airfoil. The accelerated flow on the suction surface reduces the amount of diffusion, thereby eliminating or at least delaying, flow separation. The net effect is to produce a turbine blade capable of greater work capacity than an unblown or conventional airfoil.

The design of the first jet flap rotor blade of this series is presented in Reference 1. That blade design had hub, mean, and tip axial chord solidity values of 2.188, 1.802, and 1.532, respectively. The performance results for two jet slot sizes—including a comparison with a higher solidity plain blade—were reported in Reference 2. At design speed and expansion ratio the efficiency for the small and large slots was 90.1 and 91.4%, respectively. This efficiency (called base efficiency) was computed using the primary flow only. The comparable plain blade efficiency was 88.4%.

The turbine performance at lower values of rotor blade axial chord solidity was examined. The solidity was reduced about 14.5% by removing metal from the blade leading edge region. The resulting solidity values were 1.871, 1.541, and 1.310 for the hub, mean, and tip, respectively. The experimental results are presented in Reference 3. The base efficiency for this modified jet flap blade with large slot size at design speed and expansion ratio was 90.5%.

In addition to this series of jet flap rotor tests, a companion series of low solidity, impulse-type, jet flap stator tests was conducted and is summarized in Reference 4. These latter results also demonstrated that the jet flap concept could substantially increase blade loading capacity.

In view of these generally positive rotor and stator results for the jet flap blade, a jet flap rotor having much lower solidity than the two previous jet flap rotors was designed and tested. The design values of axial chord solidity for this rotor (referred to hereafter as the low solidity jet flap) were 1.324, 0.922, and 0.641 for the hub, mean, and tip sections. This report presents the design and test results for the low solidity jet flap rotor blade.

The low solidity jet flap rotor was tested in the same single-stage test rig previously used in the series of highly loaded blade tests. The design

jet slot size and jet flow rate were 0.025 in. (0.064 cm) and 2.30%, respectively. A cavity pressure optimization study was first performed over a range of turbine expansion ratios at design speed to determine the effect of rotor cavity pressure on turbine performance. The amount of jet flow ranged from zero to 3.4% of the primary (stator in) flow rate. Cavity conditions were then fixed at $P_{T_I}/P_{T_0} = T_{T_I}/T_{T_0} = 1.0$ and a performance map was obtained from 55 to 110% design equivalent speeds over a range of expansion ratios, Re_{TT} , from 1.3 to 2.3. Rotor exit surveys and blade surface static pressure measurements were taken at (1) design speed and expansion ratio, and (2) 65% design equivalent speed and $Re_{TT} = 1.3$. The rotor exit surveys consisted of circumferential traverses with a combination total pressure, temperature, and yaw angle probe at constant radii to map the flow characteristics at the rotor trailing edge. The test results were compared with the modified jet flap rotor performance results.

All testing was conducted while operating the test rig with inlet conditions of approximately 2.7 atm absolute pressure and 650°R (361°K) temperature.

SYMBOLS

C_F	Flow coefficient (Figure 3)
C_V	Velocity coefficient
C_j	Jet momentum coefficient, $C_j = \dot{m}_j U_j / (\dot{m}_p + \dot{m}_j) W_3$
C_x	Axial chord, in. (cm)
d_l	Leading edge diameter, in. (cm)
d_t	Trailing edge diameter, in. (cm)
g_c	Gravitational constant, $32.174 \frac{\text{lb}_m \text{ ft}}{\text{lb}_f \text{ sec}^2} , \left(1 \frac{\text{kg m}}{\text{N sec}^2} \right)$
$\overline{h_b}$	Jet slot size, in. (cm)
H_i	Incompressible shape factor
ΔH	Specific work output, Btu/lb (joule/kg)
l	Blade length, in. (cm)
L	Lift, $\text{lb}_f/\text{in.}$ (N/cm)
\dot{m}	Mass flow rate, lb/sec (kg/sec)
M	Mach number
N	Rotational speed, rpm (rad/sec)
P	Pressure, $\text{lb}/\text{in.}^2$ (N/m ²)
r	Radial location in. (cm)
R	Reaction defined as $1 - (W_1^2 / W_3^2)$
R_e	Expansion ratio
s	Blade spacing, in. (cm)
t	Throat dimension, in. (cm)
T	Temperature, °R (°K)
U	Blade tangential velocity, ft/sec (m/sec)
U_j	Jet velocity, ft/sec (m/sec)
V	Absolute gas velocity, ft/sec (m/sec)
W	Relative gas velocity, ft/sec (m/sec)
X	Axial coordinate, in. (cm)
Y	Tangential coordinate, in. (cm)
α	Absolute gas angle measured from tangential, degrees
β	Relative gas angle measured from tangential, degrees
γ	Ratio of specific heats
Δ	Change in variable
δ_I	Ratio of rotor inlet cavity pressure to standard sea level conditions
δ_0	Ratio of turbine inlet air total pressure to standard sea level conditions
ϵ	Function of γ defined as $\frac{\gamma^* \left(\frac{\gamma+1}{2} \right)^{\gamma/(\gamma-1)}}{\gamma \left(\frac{\gamma^*+1}{2} \right)^{\gamma^*/(\gamma^*-1)}}$

η_T	Adiabatic efficiency defined as the ratio of turbine work based on torque, weight flow, and speed measurements to the ideal work based on inlet total temperature, and inlet and outlet total pressure both defined as sum of static pressure plus pressure corresponding to the gas velocity.
η_t	Adiabatic efficiency defined as the ratio of turbine work based on measured inlet and exit total temperature to ideal work based on measured inlet total temperature and pressure and measured exit total pressure
θ	Jet deflection angle, degrees
θ_{cr}	Squared ratio of critical velocity at turbine inlet temperature to critical velocity at standard sea level temperature.
v	Ratio of blade speed to isentropic gas velocity based on inlet total temperature and pressure and exit static pressure, U_m/V'
ρ	Density, lb/ft ³ (kg/m ³)
σ_x	Blade axial chord solidity defined as C_x/s
ψ	Angle measured from axial, degrees
ψ_t	Compressible tangential lift coefficient defined as
	$\frac{s}{C_x} \left(\frac{\rho_{st3} V_{x3} \Delta V_{u1-3}}{P_{T1 \text{ rel}} - P_{st3}} \right)$
τ	Jet efflux angle, degrees or torque, ft-lb (N-m)
τ_w	Wall shear stress, psi (N/cm ²)

Subscripts

0	Station at stator inlet (all stations are shown in Figure 2)
1	Station at free-stream conditions between stator and rotor
2	Station at outlet of rotor just downstream of trailing edge
3	Station downstream of turbine
cr	Condition at Mach number of unity
h	Hub section
I	Jet flow inlet station (rotor cavity)
j	Jet flow
m	Mean section
p	Primary flow
rel	Relative to moving blade
st	Static
T	Total
T T	Total-to-total
T-S	Total-to-static
t	Tip Section
th	Throat

u	Tangential direction
x	Axial direction
wo/j	Without jet
w/j	With jet

Superscripts

'	Ideal or isentropic condition
-	Average of variable
*	Standard condition

BLADE DESIGN

AERODYNAMIC DESIGN

The objective of this program was to design and test a single-stage turbine rotor having very highly loaded, low solidity blades. This high loading was to be achieved without flow separation by using jet flap airfoils.

The test rig, including the stator blade row, used with the low solidity jet flap rotor was developed in the program described in Reference 1. This unit has a 30 in. (76.2 cm) tip diameter and a constant hub-tip radius ratio of 0.7. The overall design point characteristics were:

● Equivalent specific work output, $\Delta H/\theta_{cr}$	20.0 Btu/lb	$(46.5 \times 10^3 \frac{\text{Joule}}{\text{kg}})$
● Equivalent weight flow, $(\dot{m}_p \sqrt{\theta_{cr}} \epsilon)/\delta_o$	47.7 lb/sec	(21.6 kg/sec)
● Equivalent blade tip speed, $U_t/\sqrt{\theta_{cr}}$	610.0 ft/sec	(186 m/sec)
● Pressure ratio, P_{T0}/P_{T3}	2.01	
● Total thermodynamic efficiency, η_T	86.7%	

Velocity Diagrams

In the work of Reference 5, new, nearly zero exit whirl velocity diagrams for the test rig flowpath were computed using the stator exit total pressure survey results from Reference 6. The velocity diagrams for the low solidity jet flap rotor test were to be identical to those of Reference 5 only modified to include the addition of the jet flow. The Reference 5 total-to-total thermodynamic efficiency was 88.7%. This value of efficiency was altered for the present investigation to account for the addition of the jet flow. When the ideal power of the design jet flow rate, $\dot{m}_j/\dot{m}_p = 2.3\%$, was considered, the 88.7% value of thermodynamic efficiency was reduced to 86.7%. The diagrams evolved are shown in Figure 1. Station nomenclature is presented in Figure 2.

The number of blades for the rotor was chosen to be 38, half the number used in previous jet flap rotor designs. This number of blades would be sufficient to produce very highly loaded individual blades. Also, there were 38 channels on the front face of the wheel which ducted the jet flow to the bases of the rotor blades. These channels are shown in detail in Figure 3. Using 38 blades on the wheel ensured uniform blade-to-blade jet flow distribution into each blade base.

Because of the low number of blades, low jet flows were incorporated in the design to keep the velocities low in the blade cavity. Therefore, a small slot size of 0.025 in. (0.064 cm) was selected. The design jet supply pressure as measured in the rotor cavity was limited to the turbine inlet total pressure. With 38 blades and the 0.025 in. (0.064 cm) slot size, the design jet flow was calculated to be 2.30% of the stator inlet (primary) flow. The flow coefficient

data obtained as part of the investigation reported in Reference 2 (reproduced in Figure 4) was used in calculating the jet flow. The blade cavity pressure was assumed to be the rotor cavity pressure plus the increase in pressure because of centrifugal effects. For example, with a rotor cavity pressure of 14.696 psi ($101.325 \times 10^3 \text{ N/m}^2$), the pressure in the blade cavity at the mean section would be 17.041 psi ($115.493 \times 10^3 \text{ N/m}^2$). The jet exhaust pressure was assumed to be the downstream static pressure (Station 3). The jet flap blade airfoil design procedure then was one of assuming that the conditions of 38 blades, 0.025 in. (0.064 cm) jet slot and 2.30% jet flow would be adequate to prevent flow separation on blading surfaces and thereby satisfy the computed velocity diagrams. If the design procedure showed that flow separation probably would occur then either (1) the slot size, or (2) the amount of jet flow, or both (1) and (2) would have to be increased. If the procedure showed the assumed slot size and flow conditions to be too conservative the assumed condition would be reduced in either slot size or jet flow requirements.

The complete velocity diagram/throat sizing calculation procedure is described in detail in the Appendix. Briefly, the calculation procedure consisted of the simultaneous satisfaction of continuity and experimental jet deflection characteristics. The following sets of equations satisfy the turning requirements.

Set A

$$\theta_A = \beta_{3_{wo/j}} - \beta_{3_{w/j}}$$

$$\text{but } \beta_{3_{wo/j}} = \beta_{2_{wo/j}}$$

$$\therefore \theta_A = \beta_{2_{wo/j}} - \beta_{3_{w/j}}$$

$$W_2 = W_{u_2} / \cos \beta_2$$

$$(\dot{m}/\ell)_2 = \rho_{st_2} W_{x_2} s$$

$$C_j = (\dot{m}_j/\ell) U_j / \left\{ [(\dot{m}_p/\ell)_2 + (\dot{m}_j/\ell)] W_3 \right\}$$

Set B

$$\theta_B = F(C_j, \tau)$$

The functional relationship on Set B is given by an experimentally derived set (from Reference 2) of curves that are shown in Figure 5. These curves describe the deflection, θ , with respect to zero jet flow, of the downstream flow that is accomplished when the jet is activated. The dependency of deflection on jet efflux angle, τ , is also shown in Figure 5. The theoretical work of Reference 7 showed that the jet flap was most effective as a high lift device when $\tau = 90$ degrees. Further, the jet flap blade designs of References 2 and 3 incorporated jet efflux angle designs of $\tau = 90$ degrees. Based on this background, a jet efflux angle value of 90 degrees was selected for the current design. The jet efflux angle is so measured that $\tau = 90$ degrees results in the jet effluxing along the throat line.

The downstream tangential velocity component was known from the work requirement, so the downstream velocity triangles were derived by satisfying continuity with the sum of primary and jet mass flow rates. As a result of the presence of the jet, less gas turning was required of the jet flap airfoil than a conventional airfoil of equivalent loading. An initial value was assumed for this reduced turning requirement and this, in turn, fixed the tangential velocity component at the blade row exit. Thus, for a given jet efflux angle (gas turning split between the airfoil and jet) and jet momentum coefficient, there was a unique solution to the previously listed equations so that $\theta_A = \theta_B$. Continuity was then checked at the blade row exit, and, if adjustment was needed, a new value was assumed on the blade turning requirement until both continuity and the velocity diagram total turning requirements were satisfied.

The blade throats were designed by satisfying continuity and conserving the tangential component of momentum from throat to blade exit. The exit velocity triangles were calculated reflecting no jet flow addition. This was accomplished by retaining the exit tangential velocity component from the previous calculation and satisfying continuity with the primary flow. The throat conditions are then developed from these exit velocity triangles. It was assumed for these calculations that the blade had no turning from the throat to the exit. When the throat velocity diagrams were determined, the throat was computed from $t = (s \sin \beta_{th}) - d_t$. Hub, mean, and tip section velocity diagrams (with jet on) for the assumed conditions of 0.025 in. (0.064 cm) jet slot size, 2.30% jet flow, and a trailing edge diameter of 0.120 in. (0.305 cm) were presented in Figure 1. Pertinent design data for the jet flap rotor with these diagrams are listed in Table I.

Solidity Considerations

The objective of this research program was to examine the performance of a very highly loaded jet flap rotor blade. High loading is synonymous with large values of tangential lift coefficient, ψ_t , which is essentially a compressible form of Zweifel's (Reference 8) actual-to-ideal loading coefficient and defined for a conventional blade as

$$\psi_t = \frac{s}{C_x} \left[\frac{\rho_{st3} V_{x3} \Delta V_{u1-3}}{P_{T1 \text{ rel}} - P_{st3}} \right]$$

The same definition will be retained herein even though it is the blade plus the jet that is required to achieve the required velocity diagrams.

The experimental results of Reference 4 and 9 have shown that low solidity jet flap stators can maintain fairly high levels of performance. Based on the velocity diagrams of Figure 1—a maximum hub section axial chord dimension of 2.3 in. (5.842 cm), and 38 blades—the hub section ψ_t was 1.482. The axial chord was then tapered radially to ensure a satisfactory distribution of blade

stress and to produce mean and tip section ψ_t values of about 1.4. Mean and tip section and axial chords of 1.945 in. (4.940 cm) and 1.59 in. (4.038 cm) produced ψ_t values of 1.434 and 1.340, respectively. The corresponding hub, mean, and tip section values of solidity were 1.324, 0.922, and 0.641, respectively. These data are listed in Table I.

Airfoil Design

The blade section profile shapes were determined by iterating with the radial section geometry without jet flow until satisfactory surface velocity distributions were obtained. The surface velocities were computed by the two-dimensional flow methods described in Reference 10. Even though the flow separation from the aft suction surface was expected without jet flow, the airfoil geometry was varied to (1) keep the velocity levels on the pressure surface as low as possible (this would help to avoid unnecessarily high velocity levels on the suction surface), (2) avoid having velocity spikes and large decelerations on the suction surface, and (3) keeping the loading levels high as far back on the blade as possible. Resulting hub, mean, and tip section profiles are presented in Figures 6, 7, and 8 with the respective surface velocity predictions illustrated in Figures 9, 10, and 11. Blade section coordinates are listed in Table II.

The effect of the free-stream static pressure distribution on the behavior of the suction surface boundary layer was investigated by using the calculation techniques of both Truckenbrodt (Reference 11) and McNally (Reference 12). The separation criteria for the Truckenbrodt method was when the incompressible shape factor, H_i , attained a value between 1.8 and 2.2 while for the McNally method the separation criteria was when the wall shear stress, τ_w , went to zero. Hub, mean, and tip section axial distribution of the Truckenbrodt H_i shape factor and the McNally wall shear stress distribution is presented in Figures 12 and 13, respectively. Flow separation was predicted to occur in the aft suction surface at all three of the radial stations investigated. The locations of flow separation from the suction surface as predicted by both the Truckenbrodt and McNally methods are shown on the section profiles and velocity distribution of Figures 6 through 11. Both methods predict flow separation to occur at about the same axial location for each radial section.

The jet flap was added to the blade trailing edge to prevent flow separation by eliminating the diffusion on the suction surface. The general shape of the jet contour was determined by satisfying the condition that the change in momentum across the blade row in the tangential direction as computed by the velocity diagrams of Figure 1 was equal to the lift of the airfoil. The lift was computed as the sum of the static pressure force on the blade and the change in momentum of the jet in the tangential direction. This may be expressed in equation form as:

$$L = \dot{m}_p W_{u_1} - \dot{m}_3 W_{u_3} = \int_0^{C_x} \Delta P_{st_u} dx + C_F \rho_{st} U_j^2 \bar{h} \cos \alpha_j$$

where

$$\dot{m}_3 = \dot{m}_p + \dot{m}_j$$

and

$$\dot{m}_p W_{u_1} - \dot{m}_3 W_{u_3} = \left[(\rho_{st} W_x)_1 W_{u_1} - (\rho_{st} W_x)_3 W_{u_3} \right] \frac{s}{g_c 144}$$

Thus

$$\int_0^{C_x} \Delta P_{st_u} dx = \left[(\rho_{st} W_x W_u)_1 - (\rho_{st} W_x W_u)_3 \right] \frac{s}{g_c 144} - C_F \rho_{st_j} U_j^2 \bar{h} \cos \alpha_j$$

The two terms on the right-hand side of the equation were computed for the hub, mean, and tip sections. These computations are as follows:

$$\left[(\rho_{st} W_x W_u)_1 - (\rho_{st} W_x W_u)_3 \right] \frac{s}{g_c 144} \quad C_F \rho_{st} U_j^2 \bar{h} \cos \alpha_j \quad \int_0^{C_x} \Delta P_{st_u} dx$$

hub	lb _f /in. (N/cm)	7.450 (13.047)	0.295 (0.517)	7.155 (12.530)
mean	lb _f /in. (N/cm)	8.382 (14.679)	0.290 (0.508)	8.092 (14.171)
tip	lb _f /in. (N/cm)	8.339 (14.604)	0.297 (0.520)	8.042 (14.084)

The jet stream was assumed to be approximately parabolic in shape (Figure 5), emanating at the jet flap slot. The downstream direction of the jet stream was set equal to the β_3 as computed by the velocity diagram of Figure 1. The jet stream was considered to behave as a solid flow boundary. The approximate parabolic jet shape was maintained, but the exact position of jet stream line relative to the airfoils was iterated upon until the integral of the static pressure distribution around the airfoil as predicted by the methods of Reference 10 matched that in the preceding list. Satisfaction of this requirement fixed the jet shape and, hence, the surface velocity distribution around the blade with the jet on. If the subsequent boundary layer analyses showed that this surface velocity distribution would not separate, then the design was considered complete. If separation was predicted to occur, then the jet momentum would have to be increased and the design procedure repeated, starting back with assuming new values of jet slot size and jet flow rate and computing a new set of velocity diagrams.

The hub, mean, and tip surface velocity distributions resulting from iterating with jet contour to satisfy the aforementioned blade static pressure requirements are shown in Figures 14, 15, and 16. By comparison with the velocity distributions without the jet (Figures 9, 10, and 11), it can be seen that much of the suction surface diffusion has been eliminated by the presence of the jet flap.

Subsequent boundary layer analyses (using the Truckenbrodt and McNally methods) are presented in Figures 17 and 18. Both procedures predicted that flow separation would not occur when the jet flap was activated.

Blade Cavity Design

The rotor blade cavity was defined by having a wall thickness of slightly over 0.060 in. (0.152 cm) over most of the airfoil. This thickness tapered to about 0.030 in. (0.076 cm) in the very aft trailing edge region. These dimensional features are shown in Figure 19 for the mean section.

The blade was supplied with jet flow through the hub section. The flow area at this section was 0.45 in.² (2.90 cm²). With design jet flow the Mach number at the hub section was estimated to be only 0.10.

The work of Reference 2 shows there was an unsatisfactory distribution of the jet flow along the radial span of the jet slot. The jet flow could not negotiate the abrupt radial-to-axial turn at the hub section, resulting in a deficiency of jet flow in the hub region. To overcome this difficulty in the low solidity blade design, a series of turning vanes was incorporated in the blade cavity. This feature is shown in Figure 20. The turning vanes were 0.050 in. (0.127 cm) thick and were placed so as not to disrupt the flow in the various radial-circumferential planes of the rotor exit survey. These vanes proved to be quite satisfactory in turning the flow from the radial to an axial direction. This is demonstrated by comparing the flow distribution photographs for the current low solidity jet flap blade (Figure 21) and the jet flap blade of Reference 2 (Figure 22). The flow distribution in the hub region of the low solidity jet flap blade (with internal guide vanes) was much improved over the conditions in the hub region of the Reference 2 blade which had no internal guide vanes.

MECHANICAL DESIGN

Stress Analysis

A stress analysis was made of the blade geometry subjected to the turbine design point operating conditions. Axial and tangential forces acting on the blade are presented in Table III. These forces were determined from the surface static pressure distributions calculated about the airfoil at the design operating point. The blades were investment cast from Inco 718 material.

The blades were stacked on one edge of the jet flap slot so that the Elox slot cutting operation would be facilitated with a straight cutting tool.

The stress analysis showed that the blade stacked in this manner and operating at the design point conditions would have the maximum stress located at the hub section. The maximum stress was the sum of 11,279 psi (7776.5 N/cm²) caused by centrifugal loading and 13,000 psi (8963.1 N/cm²) as a result of gas bending loads. The stress analysis further predicted that the life of the blade should be infinite when subjected to these stress conditions.

Blade Dynamic and Flutter Analysis

Figure 23 shows the vibrational characteristics of the low solidity jet flap blade. These results show that several modes of blade vibration could be excited by the test rig engine orders in the turbine operating speed range. Testing, however, revealed that the mechanical characteristics of the blades were such that the excitation was sufficiently damped out at most operating points. Excessive vibrational stress was encountered at one low speed, moderately high expansion ratio operating point.

The blade flutter was also considered during the mechanical design of the blade. The prime variables which affect blade flutter are (1) the angle (i. e., incidence) at which the fluid particles strike the blade leading edge region, and (2) their kinetic energy. Figure 24 presents the envelope of incidence-relative velocity to which the blade was subjected. The flutter boundaries were predicted to lie at large distances from the incidence-velocity envelope. These results indicate, along with experimental confirmation, that the low solidity jet flap blade was stable in both stalled and unstalled flutter.

Comparison of Jet Flap Blade Designs

The performance of the low solidity jet flap blade will be compared with that of the modified jet flap blade. The rotor assembly with the low solidity jet flap blades is shown in Figure 25. Original and modified jet flap blades are shown in Figure 26. The modified blade was formed by removing metal from the leading edge region of the original jet flap blade. This is demonstrated in Figure 27 where it is shown that the axial chord dimension was reduced by 0.276 in. (0.701 cm) at all radial sections in the leading edge region. The modified jet flap blade had about 62% more solidity than did the low solidity jet flap blade. The design value of jet slot size and flow rate was 0.025 in. (0.064 cm) and 2.30% for the low solidity blade and 0.038 in. (0.097 cm) and 5% for the modified jet flap blade, respectively.

APPARATUS AND INSTRUMENTATION

The apparatus used in this investigation is described in Reference 1. It consisted of a single-stage cold air turbine test rig, suitable housings to provide uniform inlet flow conditions, and a dynamometer to absorb and measure the turbine power output. A schematic of the test rig and air supply facility is shown in Figure 28. Air is supplied at approximately 3-atm pressure and a temperature of $\sim 700^{\circ}\text{R}$ ($\sim 389^{\circ}\text{K}$). The inlet pressure is controlled by the separate air compressor supply and/or by a throttle valve in the inlet supply line. The turbine expansion ratio is controlled by a throttle valve in the exhaust system duct.

The turbine test rig instrumentation is also described in detail in Reference 1. The airflow is measured using a Bailey adjustable orifice which is calibrated with an ASME flow nozzle. The turbine power output is absorbed by two Dynamic dry-gap eddy current brakes. The torque of each dynamometer is measured separately by a dual output strain gage load cell connected in tension to the dynamometer torque arm.

Measurements of total temperature and total pressure were made at stations 0 and 3 (Figure 2). Turbine inlet temperature (Station 0) was measured with 20 iron-constantan thermocouples arranged five to a rake. The sensing elements were located on centers of equal annular areas, and the rakes were spaced 90 degrees apart. Four Kiel-type total pressure probes, also located at the inlet, were used to establish the desired inlet total pressure. The turbine exit measuring station (Station 3) was instrumented with five combination total pressure, total temperature, self-aligning flow angle probes. The sensing elements of the five combination probes were located at the center of five equal annular areas.

Static pressures were measured with four taps on both the inner and outer walls located around the annulus at Stations 0, 1, 2, and 3. The stator outlet (Station 1) static pressure taps were centrally located on the projected stator flow passage.

The rotor mean section was instrumented with six suction surface and three pressure surface static pressure taps. The axial location of the taps is indicated on the surface velocity distribution plots of Figures 10 and 15. In addition, one pressure tap was also located in the blade cavity at the mean section. The taps were constructed of 0.032-in. (0.081-cm) OD/0.020-in. (0.051-cm) ID tubing. The static pressures on the surface of the rotating blades were measured by a Scanivalve Company Model 24D3-1 rotating pressure switch located in the aft center position of the rotor wheel. Pressure measurements were transmitted from the rotating pressure switch to a stationary transducer through a rotating-to-stationary seal. The electrical signal for indexing the rotating pressure switch was transmitted through a slip ring assembly mounted on the downstream end of the rotor wheel shaft.

A rotor exit survey was performed approximately 0.125 in. (0.318 cm) axially downstream of the rotor blade trailing edge (Station 2). Total pressure, total temperature, and flow angle were measured at seven radii from hub to tip for a circumferential arc of 22 degrees. The measurements were taken concurrently with a single combination probe.

CALCULATION PROCEDURE

OVERALL TURBINE PERFORMANCE

The turbine performance was rated on the basis of the ratio of inlet total pressure and rotor exit total pressure. The inlet total pressure at Station 0 was calculated from continuity by using the average of the 20 measured total temperatures, the average of the hub and tip static pressures, the mass flow rate, and the inlet annulus area. The flow was assumed to be axial. The exit total pressure at Station 3 was also calculated from continuity using the mass flow rate, the annulus area, the average of the hub and tip static pressures, the average flow angle, and the total temperature. The total temperature was calculated from the enthalpy drop which, in turn, was based on the measured airflow, torque, and speed.

Two efficiencies were defined: base efficiency and thermodynamic efficiency. The base efficiency was calculated as a ratio of the actual power developed as obtained from torque, and rotor speed measurements to the ideal power as obtained from the primary mass flow rate, inlet total temperature, and the associated calculated expansion ratio, i. e. ,

$$\eta_{T_{base}} = \frac{\tau N}{\dot{m}_p H'_{P0-3}}$$

The thermodynamic efficiency charged the turbine for the available power of the jet flow, i. e. ,

$$\eta_{T_{thermo}} = \frac{\tau N}{\dot{m}_p \Delta H'_{P0-3} + \dot{m}_j \Delta H'_{jI-3}}$$

ROTOR EXIT SURVEY

The performance of the turbine as described by a rotor exit survey at the design point condition was based on measured expansion ratio, inlet temperature, and exit temperature. The measured expansion ratio was based on the average total pressure indicated by the four inlet Kiel probes and the exit total pressure measured by the survey probe. The inlet total temperature was the average temperature of the 20 inlet thermocouples; the exit total temperature was measured by the thermocouple on the survey probe. These thermocouples were corrected for Mach number based on a

linear variation of hub and tip static pressure and the measured total pressure. The isentropic work of the turbine was based on the measured inlet temperature and measured total pressure ratio. The actual work was the difference of the enthalpies associated with the measured inlet and exit temperatures. The efficiency at each station in the survey was the ratio of the actual work to the isentropic work, i.e.,

$$\eta_t = \frac{T_{T_0} - T_{T_3}}{T_{T_0} \left[1 - \left(\frac{P_{T_3}}{P_{T_0}} \right)^{\frac{\gamma-1}{\gamma}} \right]}$$

EXPERIMENTAL RESULTS

The low solidity jet flap rotor was tested in the same single-stage rig that was used to test the modified jet flap rotor blade reported in Reference 3. The experimental program was divided into two phases. The first phase was a rotor cavity pressure optimization study whose objectives were to (1) examine the effect of rotor cavity pressures on turbine performance and (2) provide an optimum value of cavity pressure setting to use in determining the turbine performance at off-design speeds and expansion ratios. The rotor cavity temperature was held at turbine inlet total temperature, (i. e., $T_{T_I}/T_{T_0} = 1.0$). The second phase of testing consisted of holding the cavity temperature and pressure at fixed values and obtaining a performance map at off-design values of speeds and expansion ratios. Rotor exit surveys of temperature, pressure, and angle and blade surface static pressure measurements were conducted at (1) design speed and expansion ratio and (2) 65% design equivalent speed and $Re_{TT} = 1.32$.

Rotor Cavity Pressure Optimization Study

The rotor cavity pressure optimization study was conducted at design equivalent speed, $N/\sqrt{\theta}_{cr} = 4660$ rpm (487.99 rad/sec), and jet-to-inlet total pressure ratios, P_{T_I}/P_{T_0} , of 0.6, 1.0, 1.2, and also zero jet flow. At each cavity pressure ratio the turbine expansion ratio, P_{T_0}/P_{T_3} was varied from about 1.7 to about 2.4. Also data were obtained at $P_{T_I}/P_{T_0} = 1.1$ and 1.3 at design expansion ratio of $P_{T_0}/P_{T_3} = 2.01$.

Figure 29 shows the equivalent primary flow variation with turbine expansion ratio and cavity pressure level. The design value of equivalent flow was 47.7 lb/sec (21.6 kg/sec) at $Re_{TT} = 2.01$ and $P_{T_I}/P_{T_0} = 1.0$. An experimental value of 47.4 lb/sec (21.5 kg/sec) was obtained. Figure 29 shows that the primary flow level decreased as the cavity pressure level was increased. This is the result of the jet flow progressively reducing throat area available to the primary flow as the cavity pressure was increased. The choked level variation of primary flow from zero jet flow to $P_{T_I}/P_{T_0} = 1.2$ was slightly under 1%.

Figure 30 shows that the amount of jet flow increased to about 3.4% of the primary flow as the cavity pressure ratio was increased to a value of 1.2. The percentage of jet flow, \dot{m}_j/\dot{m}_p was nearly constant with turbine expansion ratios for the jet rotor cavity pressure ratio investigated. The jet slot passed more flow than design in that 2.7% was measured at $Re_{TT} = 2.01$ whereas the design value was 2.3%. The experimental jet slot flow coefficient was larger than the design value. Figure 31 shows flow characteristics for this jet slot design and the results of bench tests on individual blades used to determine the flow characteristics of the slot. The slot was passing slightly more than design values of equivalent jet

flow. Figure 32 shows the choking characteristics of the 0.025 in. (0.064 cm) jet slot and that the slot was choked above P_{T_I}/P_{T_0} values of about 1.1. Figure 32 also shows that the slot was passing slightly more than design jet flow rate. At design turbine expansion ratio and cavity pressure ratio, 1.28 lb/sec (0.58 kg/sec) was measured whereas the design value was only 1.097 lb/sec (0.498 kg/sec).

Figures 33 and 34 present the corrected torque and work characteristics of the low solidity jet flap turbine as a function of cavity and turbine pressure ratios. The torque characteristics show that over the range of expansion ratios investigated, the turbine continued to develop shaft torque, thus the condition of limiting loading was not imminent. These curves do indicate, however, that the level of performance was less than design since neither design values of work nor torque was obtained at design expansion ratio. For $P_{T_I}/P_{T_0} = 1.0$, Re_{TT} had to be increased to 2.1 before design torque and work were achieved. As will be explained later, this condition is probably caused by flow separation from the blading surface with reduced gas turning and subsequent loss in total pressure.

The effect of rotor cavity pressure on the absolute angle turning characteristics for the low solidity blade are shown in Figure 35. These angle data represent the average reading of the five yaw probes located in measurement plane 3 (Figure 2). The design velocity diagrams used a cavity pressure ratio of 1.0 to achieve a near axial (i. e., $\alpha \approx 90$ degrees) average exit angle. Figure 35 shows that without the jet on the mainstream, flow was underturned (e. g., at design $Re_{TT} = 2.01$, $\alpha \approx 72$ degrees which is 18 degrees from axial). Because of flow separation from the suction surface, the value of the absolute exit gas angle was expected to be substantially less than axial (90 degrees) when the jet was turned off. As the jet strength was to be progressively increased (by increasing P_{T_I}/P_{T_0}), flow separation would be delayed to further aft on the suction surface. At $P_{T_I}/P_{T_0} = 1.0$, flow separation was to have been eliminated and the design velocity diagrams achieved. Experimentally, however, with the design value of $P_{T_I}/P_{T_0} = 1.0$, the turning was not quite sufficient to produce the design angle at design expansion ratio. The angle was 86 degrees which was still 4 degrees short of being axial.

The turning characteristics of the low solidity jet flap rotor are further demonstrated in Figures 36 through 39. Figure 36 shows the individual station 3 probe angle measurements as a function of jet rotor cavity pressure ratio at design speed and turbine expansion ratio. Design values at the hub, mean, and tip sections are also shown. The trend of approaching the axial direction with increasing cavity pressure is shown in Figure 36. The interesting result, though, is that the flow was overturned (turned past axial) in the hub region and substantially underturned (relative to design)

in the outer half radial span of the blade. The blade solidity was lowest and loading requirements were highest in the outer portion of the blade. The observed underturning in this region was probably caused by the jet flap being unable to prevent flow separation from the suction surface.

In Figure 37 the average absolute angle information at design total-to-static expansion ratio is shown as a function of cavity pressure ratio. A value of $P_{T_I}/P_{T_0} \approx 1.2$ was required to produce an axial angle. Figure 37 data were used along with speed and flow field measurements to compute the relative exit angle (β_3) variation with P_{T_I}/P_{T_0} . These results for the low solidity jet flap rotor along with those for the modified jet flap blade are shown in Figure 38. These results demonstrate how the relative angle decreases (i.e., increased gas turning) with increasing cavity pressure. The shape of the β_3 versus P_{T_I}/P_{T_0} curve is similar for both blade designs; however, the reference angle value (β_3 without jet) is different for the two designs. The difference in measured angle with no jet flow is probably the combined result of many effects. First, the experimental results indicate that although flow separation was much more pronounced on the low solidity jet flap, separation was experienced with zero jet flow on both blade designs. Because the amount of gas turning varies inversely with the degree of flow separation, the modified jet flap experienced less underturning (relative to the design value) when the jet was turned off. Another reason why the reference zero jet flow angles were different for the two jet flap designs was that the flow and efficiency assumptions for the two turbines were different. Design values of efficiency and flow rate were 84% and 45.51 lb/sec (20.64 kg/sec) for the modified jet flap blade and 86.7% and 47.7 lb/sec (21.6 kg/sec) for the low solidity jet flap turbine. These differences, combined with slightly different design procedures, produced different throat areas for the two turbines. The low solidity jet flap turbine had about 3% more throat area than did the modified jet flap turbine.

Figure 39 correlates the relative angle data of Figure 38 with jet momentum coefficient, C_j , for the two jet flap designs. The jet momentum coefficient was considered to be an average momentum coefficient defined as

$$C_j = \frac{\dot{m}_j \bar{U}_j}{(\dot{m}_p + \dot{m}_j) \bar{W}_3} .$$

C_j was computed based on measured jet and primary flow rates, computed downstream total average relative velocity, and computed jet velocity which expanded from the mean section cavity pressure to the measured downstream average static pressure. The jet deflection angle, θ , is defined as the relative angle measured with jet off minus the relative angle measured with jet on. Data for these two blade designs correlate well when presented in

this manner. A variation in deflection angle of about 10 degrees was observed over the range of jet momentum coefficients investigated. The design $C_j - \theta$ curve for $\tau = 90$ degrees is included in Figure 39. For a given value of C_j , the experimental curve demonstrated more deflection (i. e., larger θ) than the design curve. The reasons for this is primarily because the design curve was generated from the experimental results of Reference 2 and in that reference $\beta_3 w_{o/j}$ was not measured and had to be computed. It was assumed to be parallel to the very aft trailing edge pressure surface contour. This was apparently an optimistic assumption. If measurements had been made with no jet flow in Reference 2, flow separation probably would have been observed which would have resulted in larger than assumed values of $\beta_3 w_{o/j}$ (Reference 2).

Figures 40 through 43 present the static pressure distribution through the turbine for various turbine expansion ratios and cavity pressure ratios. In general, the low solidity turbine operated with negative reaction in the hub region over most of the expansion ratios and cavity pressures investigated. Increasing the cavity pressure ratio, P_{T_I}/P_{T_0} , increased the jet momentum which subsequently reduced the throat dimension of the blading passage; thus, the rotor blade row became more reactive as the jet flow was increased. This is illustrated in Figure 40 which shows that with no jet flow the reaction is negative for all expansion ratios investigated (i. e., $1.6 < Re_{TT} < 2.5$), while, in Figure 43 (where $P_{T_I}/P_{T_0} = 1.2$) the blade hub changed from negative reaction to impulse at $Re_{TT} = 2.13$. Figure 42 shows that the design level of negative reaction at the hub section was nearly satisfied by the low solidity jet flap design. Measured and design values of P_{st}/P_{T_0} through the turbine are as follows:

Comparison of measured and design values
of static pressure through turbine

<u>Station</u>	<u>Design, P_{st}/P_{T_0}</u>	<u>Measured, P_{st}/P_{T_0}</u>
0 - hub and tip	0.964	0.965
1 - hub	0.375	0.394
1 - tip	0.600	0.579
2 - hub	0.420	0.420
2 - tip	0.420	0.420

The static pressure distributions of Figures 40 through 43 show that for all expansion ratios the rotor did not choke for all values of P_{T_I}/P_{T_0} investigated. That is, as the turbine exit hub and tip static pressure was reduced, both the stator exit hub and tip pressures also were reduced. The rotor was not choked and, therefore, did not prevent the flow conditions downstream of the rotor from being felt upstream of the rotor at the stator exit.

The modified jet flap blade had similar reaction-impulse characteristics as those previously mentioned for the low solidity blade. A comparison of the static pressure distribution characteristics for the two jet flap designs is shown in Figure 44. These data represent the static pressure distributions through the two turbines as a function of percent jet flow at design speed and expansion ratio and show that the low solidity jet flap turbine is a lower reaction turbine than the modified jet flap rotor turbine. The modified design changes to impulse at 3.8% jet flow, while a reasonable extrapolation of the low solidity jet flap data would suggest that 5% jet flow would be required to create an impulse-type flow condition at the hub section of the low solidity jet flap blade. This condition is the result of the throat area of the low solidity blade being about 3% larger than the throat area of the modified blade design. For the same expansion ratio across the two turbines the low solidity jet flap blade had more reaction across the stator and less reaction across the rotor (i. e., higher rotor exit pressure) than did the modified jet flap turbine.

The effect of rotor cavity pressure ratio on turbine efficiency is presented in Figures 45 and 46 as a function of turbine expansion ratio. Figure 45 shows the effect on thermodynamic efficiency. Figure 46 shows the effect on base efficiency.

The results in Figure 45 show that the performance fell off fairly rapidly for all cavity pressure ratios investigated as the turbine expansion ratio was increased. The predicted suction surface critical velocity ratio with the jet on exceeded 1.2 in the aft region of the tip section. The rapid deterioration in performance with increasing expansion ratio suggests normal shocks may have been created in the high velocity flow field and were promoting separation from the blading surfaces.

Figure 45 shows that at design expansion ratio, a cavity pressure ratio of 0.6 produced the maximum efficiency. Also at this expansion ratio, the turbine efficiency was only 80.75% with no jet flow. This low efficiency was caused by strong flow separation from the blading suction surfaces with the resulting small gas turning in the rotor and loss in total pressure. As the jet was activated, the diffusion on the suction surface was reduced, flow separation was delayed to further aft on the airfoil, and the flow field began to approach that required by the design velocity diagrams. However, as the cavity pressure was further increased ($P_{T1}/P_{T0} \sim 1.0$), the jet flow approached a choking condition and the rate of change of jet momentum with respect to cavity pressure began to decrease. Thus, the increase in effectiveness of the jet flap in deflecting the primary stream began to wane with increasing cavity pressure. This condition of decreasing jet effectiveness, coupled with increasing ideal jet flow power term ($\dot{m}_j \Delta H_{j1-3}$) in the efficiency definition actually produced a decrease in turbine thermodynamic efficiency with increasing jet cavity pressure ratio. At design speed and expansion

ratio, the maximum thermodynamic efficiency was 82.4% and occurred with a cavity pressure ratio of $P_{T_I}/P_{T_0} = 0.6$. Although not shown on Figure 45, at design work and speed this efficiency dropped to 81.2%.

The variation of base total-to-total efficiency with expansion ratio was similar to that described for the thermodynamic efficiency. Figure 46 shows that, at all expansion ratios, the rate of change of base efficiency decreased with increasing cavity pressure ratio. This (as discussed earlier) is a consequence of the choking characteristics of the jet slot. However, since this definition of efficiency does not include a term which accounts for the jet flow ideal power, the base efficiency continues to increase with increasing cavity pressure ratio. At design speed and expansion ratio, the maximum efficiency measured occurred with $P_{T_I}/P_{T_0} = 1.2$ and was 85.5%.

The influence of jet flow rate on turbine performance at design speed and expansion ratio for the two jet flap designs is presented in Figure 47. The large difference in maximum percentage of jet flow rate (over 8% for the modified jet flap and only 3.4% for the low solidity design) was caused by the difference in jet slot sizes for the two designs. The jet slot sizes were 0.025 in. (0.064 cm) and 0.038 in. (0.097 cm) for the low solidity and modified jet flap blades, respectively. The difference in efficiency level of 85.2% for the modified jet flap and 80.75% for the low solidity design with zero jet flow was caused primarily by the solidity and loading level requirements for these two jet flap designs. The low solidity blade mean section design compressible tangential lift coefficient value was 1.43 and it had about 62% less solidity than the modified jet flap blade design. The mean section lift coefficient was about 0.85 for the modified design. Flow separation was probably experienced on both of these blading designs with zero jet flow, but to a much greater degree on the low solidity design—thus the lower measured efficiency with no jet flow.

The base efficiency curves had very similar shapes as a function of percent jet flow for the two blade designs. However, they were displaced by the constant difference in efficiency that was developed with zero jet flow. As noted earlier, the base definition of efficiency continues to increase in magnitude with increasing jet flow. The thermodynamic definition, however, reached a peak value of 88.2% at about 3.5% jet flow for the modified blade while the low solidity blade reached its peak value of 82.4% at about 1.5% jet flow. The same efficiency information is plotted against P_{T_I}/P_{T_0} for the two blade designs in Figure 48; these peak values of thermodynamic efficiency occurred with cavity pressure ratio conditions of about 0.6 for both jet flap blade designs.

Turbine Overall Performance

The optimization results that have just been presented show that maximum performance occurred when the rotor cavity pressure ratio, P_{T_I}/P_{T_0} , had a value of about 0.6. In particular, Figure 45 showed that above the design expansion, $Re_{TT} = 2.01$, $P_{T_I}/P_{T_0} \sim 0.6$ produced the best performance while below $Re_{TT} = 2.01$, $P_{T_I}/P_{T_0} = 1.0$, produced the highest turbine efficiency. In view of these results and the fact that (1) at $Re_{TT} = 2.01$ the efficiency with $P_{T_I}/P_{T_0} = 1.0$ was only slightly less than that with $P_{T_I}/P_{T_0} = 0.6$ and (2) $P_{T_I}/P_{T_0} = 1.0$ represents a very reasonable value of cavity pressure ratio from an engine application standpoint, it was decided to conduct the overall turbine performance phase of the test program with $P_{T_I}/P_{T_0} = 1.0$. Also, the rotor cavity temperature ratio, T_{T_I}/T_{T_0} , was again set equal to unity.

Still considering Figure 45 (where the turbine performance was shown to be good at the lower expansion ratios), the decision was made to (1) extend the overall turbine performance testing phase to include the low speed and expansion ratio operating regime, and (2) eliminate much of the testing in the high expansion ratio portion of the map. Rotor exit surveys of total pressure, total temperature, and gas angle were performed at $Re_{TT} = 2.01$, $N/\sqrt{\theta}_{cr} = 100\%$, and $Re_{TT} = 1.3$, $N/\sqrt{\theta}_{cr} = 65\%$. Surveys of static pressure on the blading mean section surfaces were conducted at the same two operating points.

The overall performance of the low solidity jet flap rotor turbine is shown in Figure 49. This map presents the equivalent shaft work ($\Delta H/\theta_{cr}$) as a function of the equivalent flow speed parameter ($\dot{m}_p N \epsilon/60 \delta_0$) for lines of constant total-to-total expansion ratio (P_{T_0}/P_{T_3}) and equivalent rotor speed ($N/\sqrt{\theta}_{cr}$). Contours of constant total thermodynamic efficiency ($\eta_{T_{thermo}}$) are also included. At design speed and expansion ratio the total thermodynamic efficiency was 83.4%. This value of efficiency is higher than that measured at comparable conditions during the cavity pressure optimization study. The reason for the difference is a slight difference in flow rate measured in the optimization study and in the overall performance study. This efficiency compares with a value of 85.4% for the modified jet flap blade when operated with a cavity pressure ratio, P_{T_I}/P_{T_0} , of unity. However, because of the larger slot size the modified blade was passing more than 6% jet flow while the low solidity design was passing 2.7% when P_{T_I}/P_{T_0} was unity. Figure 47 shows that when the modified jet flap blade was passing a comparable 2.7% jet flow, its thermodynamic efficiency was 88%. These data illustrate that the amount of secondary flow used to perform a function in a turbine—whether it be jet flow as in the present investigation or cooling flow in higher temperature applications—has a very

significant effect on the value of thermodynamic efficiency. The thermodynamic efficiency was reduced to 82.7% at design speed and work for the low solidity design; this compares with a value of 85.2 for the modified jet flap operating under similar conditions. The efficiency increased with decreasing expansion ratio. A maximum thermodynamic efficiency of 87.8% occurred at 90% design corrected speed and an expansion ratio of 1.3.

The variation of primary equivalent flow with overall expansion ratio and equivalent speed is presented in Figure 50. The turbine choked at a total expansion ratio of about 2.2. At the design expansion ratio of 2.01 and design speed, the turbine measured equivalent flow was 47.2 lb/sec (21.41 kg/sec) compared to a design value of 47.7 lb/sec (21.6 kg/sec). This is a slight decrease from the 47.4 lb/sec (21.5 kg/sec) that was measured during the rotor cavity pressure optimization study. The effect of increasing speed produced a slight decrease in the corrected flow through the turbine.

Figures 51 and 52 demonstrate how the secondary flow varied with expansion and speed. The jet flow rate, corrected on rotor cavity conditions, is presented in Figure 51 as a function of speed and expansion ratio. It is presented in Figure 52 as a ratio of corrected primary flow. Figure 52 shows that the pumping action of the rotor produced an increase in equivalent jet flow from about 2.2 to about 2.8% as the speed increased from 55 to 110% of design value. Figures 51 and 52 show the slot passed slightly more than design flow. The design value was 2.3% whereas the measured value was nearly 2.7% at design speed and expansion ratio.

Figures 53 and 54 illustrate respectively the variation of corrected torque and corrected work as functions of turbine total expansion ratio and corrected speed. At design speed and expansion ratio, the results of Figure 53 show that the measured value of equivalent torque was 1440 ft-lb (1952.4 N-m) compared with the design value of 1520 ft-lb (2060 N-m). These data also show that because the slope of torque-expansion ratio curves is positive, limiting loading was not imminent at any of the speeds investigated. The equivalent work results of Figure 54 show that at design expansion ratio and speed the equivalent work output of the turbine was 19.15 Btu/lb (44.527×10^3 joule/kg) compared with a design value of 20 Btu/lb (46.5×10^3 joule/kg).

Figure 55 presents the total-to-total thermodynamic efficiency as a function of blade-jet speed ratio ($u = U_m/V'$). V' is the exit ideal spouting velocity based on inlet total pressure and temperature and exit static pressure. At the design value of 0.446 the thermodynamic efficiency was 83.4%. The design value of efficiency was 86.7%. The peak value of efficiency was 87.8% occurring at a blade-jet speed ratio of about 0.63.

Blade Surface Static Pressure and Rotor Exit Surveys

Blade mean section surface static pressure and rotor exit surveys were conducted at two operating points. The two points were (1) design $Re_{TT} = 2.01$, $N/\sqrt{\theta}_{cr} = 100\%$ and (2) $Re_{TT} = 1.32$, $N/\sqrt{\theta}_{cr} = 65\%$. These two points have the same design value of blade-jet speed ratio. These surveyed operating points are located on the overall performance map (Figure 49). The cavity pressure ratio, P_{T1}/P_{T0} , was unity for the two operating conditions.

Blade Surface Static Pressure

Figure 56 presents the blade mean section surface static pressure nondimensionalized on turbine inlet total pressure. Figure 56a illustrates a design point comparison of surface static pressures between the low solidity and modified jet flap blade designs. The most interesting observation to be made from these results is that the jet stream on the modified blade design (1) eliminated diffusion on the suction surface and promoted a slight acceleration and (2) caused a deceleration on the pressure surface in the aft portion of the blade. This was not the case for the low solidity blade. The flow accelerated on the pressure surface and decelerated on the suction surface in the aft portion of the low solidity blade. This deceleration on the suction surface probably promoted flow separation from the blading surface. The loading level on the low solidity jet flap design appears to have been too large for the jet flap concept to function properly. Figure 56b illustrates the low solidity jet flap surface static pressures at the lower speed and pressure ratio. As previously noted, at the design point the flow accelerated on the pressure surface and decelerated on the suction surface in the aft portion of the blade. At the low speed, low expansion ratio operating point, the jet had low momentum relative to the primary stream and promoted a rather strong acceleration on the suction surface in the very aft region of the blade. However, an acceleration was also created on a large portion of the pressure surface; this resulted in a region of negative lift on the blading surface.

Rotor Exit Survey

Circumferential traverses with a combination total pressure, temperature, and yaw angle probe were made to map the flow characteristics at the rotor trailing edge. These surveys yield the circumferential variation of temperature ratio, $(T_{T0}-T_{T2})/T_{T0}$, total pressure ratio, P_{T0}/P_{T2} , blade exit absolute flow angle, and local efficiency. From these surveys contour maps of temperature ratio, pressure ratio, and local efficiency were constructed and are presented in Figures 57 through 62 for the two surveyed operating points.

The total temperature ratio contour maps presented in Figures 57 and 58 for the two points show the changes in work extraction from the fluid over the annulus surveyed. Most of the energy was extracted from the fluid in the lower half of the annulus for both operating points. Very little energy was extracted in the radially outward half of the blade.

Figures 59 and 60 show that the stage total pressure ratio, P_{T0}/P_{T2} , was not particularly uniform over the annulus for either of the two surveyed operating points. The presence of the stator wakes (coming through the large spacing between rotor blades) developed a more or less radial stratification of peaks and valleys in the total pressure distribution at the turbine exit.

The contour maps of turbine efficiency, based on locally measured total-to-total expansion ratio and temperature ratio, are presented in Figures 61 and 62. The two operating point efficiency contour plots are similar in that both show poor performance in the radially outward half of the blade span. Operating point efficiency progressively fell from about 80% at the midspan to around 65% in the tip region. The efficiency was fairly uniform from the midspan to the hub region.

Graphic integration of the traces of efficiency at constant radii yielded a plot of the circumferentially averaged efficiency at station 2 as a function of radius. The radial variation of this averaged efficiency for both of the low solidity blade operating points is illustrated in Figure 63. Also included are similar data for the modified jet flap turbine operating at design speed and expansion ratio and with a cavity pressure ratio, P_{T1}/P_{T0} , equal to unity. These results suggest that for the low solidity jet flap blade the efficiency at the design point was slightly higher than the efficiency at the $N/\sqrt{\theta}_{cr} = 65\%$, $Re_{TT} = 1.32$ operating point. This observation is borne out by examining the overall turbine performance shown in the map (Figure 49) at the conditions where the surveys were performed. Figure 49 indicates that the thermodynamic efficiency at $Re_{TT} = 2.01$, $N/\sqrt{\theta}_{cr} = 100\%$ was slightly higher than the efficiency at the $Re_{TT} = 1.32$, $N/\sqrt{\theta}_{cr} = 65\%$ point.

Comparison of the data for the low solidity and modified jet flap turbines at design speed and expansion ratios (Figure 63) reveals very large differences in radial distribution of efficiency for the two turbines. The modified jet flap design developed the highest efficiency in the tip region while the low solidity blade showed its best performance in the radially inward half of the blade span. The improved performance of the low solidity design over the modified jet flap design in the hub region is caused, at least in part, by the previously described internal guide vanes (Figure 20) which were incorporated in the low solidity jet flap blade design. The design tangential lift coefficient values were very high ($\psi_t \sim 1.4$) at all radial stations for the low solidity

jet flap. Also, the high loading was coupled with the highest free-stream Mach number flows in the outer half of the blade. The diffusion on the aft suction surface of the blading probably was too great (as suggested by the static pressure data given in Figure 56) for the jet flap effect to overcome and, therefore, the flow separated from the blading suction surface.

SUMMARY OF RESULTS

The performance of a single-stage turbine with a low solidity jet flap blade has been tested over a range of equivalent speeds and expansion ratios. The mean section axial chord solidity was 0.922. One jet slot size of 0.025 in. (0.064 cm) was investigated. A rotor cavity pressure optimization test was conducted to determine the effects of jet flow on turbine performance. Based on these tests, a rotor cavity pressure ratio of unity was selected and the overall turbine performance map was determined. The results of these tests are compared with the higher solidity modified jet flap blade. The modified blade mean section axial chord solidity was 1.541. A 0.038 in. (0.097 cm) jet slot was used in the modified jet flap tests. The low solidity and modified jet flap blades were designed to satisfy similar sets of negative hub reaction velocity diagrams. Both jet flap blades were tested with the same stator. The following observations were made.

- The variation in choked level of primary flow from zero jet flow to a cavity pressure ratio $P_{T_I}/P_{T_0} = 1.2$, was slightly under 1%.
- The jet slot choked at $P_{T_I}/P_{T_0} = 1.1$ and passed 2.7% flow as compared with the design value of 2.3%.
- The maximum efficiency at design speed and expansion ratio was obtained with $P_{T_I}/P_{T_0} = 0.6$. This efficiency was only slightly higher than the efficiency obtained with $P_{T_I}/P_{T_0} = 1.0$.
- The jet deflection angle ($\beta_3 \text{ wo/j} - \beta_3 \text{ w/j}$) ranged up to nearly 10 degrees for the jet flows investigated.
- At design speed and expansion ratio a condition of negative reaction existed for all cavity pressures investigated. Increasing P_{T_I}/P_{T_0} resulted in the rotor becoming less negative.
- The low solidity jet flap demonstrated lower hub reaction characteristics than did the modified jet flap blade. At design speed and expansion ratio the modified design became impulse with a 3.8% jet flow. Approximately 5% jet flow would have been required to make the low solidity jet flap blade hub section impulse.
- At design speed and expansion ratio and $P_{T_I}/P_{T_0} = 1.0$, the measured equivalent primary flow rate was 47.2 lb/sec (21.41 kg/sec). This compares with the design value of 47.7 lb/sec (21.6 kg/sec).
- At design speed and expansion ratio and unity cavity pressure ratio the larger jet slot size of the modified jet flap blade design passed 6.6% jet flow while the low solidity design passed 2.7%.

- At design speed and expansion ratio and $P_{T_I}/P_{T_0} = 1.0$, the thermodynamic efficiency of the low solidity jet flap turbine was 83.4%. This compares with the value of 85.4% for the modified jet flap blade operating with the same cavity pressure ratio. The design value of thermodynamic efficiency for the low solidity blade was 86.7%.
- The maximum thermodynamic efficiency of 87.8% for the low solidity blade occurred at 90% $N/\sqrt{\theta}$ cr, $Re_{TT} = 1.3$ and $P_{T_I}/P_{T_0} = 1.0$.
- Blade surface static pressure measurements indicate that at design speed and expansion ratio even with the jet activated, the flow decelerated on the aft suction surface.
- Rotor exit surveys showed that the low solidity blade had very high losses in the outer half of the blade. In the hub region the efficiency was higher than that of the modified jet flap blade design. This improved low solidity blade hub performance is attributed to the blade internal guide vanes which produced a satisfactory jet flow distribution in the hub region.
- The high blade loading requirements ($\psi_t \sim 1.4$) coupled with the high freestream Mach number flows in the outer portion of the blade probably were too severe for the jet flap of the low solidity blade to function effectively. Flow separation occurred on the aft portion of the airfoil with subsequent loss in turbine performance.

REFERENCES

1. Lueders, H. G., Experimental Investigation of Advanced Concepts to Increase Turbine Blade Loading, Vol I. Analysis and Design. NASA CR-735. June 1967.
2. Lueders, H. G., Experimental Investigation of Advanced Concepts to Increase Turbine Blade Loading, Vol II. Performance Evaluation of Jet Flap Rotor Blade. NASA CR-1580. May 1970.
3. Lueders, H. G., Experimental Investigation of Advanced Concepts to Increase Turbine Blade Loading, Vol III. Performance Evaluation of Modified Jet-Flap Rotor Blade. NASA CR-1759. 1971.
4. Bettner, J. L. and S. M. Nosek, "Summary of Tests on Two Highly Loaded Turbine Blade Concepts in Three Dimensional Cascade Sector". ASME Paper 69-WA/GT-5.
5. Bettner, J. L., Design and Experimental Results of a Highly Loaded, Low Solidity Tandem Rotor. NASA CR-1803. April 1971.
6. Lueders, H. G., Experimental Investigation of Advanced Concepts to Increase Turbine Blade Loading, Vol II, Performance Evaluation of Plain Rotor Blade. NASA CR-1172. August 1968.
7. Spence, D. A., The Two-Dimensional Jet Flap - An Exact Solution in Closed Form for Small C_j , and an Interpolation Formula Up to $C_j = 10$. Royal Aircraft Establishment, Gt Brit Report No. Aero 2568. 1956.
8. Zweifel, O., "The Spacing of Turbo-Machine Blading, Especially With Large Angular Deflection". Brown Bovevi Review. Vol. 32. December 1945. pp 436-444.
9. Bettner, J. L., Experimental Investigation in an Annular Cascade Sector of Highly Loaded Turbine Stator Blading, Vol IV. Performance of Jet Flapped Blade. NASA CR-1423. September 1969.
10. Katsanis, T., Computer Program for Calculating Velocities and Streamlines on a Blade-to-Blade Stream Surface of a Turbomachine. NASA TN-D-4525. April 1968.
11. Truckenbrodt, E., A Method of Quadrature for Calculation of Laminar and Turbulent Boundary Layer in Case of Plane and Rotationally Symmetric Flow. NACA TM-1379. 1955.

12. McNally, W. D., FORTTRAN Program for Calculating Compressible Laminar and Turbulent Boundary Layers in Arbitrary Pressure Gradients. NASA TN-D-5681. May 1970.
13. Chamey, A. J., Exploratory Research Program for Turbo Propulsion Systems. AFAPL TR-68-103, Vol 2. September 1968.

APPENDIX

JET BLADE THROAT SIZING CALCULATION PROCEDURE

The velocity diagrams developed for the low solidity jet flap rotor utilized stator performance and rotor loss information that was developed in Reference 4.

I. Downstream (Station 3) Continuity

Primary flow conditions are specified. The jet flap rate and slot size are selected, thus the station 3 total flow rate is known. W_{u3} is known from the work requirement and an initial guess was made on mean section W_3 .

Mean Section:

$$\psi_3 = \tan^{-1} [W_{u3} / (W_3^2 - W_{u3}^2)^{1/2}]$$

$$\beta_3 = 90 - \psi_3$$

$$W_{x3} = W_3 \cos \psi_3$$

$$W_{cr3} = \sqrt{\frac{2 \gamma g_c R T_{Trel3}}{\gamma + 1}}$$

$$(\rho_{st} / \rho_T)_3 = f(W_3 / W_{cr3})$$

The flow rate per unit span was calculated at the mean section.

$$(\dot{m}_T / l)_3 = (\rho_{st} / \rho_T)_3 \left(P_{Trel3} / R T_{Trel3} \right) W_{x3} s$$

The relationship between hub and mean and mean and tip axial velocities was maintained the same as those of the Reference 5 tandem rotor velocity triangles. The constants C_h and C_t were determined from those relationships:

$$W_{x3})_h = W_{x3})_m \cdot C_h$$

$$W_{x3})_t = W_{x3})_m \cdot C_t$$

Hub and Tip:

$$W_3 = (W_x^2 + W_{u3}^2)^{1/2}$$

$$(\rho_{st}/\rho_T)_3 = f(W_3/W_{cr3})$$

$$(\dot{m}_T/l)_3 = (\rho_{st}/\rho_T)_3 (P_{Trel3}/RT_{Trel3}) W_{x3} s$$

The flow rate per unit depth was integrated radially by a trapezoidal approximation to obtain a calculated total downstream flow. This was compared with the desired total flow rate and if they were not equal the mean section W_3 was adjusted and the calculation repeated starting at the mean section.

II. Jet Flow Continuity

The jet flow rate was assumed. The blade cavity total temperature at a given radius from the turbine centerline was calculated knowing the rotor shaft cavity total temperature and also the wheel speed at each radius of interest. The hub, mean, and tip section cavity temperature was computed by

$$T_{TCh, m, t} = T_{TI} + \left(\frac{U_{h, m, t}^2 - U_I^2}{2C_p} \right)$$

The cavity total pressure was determined from the computed temperature using an efficiency of compression η_{comp} . Hub, mean, and tip section cavity pressures were computed by

$$P_{TCh, m, t} = P_{TI} + \left[1 + \eta_{comp} (T_{TCh, m, t} / T_{TI} - 1) \right]^{\frac{\gamma}{\gamma-1}}$$

A compression efficiency of 100% was used in the computation.

The flow through the slot was assumed to expand from the blade cavity total conditions to turbine downstream static conditions at the blade cavity hub, mean, and tip section.

$$U_{crj} = \sqrt{\frac{2\gamma g_c R T_{TC}}{\gamma + 1}}$$

$$(P_{st}/P_T)_j = P_{st3} / P_{TC}$$

$$U/U_{crj} = f [(P_{st} / P_T)_j]$$

$$U_j = C_v (U / U_{crj}) U_{crj}$$

where C_v was a jet velocity coefficient and was set equal to 0.97 (Figure 435, p 417, Reference 13).

The equivalent flow rate per unit length of the slot was obtained using the slot flow coefficient data of Reference 2. (See Figure 4 of this report.) The actual flow was then computed.

$$\dot{m}_j / \ell = (\dot{m}_j / \ell)_{equiv} \left(\frac{P_{TC}}{14.7} \right) \times \left(\frac{518.7}{T_{TC}} \right)^{1/2}$$

The flow rate was integrated radially using a trapezoidal approximation to give a total slot flow rate. This was compared with the desired jet flow rate and, if different, P_{TP} was adjusted and the flow recomputed.

III. Satisfaction of Turning and Continuity

An initial estimate was made of the turning distribution between the blade and the jet stream. This can be expressed as the ratio of gas turning done by the blade to the total turning done.

$$\Delta = \frac{\text{blade } \Delta V_u}{\text{total } \Delta V_u}$$

at the hub, mean, and tip sections

$$(AA) \quad W_{u2} = (W_{u1} + W_{u3}) \Delta - W_{u1}$$

An initial guess was made on W_2 , without jet, at the hub, mean, and tip sections. Then,

$$(BB) \quad W_{x2} = (W_2^2 - W_{u2}^2)^{1/2}$$

$$\psi_2 = \tan^{-1} (W_{u2} / W_{x2})$$

$$\beta_2 = 90 - \psi_2$$

$$W_{cr2} = \sqrt{\frac{2 \gamma g R T_{rel3}}{\gamma + 1}}$$

$$(\rho_{st} / \rho_T)_2 = f(W_2 / W_{cr2})$$

$$(\dot{m}_p / \dot{L})_2 = (\rho_{st} / \rho_T)_2 \left(\frac{P_{Trel2}}{P_{Trel3}} \right) W_{x2} \quad s$$

$$C_j = [(\dot{m}_j / \dot{L}) U_j] / \{ [(\dot{m}_j / \dot{L}) + (\dot{m}_p / \dot{L})_2] W_3 \}$$

The jet momentum coefficient, C_j , is the ratio of jet momentum to downstream momentum at a given radius. The jet deflection angle, θ , is defined as

$$\theta_A = \beta_{3wo/j} - \beta_{3w/j}$$

Also, for the computed value of C_j and jet efflux angle, τ , the deflection angle, θ_B , can be obtained from the empirical data presented in Figure 5. If $\theta_A \neq \theta_B$, W_2 was adjusted and the calculation repeated starting at (BB).

When the turning requirements were satisfied at the hub, mean, and tip sections, the flow was integrated radially to give the station 2 flow rate. This was compared to the primary flow desired and if these were not equal, the turning distribution between the blade and the jet was adjusted and the calculation repeated starting at (AA).

IV. Throat Conditions

The throat size and angle were developed from the computed station 2 flow conditions. The two conditions to be satisfied were continuity and conservation of angular momentum. For the case of constant diameter flowpath, conservation of angular momentum reduces to

$$W_{u_{th}} = W_{u_2}$$

At the hub, mean, and tip section the following initial conditions were assumed

$$W_{u_{th}} = W_{u_2}$$

$$\beta_{th} = \beta_2$$

$$W_{x_{th}} = W_{x_2}$$

$$(\rho_{st} W_x)_2 = (\rho_{st}/\rho_T)_2 \left(\frac{P_{T_{rel2}}}{RT_{T_{rel3}}} \right) \cdot W_{x_2}$$

$$(CC) \quad \beta_{th} = \tan^{-1} (W_{x_{th}}/W_{u_{th}})$$

$$BLK = s/(s-d_t/\sin \beta_{th})$$

$$(\rho_{st} W_x)_A = (\rho_{st} W_x)_2 BLK$$

$$W_{th} = (W_{x_{th}}^2 + W_{u_{th}}^2)^{1/2}$$

$$W_{cr_{th}} = \left[2\gamma g_c R T_{T_{rel3}} / (\gamma + 1) \right]^{1/2}$$

$$(\rho_{st}/\rho_T)_{th} = f (W_{th}/W_{cr_{th}})$$

$$(\rho_{st} W_x)_B = (\rho_{st}/\rho_T)_{th} \left(\frac{P_{T_{rel\ th}}}{R T_{rel_3}} \right) W_{x\ th}$$

If $(\rho_{st} W_x)_A \neq (\rho_{st} W_x)_B$ then $W_{x_{th}}$ was adjusted and the calculation repeated starting at (CC).

When continuity was satisfied the throat dimension was computed from

$$t = (s \times \sin \beta_{th}) - d_t$$

TABLE I.

Low solidity jet flap rotor design data.

<u>Parameter</u>	<u>Units</u>	<u>Hub</u>	<u>Mean</u>	<u>Tip</u>
Radial location, r	in. (cm)	10.50 (26.67)	12.75 (32.39)	15.00 (38.10)
Axial chord, C_x	in. (cm)	2.300 (5.842)	1.945 (4.940)	1.590 (4.039)
Blade spacing, s	in. (cm)	1.736 (4.409)	2.108 (5.354)	2.480 (6.299)
Axial chord solidity, $\sigma_x = C_x/s$		1.324	0.922	0.641
Throat dimension, t	in. (cm)	1.293 (3.284)	1.434 (3.642)	1.597 (4.056)
Leading edge diameter, d_l	in. (cm)	0.044 (0.112)	0.084 (0.213)	0.124 (0.315)
Trailing edge diameter, d_t	in. (cm)	0.120 (0.305)	0.120 (0.305)	0.120 (0.305)
Blade setting angle, ϕ (See Figure 5.)	degrees	-7.067	+8.781	+30.004
Blade cavity total pressure, P_{T1}/δ_0	psia (N/cm ²)	16.258 (11.209)	17.039 (11.748)	18.007 (12.415)
Blade cavity total temperature, T_{T1}/θ_{cr}	°R (°K)	533.89 (296.61)	541.10 (300.61)	549.71 (305.39)
Jet flow ratio, \dot{m}_j/\dot{m}_p		0.0316	0.0219	0.0199
Jet velocity, u_j	ft/sec (m/sec)	1204.9 (367.3)	1248.1 (380.4)	1286.9 (392.2)
Slot size, \overline{hb}	in. (cm)	0.025 (0.064)	0.025 (0.064)	0.025 (0.064)
Jet momentum coefficient, C_j		0.0671	0.0362	0.0297
Jet deflection angle, θ	degrees	5.361	3.520	3.100
Jet efflux angle, τ	degrees	90.0	90.0	90.0
Inlet critical velocity ratio, W/W_{cr1}		0.785	0.622	0.427
Exit critical velocity ratio, $W/W_{cr3 w/j}$		0.600	0.775	0.833
Compressible tangential lift coefficient, ψ_t		1.482	1.434	1.340
Blade row reaction, R		-0.706	+0.358	+0.737

Table II.

Jet flap blade section coordinates.External profile—hub section

<u>x</u>		<u>y</u>		<u>x</u>		<u>y</u>	
<u>in.</u>	<u>(cm)</u>	<u>in.</u>	<u>(cm)</u>	<u>in.</u>	<u>(cm)</u>	<u>in.</u>	<u>(cm)</u>
0.7249	1.8412	3.0338	7.7058	3.0174	7.6642	2.9669	7.5359
0.7270	1.8466	3.0432	7.7297	3.0140	7.6555	2.9618	7.5229
0.7553	1.9184	3.1017	7.8783	3.0090	7.6428	2.9543	7.5039
0.8125	2.0637	3.2024	8.1341	3.0049	7.6324	2.9483	7.4887
0.8666	2.2012	3.2781	8.3264	2.9899	7.5943	2.9466	7.4844
0.9450	2.4003	3.3691	8.5575	2.9426	7.4742	2.9885	7.5908
1.0210	2.5933	3.4419	8.7424	2.8717	7.2941	3.0461	7.7371
1.1201	2.8451	3.5200	8.9408	2.8306	7.1897	3.0755	7.8118
1.2172	3.0917	3.5825	9.0995	2.7892	7.0846	3.1020	7.8791
1.3129	3.3347	3.6324	9.2263	2.7476	6.9789	3.1270	7.9426
1.4071	3.5740	3.6713	9.3251	2.7058	6.8727	3.1501	8.0013
1.5001	3.8103	3.7011	9.4008	2.6424	6.7117	3.1802	8.0777
1.6151	4.1024	3.7272	9.4671	2.5786	6.5496	3.2057	8.1425
1.7286	4.3906	3.7414	9.5032	2.5141	6.3858	3.2273	8.1973
1.8410	4.6761	3.7464	9.5158	2.4277	6.1664	3.2514	8.2585
1.9523	4.9588	3.7428	9.5067	2.3408	5.9456	3.2714	8.3093
2.0626	5.2390	3.7309	9.4765	2.2314	5.6677	3.2898	8.3561
2.1718	5.5164	3.7103	9.4242	2.1212	5.3878	3.3022	8.3876
2.2800	5.7912	3.6817	9.3515	2.0104	5.1064	3.3105	8.4087
2.3871	6.0632	3.6444	9.2567	1.8990	4.8235	3.3127	8.4143
2.4931	6.3325	3.5983	9.1397	1.7866	4.5379	3.3075	8.4011
2.5978	6.5984	3.5416	8.9957	1.6733	4.2502	3.2954	8.3703
2.6806	6.8087	3.4883	8.8603	1.5593	3.9606	3.2771	8.3238
2.7621	7.0157	3.4244	8.6979	1.4444	3.6688	3.2518	8.2596
2.8222	7.1684	3.3680	8.5547	1.3518	3.4336	3.2260	8.1940
2.8811	7.3179	3.3029	8.3894	1.2588	3.1974	3.1967	8.1196
2.9389	7.4648	3.2277	8.1983	1.1654	2.9601	3.1651	8.0393
2.9765	7.5603	3.1709	8.0541	1.0953	2.7821	3.1399	7.9753
3.0131	7.6533	3.1055	7.8879	1.0251	2.6038	3.1141	7.9098
3.0363	7.7122	3.0591	7.7701	0.9547	2.4249	3.0876	7.8425
3.0415	7.7254	3.0265	7.6873	0.9079	2.3061	3.0698	7.7973
3.0350	7.7089	3.0015	7.6238	0.8609	2.1867	3.0520	7.7521
3.0270	7.6886	2.9830	7.5768	0.8140	2.0676	3.0348	7.7084
				0.7543	1.9159	3.0131	7.6533

Table II (cont).

External profile—mean section

x		y		x		y	
in.	(cm)	in.	(cm)	in.	(cm)	in.	(cm)
1.0661	2.7079	3.0258	7.6855	3.0236	7.6800	2.9601	7.5187
1.0709	2.7201	3.0448	7.7338	3.0216	7.6749	2.9540	7.5032
1.0959	2.7836	3.0910	7.8512	3.0190	7.6683	2.9454	7.4813
1.1253	2.8583	3.1423	7.9815	3.0159	7.6604	2.9360	7.4437
1.1552	2.9342	3.1906	8.1041	3.0002	7.6205	2.9309	7.4445
1.2014	3.0516	3.2549	8.2675	2.9376	7.4615	2.9773	7.5624
1.2485	3.1712	3.3118	8.4120	2.8810	7.3178	3.0167	7.6624
1.3125	3.3338	3.3810	8.5878	2.8395	7.2123	3.0437	7.7310
1.3778	3.4996	3.4416	8.7417	2.7982	7.1074	3.0691	7.7955
1.4445	3.6690	3.4931	8.8725	2.7572	7.0033	3.0931	7.8565
1.5123	3.8412	3.5379	8.9863	2.7165	6.8999	3.1147	7.9114
1.5810	4.0157	3.5764	9.0841	2.6560	6.7462	3.1433	7.9840
1.6684	4.2377	3.6155	9.1834	2.5962	6.5944	3.1682	8.0472
1.7570	4.4628	3.6456	9.2598	2.5368	6.4435	3.1903	8.1034
1.8470	4.6914	3.6678	9.3162	2.4584	6.2443	3.2142	7.9355
1.9383	4.9233	3.6809	9.3495	2.3809	6.0475	3.2323	8.2101
2.0308	5.1582	3.6866	9.3640	2.2851	5.8042	3.2484	8.2510
2.1245	5.3962	3.6835	9.3561	2.1901	5.5629	3.2588	8.2774
2.2199	5.6386	3.6709	9.3241	2.0962	5.3244	3.2629	8.2878
2.3165	5.8839	3.6491	9.2687	2.0032	5.0881	3.2606	8.2819
2.4149	6.1339	3.6167	9.1864	1.9109	4.8537	3.2543	8.2659
2.5154	6.3891	3.5703	9.0686	1.8191	4.6205	3.2438	8.2393
2.5974	6.5974	3.5230	8.9484	1.7282	4.3869	3.2283	8.1999
2.6811	6.8100	3.4644	8.7996	1.6379	4.1603	3.2081	8.1486
2.7457	6.9741	3.4093	8.6596	1.5663	3.9784	3.1881	8.0978
2.8116	7.1415	3.3447	8.4956	1.4953	3.7981	3.1643	8.0373
2.8794	7.3137	3.2686	8.3023	1.4248	3.6190	3.1375	7.9693
2.9262	7.4326	3.2074	8.1468	1.3722	3.4854	3.1157	7.9139
2.9744	7.5550	3.1374	7.9690	1.3197	3.3520	3.0924	7.8560
3.0246	7.6825	3.0562	7.7628	1.2677	3.2200	3.0670	7.7902
3.0321	7.7015	3.0349	7.7087	1.2332	3.1323	3.0490	7.7445
3.0330	7.7038	3.0050	7.6327	1.1987	3.0447	3.0306	7.6977
3.0290	7.6937	2.9800	7.5692	1.1642	2.9571	3.0120	7.6505
				1.1249	2.8573	2.9905	7.5959

Table II (cont).

External profile—tip section

<u>x</u>		<u>y</u>		<u>x</u>		<u>y</u>	
<u>in.</u>	<u>cm</u>	<u>in.</u>	<u>cm</u>	<u>in.</u>	<u>cm</u>	<u>in.</u>	<u>cm</u>
1.2095	3.0721	3.0103	7.6460	3.0355	7.7102	2.9701	7.5441
1.2106	3.0749	3.0215	7.6746	3.0365	7.7127	2.9550	7.5057
1.2247	3.1107	3.0843	7.8341	3.0378	7.7160	2.9350	7.4549
1.2362	3.1399	3.1232	7.9329	3.0389	7.7188	2.9159	7.4064
1.2500	3.1750	3.1583	8.0221	3.0232	7.6789	2.9069	7.3835
1.2736	3.2349	3.2055	8.1420	2.9379	7.4623	2.9580	7.5133
1.3005	3.3033	3.2474	8.2484	2.9010	7.3685	2.9777	7.5634
1.3402	3.4041	3.2963	8.3726	2.8525	7.2454	3.0029	7.6274
1.3837	3.5146	3.3388	8.4806	2.8052	7.1252	3.0258	7.6855
1.4305	3.6335	3.3754	8.5735	2.7594	7.0089	3.0463	7.7376
1.4801	3.7595	3.4073	8.6545	2.7147	6.8953	3.0648	7.7846
1.5324	3.8923	3.4345	8.7236	2.6503	6.7318	3.0881	7.8438
1.6017	4.0683	3.4616	8.7925	2.5881	6.5748	3.1074	7.8928
1.6753	4.2553	3.4814	8.8428	2.5282	6.4224	3.1229	7.9322
1.7527	4.4519	3.4945	8.8760	2.4508	6.2250	3.1393	7.9738
1.8330	4.6558	3.5027	8.8969	2.3757	6.0343	3.1516	8.0051
1.9162	4.8670	3.5058	8.9047	2.2853	5.8047	3.1609	8.0287
2.0023	5.0858	3.5039	8.8999	2.1984	5.5839	3.1642	8.0371
2.0910	5.3111	3.4974	8.8834	2.1146	5.3711	3.1622	8.0320
2.1828	5.5443	3.4855	8.8532	2.0333	5.1646	3.1557	8.0155
2.2789	5.7884	3.4664	8.8047	1.9540	4.9632	3.1459	7.9906
2.3799	6.0449	3.4386	8.7340	1.8765	4.7663	3.1329	7.9576
2.4651	6.2614	3.4086	8.6578	1.8009	4.5743	3.1166	7.9162
2.5557	6.4915	3.3697	8.5590	1.7267	4.3858	3.0981	7.8692
2.6269	6.6723	3.3346	8.4699	1.6683	4.2375	3.0813	7.8265
2.7026	6.8646	3.2919	8.3614	1.6106	4.0909	3.0635	7.7813
2.7841	7.0716	3.2389	8.2268	1.5534	3.9456	3.0450	7.7343
2.8437	7.2230	3.1947	8.1145	1.5104	3.8364	3.0310	7.6987
2.9067	7.3754	3.1445	7.9870	1.4676	3.7277	3.0168	7.6627
3.0084	7.6413	3.0540	7.7572	1.4251	3.6198	3.0022	7.6256
3.0193	7.6690	3.0403	7.7224	1.3966	3.5474	2.9926	7.6012
3.0280	7.6911	3.0203	7.6716	1.3681	3.4750	2.9831	7.5771
3.0330	7.7038	2.9971	7.6126	1.3397	3.4028	2.9735	7.5527
				1.2855	3.2652	2.9552	7.5062

Table II (cont).

Internal profile—hub section

x		y		x		y	
in.	cm	in.	cm	in.	cm	in.	cm
1.0595	2.6911	3.2942	8.3673	3.0000	7.6200	3.0000	7.6200
1.0617	2.6967	3.3046	8.3937	2.9917	7.5989	2.9988	7.6170
1.0931	2.7765	3.3633	8.5428	2.9583	7.5141	3.0276	7.6901
1.1387	2.8923	3.4239	8.6967	2.9064	7.3823	3.0700	7.7978
1.1822	3.0028	3.4666	8.8052	2.8541	7.2494	3.1096	7.8984
1.2244	3.1100	3.5002	8.8905	2.8014	7.1156	3.1459	7.9906
1.2866	3.2680	3.5402	8.9921	2.7482	6.9804	3.1786	8.0736
1.3477	3.4232	3.5710	9.0703	2.6946	6.8443	3.2081	8.1486
1.4280	3.6271	3.6039	9.1539	2.6409	6.7079	3.2353	8.2177
1.5076	3.8293	3.6303	9.2210	2.5685	6.5240	3.2671	8.2984
1.6059	4.0790	3.6543	9.2819	2.4955	6.3386	3.2932	8.3647
1.7030	4.3256	3.6692	9.3198	2.4220	6.1519	3.3154	8.4211
1.7992	4.5700	3.6762	9.3375	2.3294	5.9167	3.3374	8.4770
1.8946	4.8123	3.6761	9.3373	2.2362	5.6799	3.3558	8.5237
1.9892	5.0526	3.6696	9.3208	2.1425	5.4420	3.3690	8.5573
2.0829	5.2906	3.6566	9.2878	2.0484	5.2029	3.3782	8.5806
2.1758	5.5265	3.6376	9.2395	1.9536	4.9621	3.3830	8.5928
2.2681	5.7610	3.6132	9.1775	1.8582	4.7198	3.3817	8.5895
2.3598	5.9939	3.5829	9.1006	1.7620	4.4755	3.3761	8.5753
2.4506	6.2245	3.5466	9.0084	1.6655	4.2304	3.3660	8.5496
2.5407	6.4534	3.5044	8.9012	1.5877	4.0328	3.3543	8.5199
2.6122	6.6350	3.4653	8.8019	1.5095	3.8341	3.3389	8.4808
2.6829	6.8146	3.4206	8.6883	1.4311	3.6350	3.3215	8.4336
2.7528	6.9921	3.3690	8.5573	1.3527	3.4359	3.3033	8.3904
2.8216	7.1669	3.3084	8.4033	1.2939	3.2865	3.2912	8.3596
2.8890	7.3381	3.2368	8.2215	1.2354	3.1379	3.2811	8.3340
2.9382	7.4630	3.1727	8.0567	1.1966	3.0394	3.2758	8.3205
2.9701	7.5441	3.1224	7.9309	1.1580	2.9413	3.2720	8.3109
3.0008	7.6220	3.0627	7.7793	1.1196	2.8438	3.2697	8.3050
3.0082	7.6408	3.0255	7.6848	1.0842	2.7539	3.2692	8.3038

Table II (cont).

Internal profile—mean section

x		y		x		y	
in.	cm	in.	cm	in.	cm	in.	cm
1.3368	8.6245	3.2373	8.2227	3.0000	7.6200	3.0000	7.6200
1.3395	3.4023	3.2486	8.2514	2.9819	7.5740	2.9941	7.6050
1.3554	3.4427	3.2780	8.3261	2.9533	7.5014	3.0148	7.6576
1.3805	3.5065	3.3172	8.4257	2.9008	7.3680	3.0521	7.7523
1.4065	3.5725	3.3511	8.5118	2.8488	7.2360	3.0872	7.8415
1.4329	3.6396	3.3813	8.5885	2.7970	7.1044	3.1199	9.9245
1.4736	3.7396	3.4203	8.6876	2.7455	6.9736	3.1504	8.0020
1.5153	3.8489	3.4531	8.7709	2.6946	6.8443	3.1781	8.0724
1.5717	3.9921	3.4905	8.6959	2.6440	6.7158	3.2029	8.1354
1.6292	4.1382	3.5222	8.9464	2.5771	6.5458	3.2327	8.2111
1.7022	4.3236	3.5535	9.0259	2.5110	6.3779	3.2578	8.2748
1.7763	4.5118	3.5776	9.0871	2.4455	6.2116	3.2781	8.3264
1.8513	4.7023	3.5969	9.1361	2.3646	6.0061	3.2978	8.3764
1.9269	4.8943	3.6107	9.1712	2.2845	5.8026	3.3124	8.4135
2.0037	5.0894	3.6179	9.1895	2.2050	5.6007	3.3228	8.4399
2.0816	5.2873	3.6177	9.1890	2.1262	5.4005	3.3285	8.4544
2.1606	5.4879	3.6108	9.1714	2.0481	5.2022	3.3306	8.4597
2.2405	5.6909	3.5971	9.1366	1.9706	5.0053	3.3284	8.4541
2.3218	5.8974	3.5753	9.0813	1.8936	4.8097	3.3227	8.4397
2.4042	6.1067	3.5454	9.0053	1.8171	4.6154	3.3138	8.4171
2.4881	6.3198	3.5069	8.9075	1.7562	4.4607	3.3042	8.3927
2.5561	6.4925	3.4693	8.8120	1.6958	4.3073	3.2923	8.3624
2.6253	6.6683	3.4249	8.6992	1.6358	4.1549	3.2776	8.3251
2.6952	6.8458	3.3751	8.5728	1.5761	4.0033	3.2610	8.2829
2.7665	7.0269	3.3173	8.4259	1.5313	3.8895	3.2487	8.2517
2.8394	7.2121	3.2485	8.2512	1.4863	3.7752	3.2372	8.2225
2.8954	7.3543	3.1884	8.0985	1.4562	3.6987	3.2301	8.2045
2.9338	7.4519	3.1411	7.9784	1.4261	3.6223	3.2238	8.1885
2.9739	7.5537	3.0833	7.8316	1.3959	3.5456	3.2180	8.1737
3.0013	7.6233	3.0250	7.6835	1.3655	3.4684	3.2128	8.1605

Table II (cont).

Internal profile—tip section

x		y		x		y	
in.	cm	in.	cm	in.	cm	in.	cm
1.4462	3.6733	3.1915	8.1064	3.0000	7.6200	3.0000	7.6200
1.4468	3.7003	3.1969	8.1201	2.9734	7.5524	2.9835	7.5781
1.4531	3.6909	3.2226	8.1854	2.9500	7.4930	2.9966	7.6114
1.4637	3.7178	3.2517	8.2593	2.8906	7.3421	3.0285	7.6924
1.4763	3.7498	3.2770	8.3236	2.8330	7.1958	3.0573	7.7655
1.4910	3.7871	3.2990	8.3795	2.7761	7.0513	3.0849	7.8356
1.5158	3.8501	3.3270	8.4506	2.7204	6.9098	3.1103	7.9002
1.5435	3.9205	3.3500	8.5090	2.6661	6.7719	3.1334	7.9588
1.5839	4.0231	3.3747	8.5717	2.6135	6.6383	3.1534	8.0096
1.6272	4.1331	3.3945	8.6220	2.5455	6.4656	3.1766	8.0686
1.6849	4.2796	3.4128	8.6685	2.4800	6.2992	3.1953	8.1161
1.7462	4.4353	3.4250	8.6695	2.4167	6.1384	3.2104	8.1544
1.8101	4.5977	3.4327	8.7191	2.3409	5.9459	3.2232	8.1869
1.8760	4.7650	3.4367	8.7292	2.2685	5.7620	3.2304	8.2052
1.9440	4.9378	3.4378	8.7307	2.1986	5.5844	3.2330	8.2118
2.0139	5.1153	3.4346	8.7239	2.1309	5.4125	3.2322	8.2098
2.0853	5.2967	3.4292	8.7102	2.0643	5.2433	3.2290	8.2017
2.1589	5.4836	3.4201	8.6871	1.9993	5.0782	3.2233	8.1872
2.2353	5.6777	3.4060	8.6512	1.9359	4.9172	3.2149	8.1658
2.3151	5.8804	3.3862	8.6009	1.8736	4.7589	3.2044	8.1392
2.3963	6.0866	3.3641	8.5448	1.8247	4.6347	3.1945	8.1140
2.4623	6.2619	3.3442	8.4943	1.7764	4.5121	3.1833	8.0856
2.5311	6.4290	3.3197	8.4320	1.7281	4.3894	3.1723	8.0576
2.6031	6.6119	3.2898	8.3561	1.6789	4.2644	3.1630	8.0340
2.6788	6.8042	3.2533	8.2634	1.6408	4.1676	3.1579	8.0211
2.7595	7.0091	3.2081	8.1486	1.6015	4.0678	3.1551	8.0140
2.8246	7.1745	3.1673	8.0449	1.5743	3.9987	3.1547	8.0129
2.8712	7.2928	3.1331	7.9581	1.5465	3.9281	3.1555	8.0150
2.9229	7.4242	3.0910	7.8511	1.5178	3.8552	3.1580	8.0213
2.9867	7.5862	3.0309	7.6985	1.4651	3.7213	3.1671	8.0444

Table III.

Design operating point blade loads.

$$N/\sqrt{\theta}_{cr} = 4660 \text{ rpm } (487.99 \frac{\text{rad}}{\text{sec}})$$

$$P_{T_0}/P_{T_3} = 2.01 \quad \dot{m}_j/\dot{m}_p = 2.30\%$$

Lift—lb_f/in. (N/cm) Drag*—lb_f/in. (N/cm)

Hub	7.450	13.047	+0.316	+0.553
Mean	8.382	14.679	-1.733	-3.035
Tip	8.339	14.604	-5.7035	-9.988

* positive drag is in downstream direction

$$\dot{m}_j/\dot{m}_p = 2.3\%$$

$$\overline{hb} = 0.025 \text{ in. (0.064 cm)}$$

$$P_{T1}/P_{T0} = 1.0, T_{T1}/T_{T0} = 1.0$$

Hub—10.5 in. (26.67 cm) radius

Mean—12.75 in. (32.39 cm) radius

Tip—15.0 in. (38.10 cm) radius

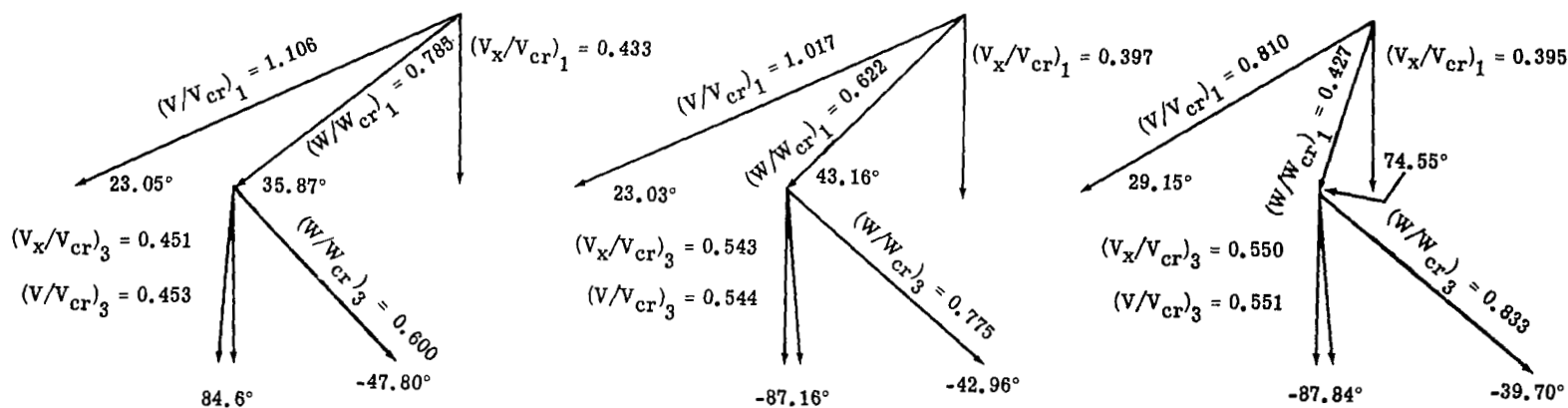


Figure 1. Jet flap blade velocity triangles with jet on.

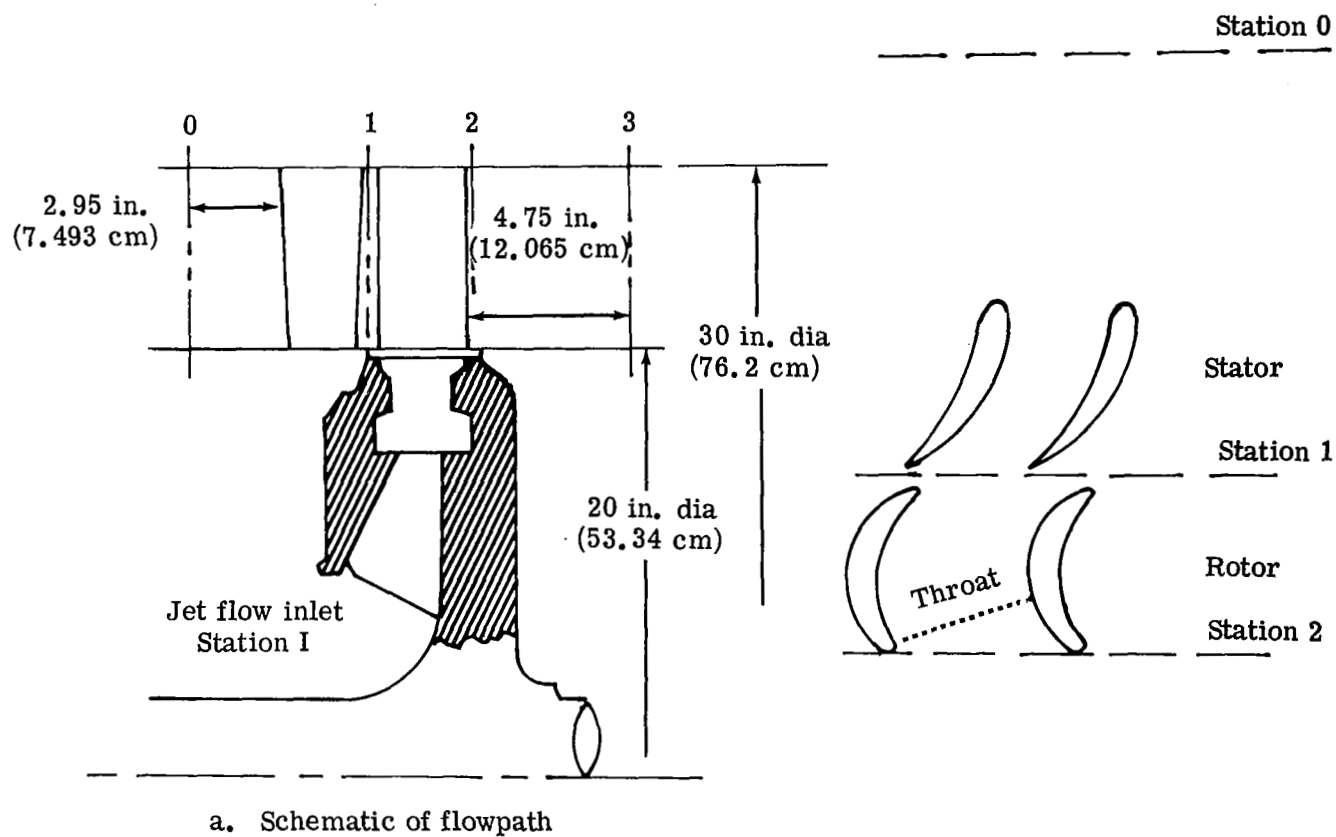


Figure 2. Jet flap turbine station nomenclature.

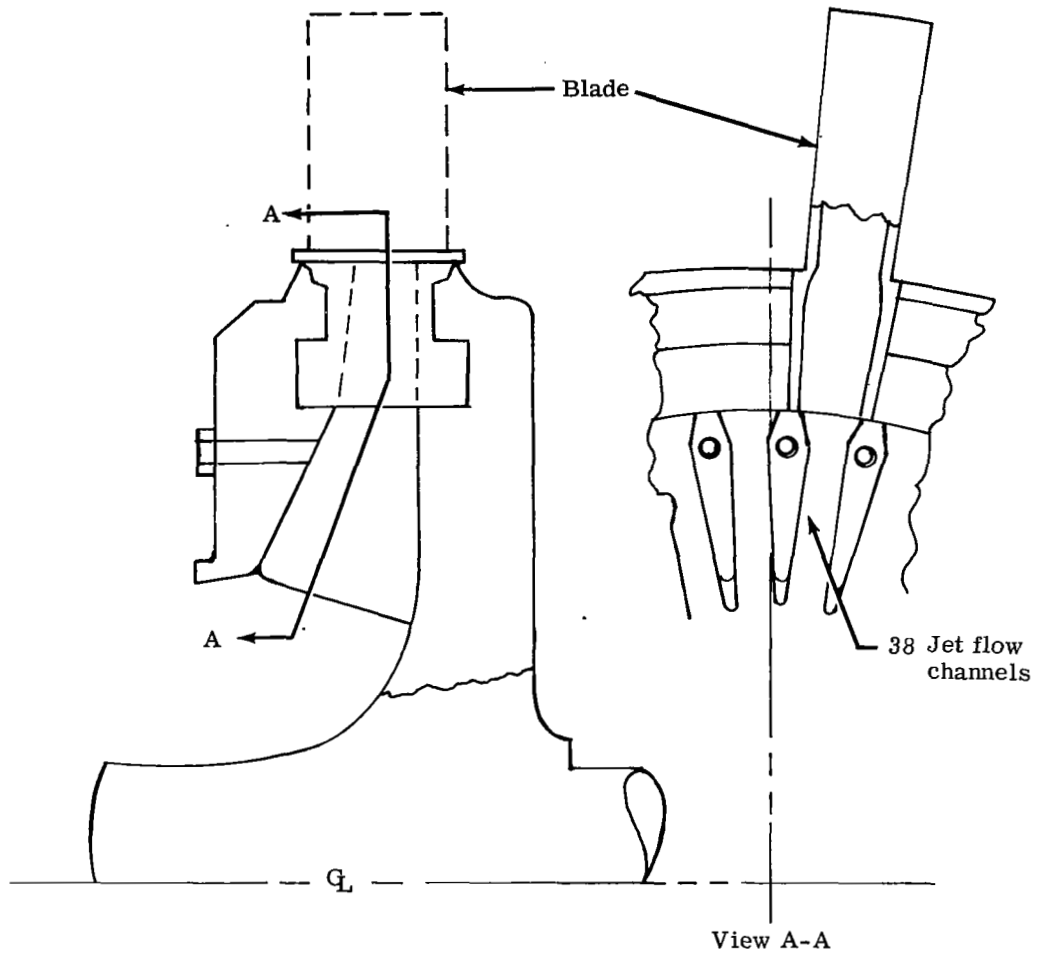


Figure 3. Rotor wheel assembly schematic.

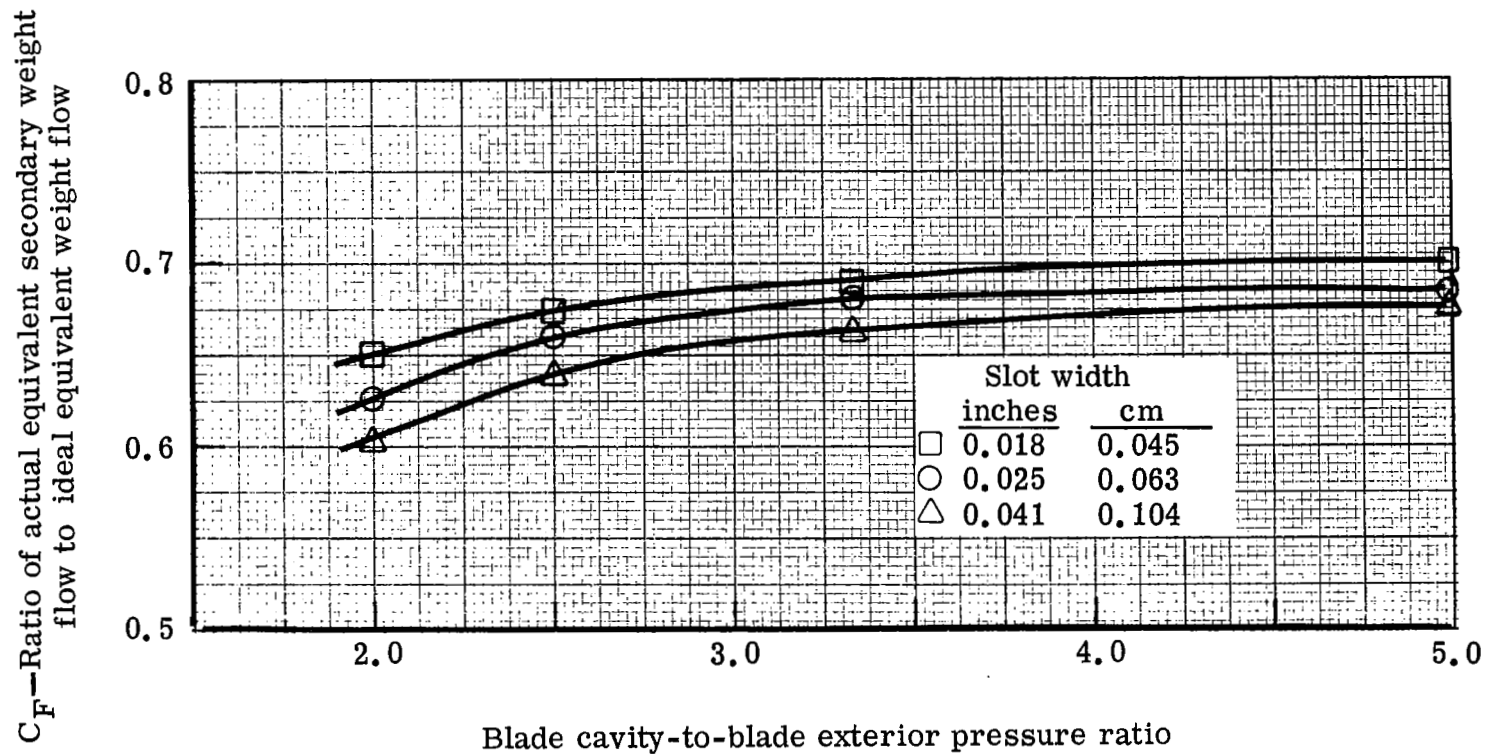
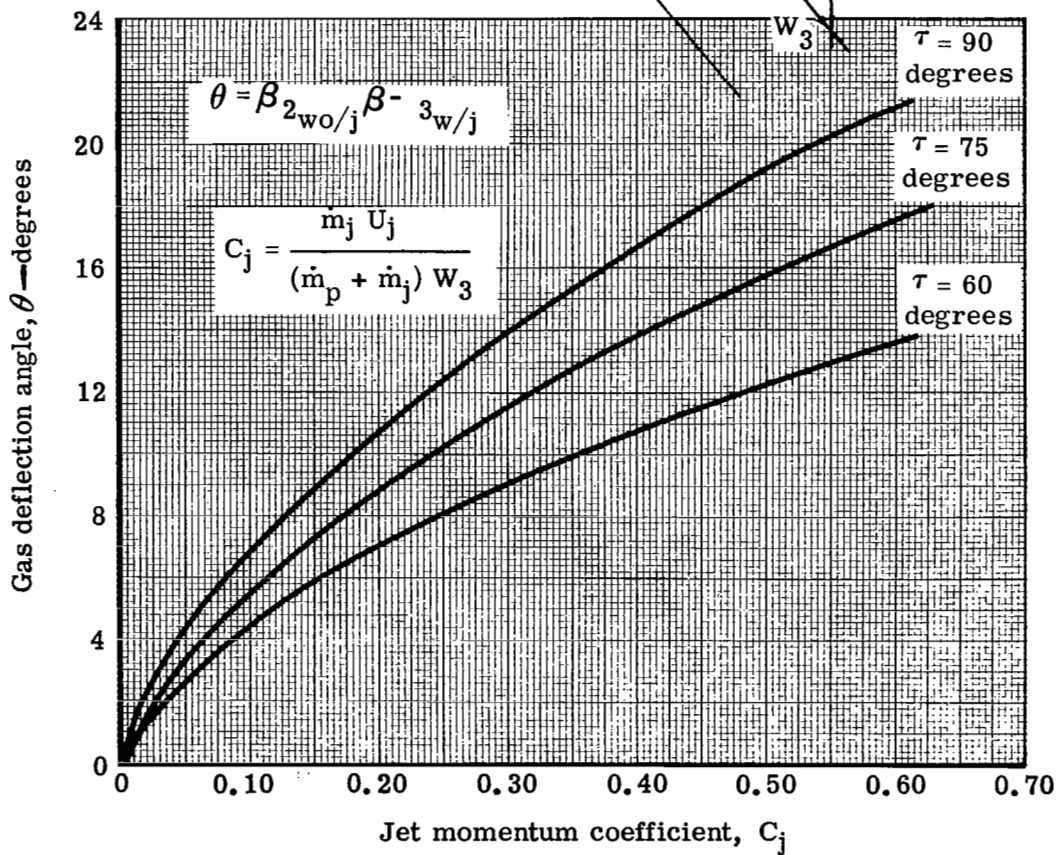


Figure 4. Variation of jet flap blade slot coefficient with slot pressure ratio for lines of slot width.



51

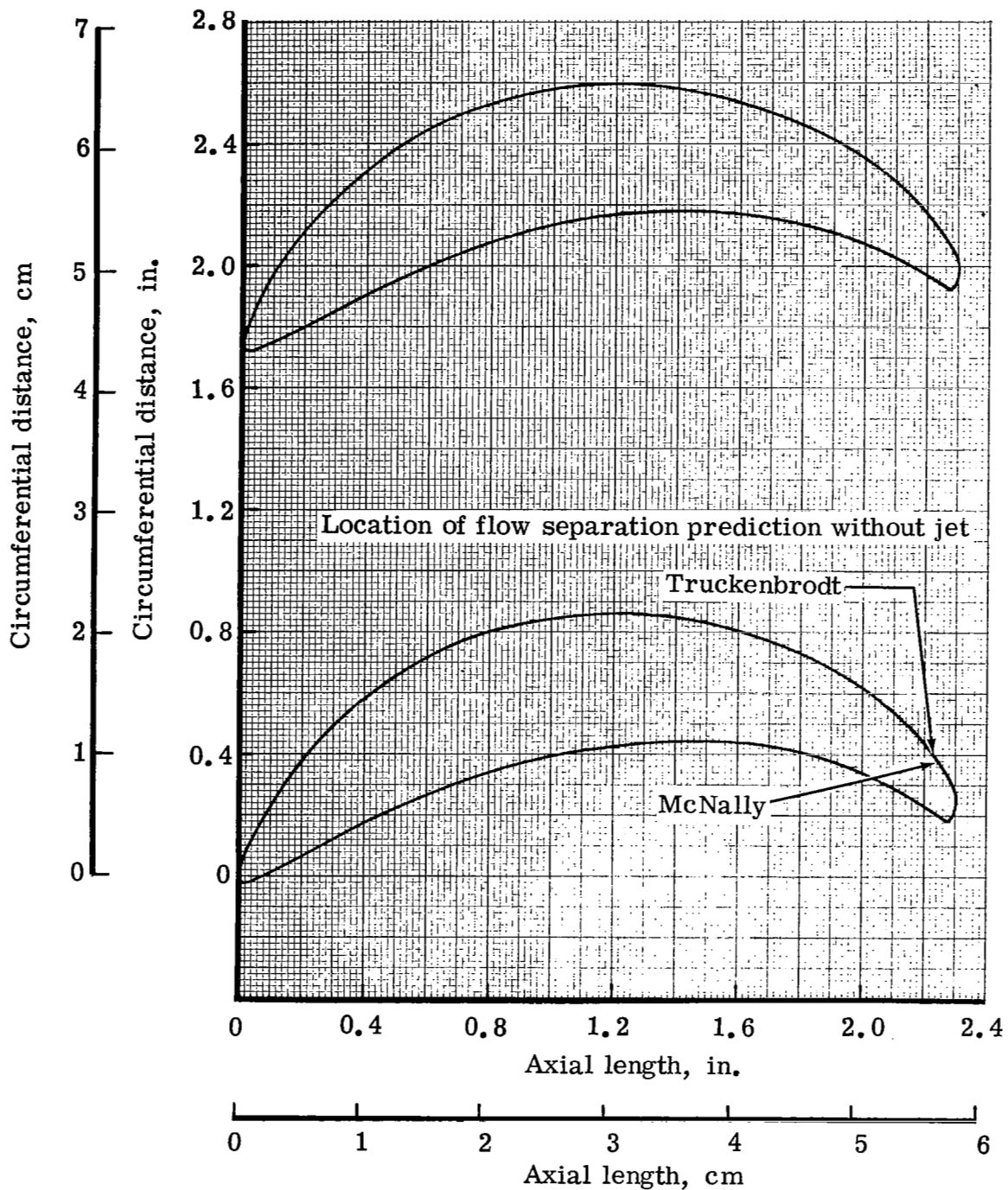


Figure 6. Jet flap blade hub section profile.

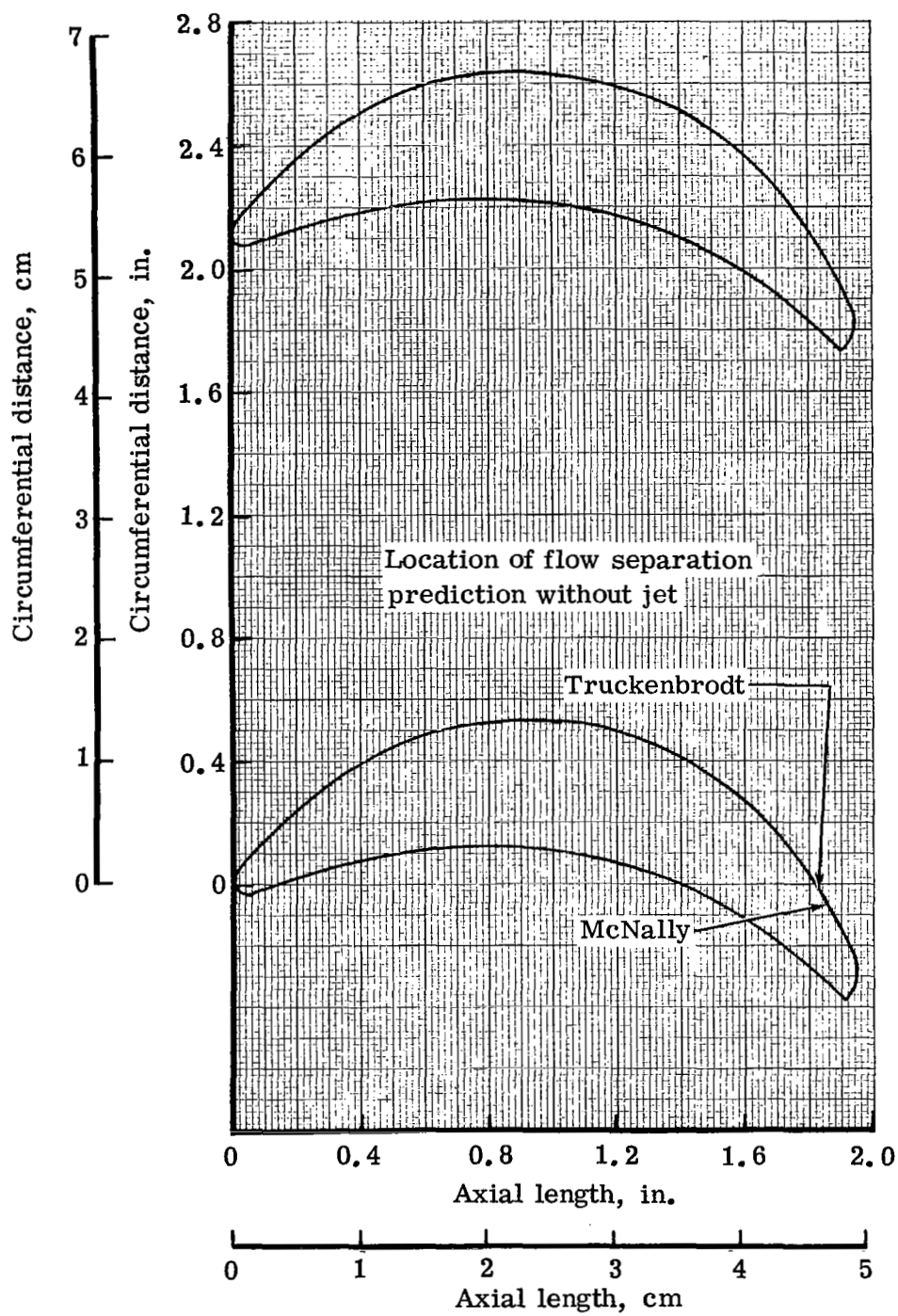


Figure 7. Jet flap blade mean section profile.

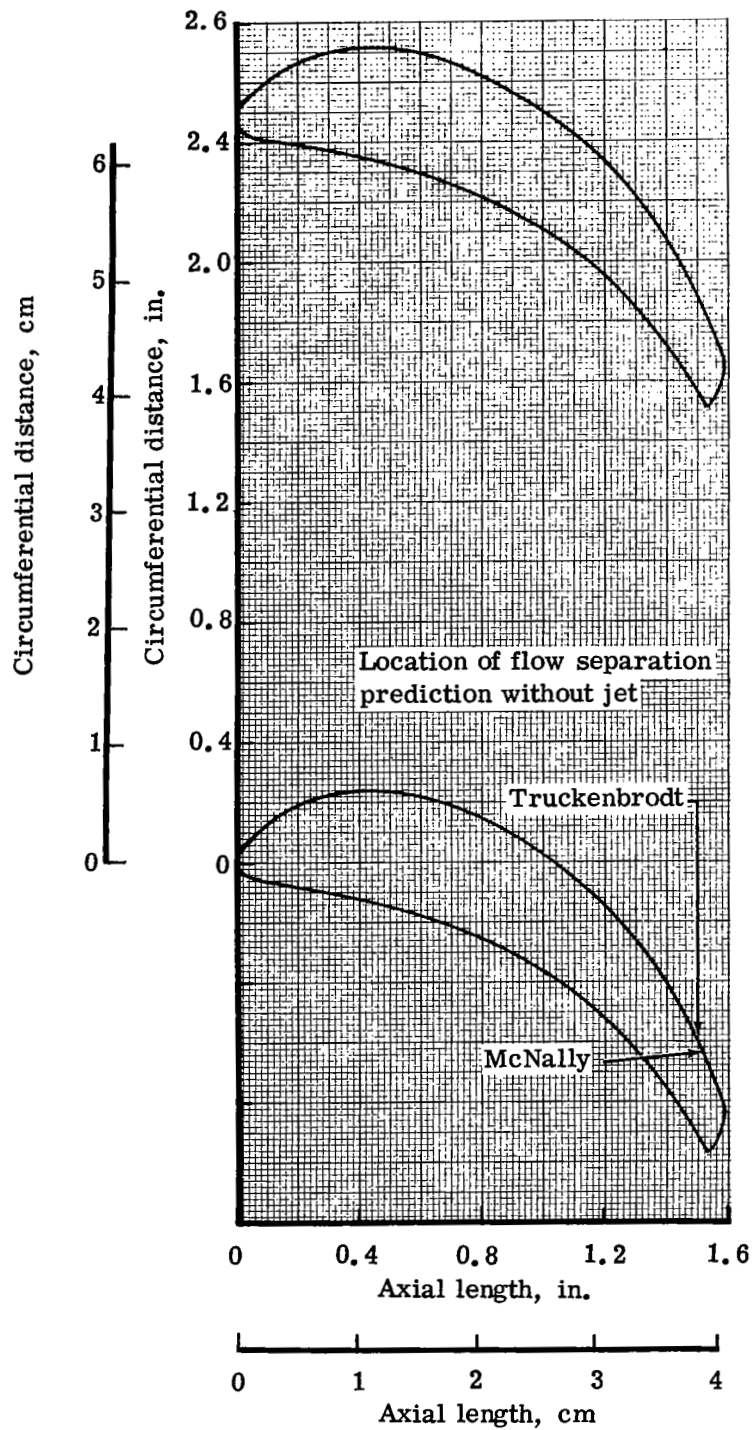


Figure 8. Jet flap blade tip section profile.

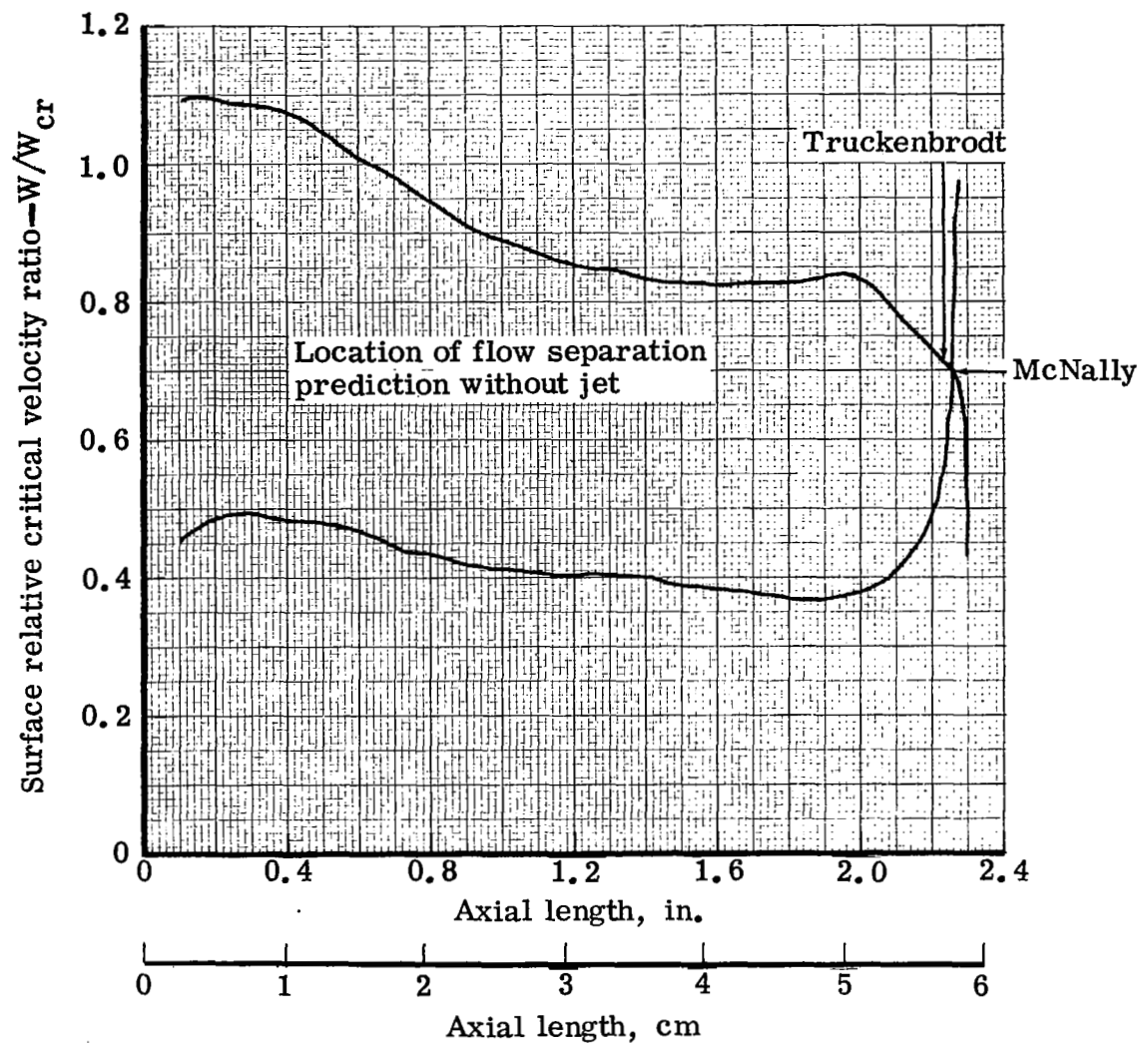


Figure 9. Jet flap blade hub section surface critical velocity ratio with jet off.

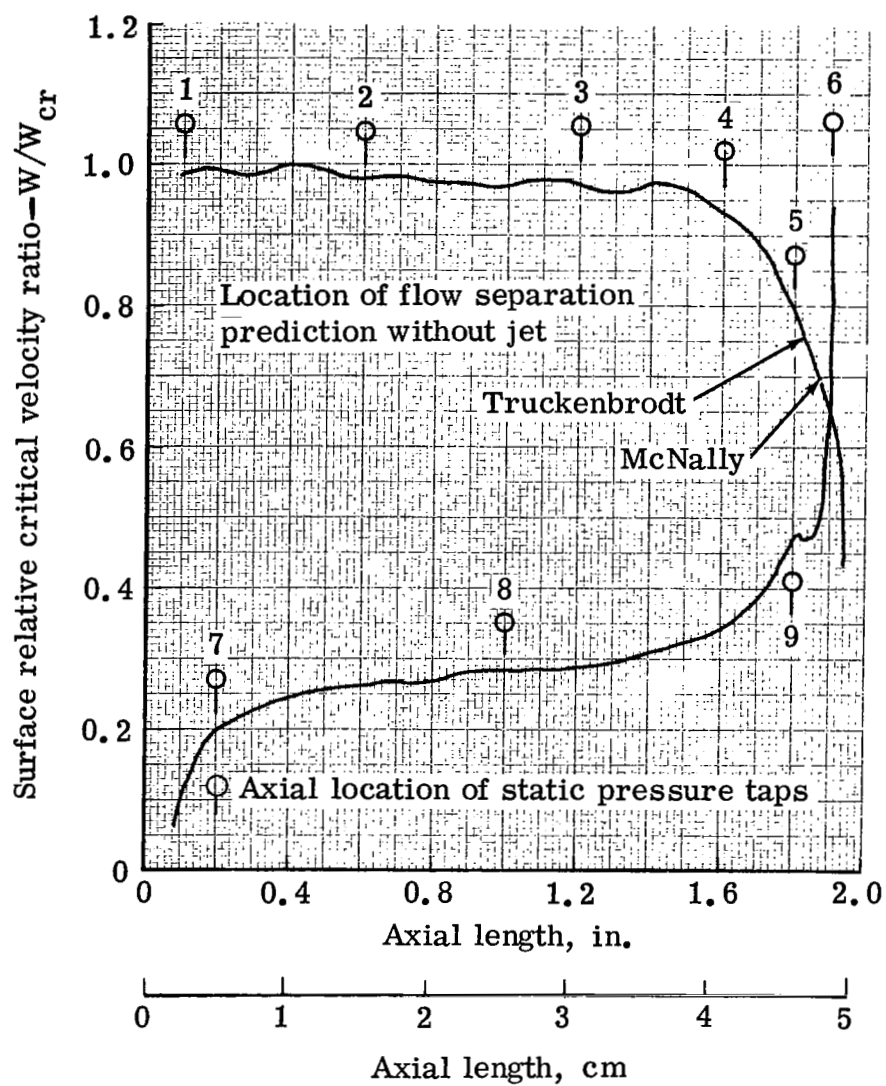


Figure 10. Jet flap blade mean section surface critical velocity ratio jet off.

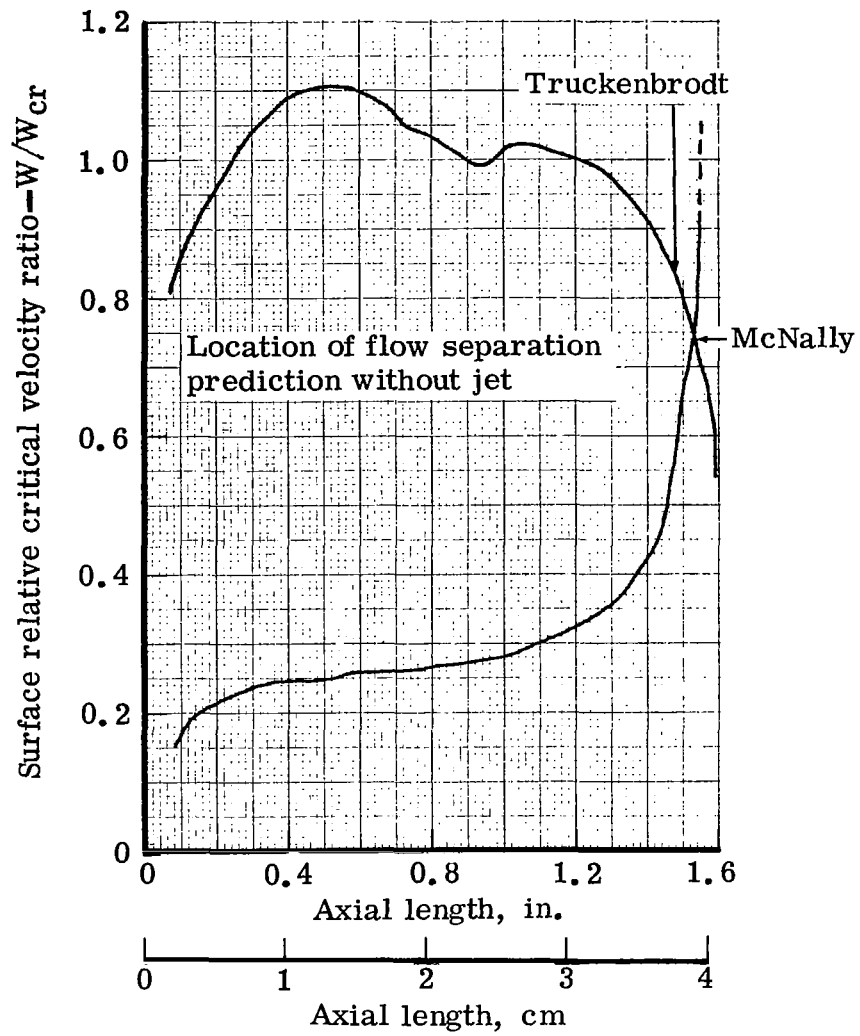


Figure 11. Jet flap blade tip section surface critical velocity ratio with jet off.

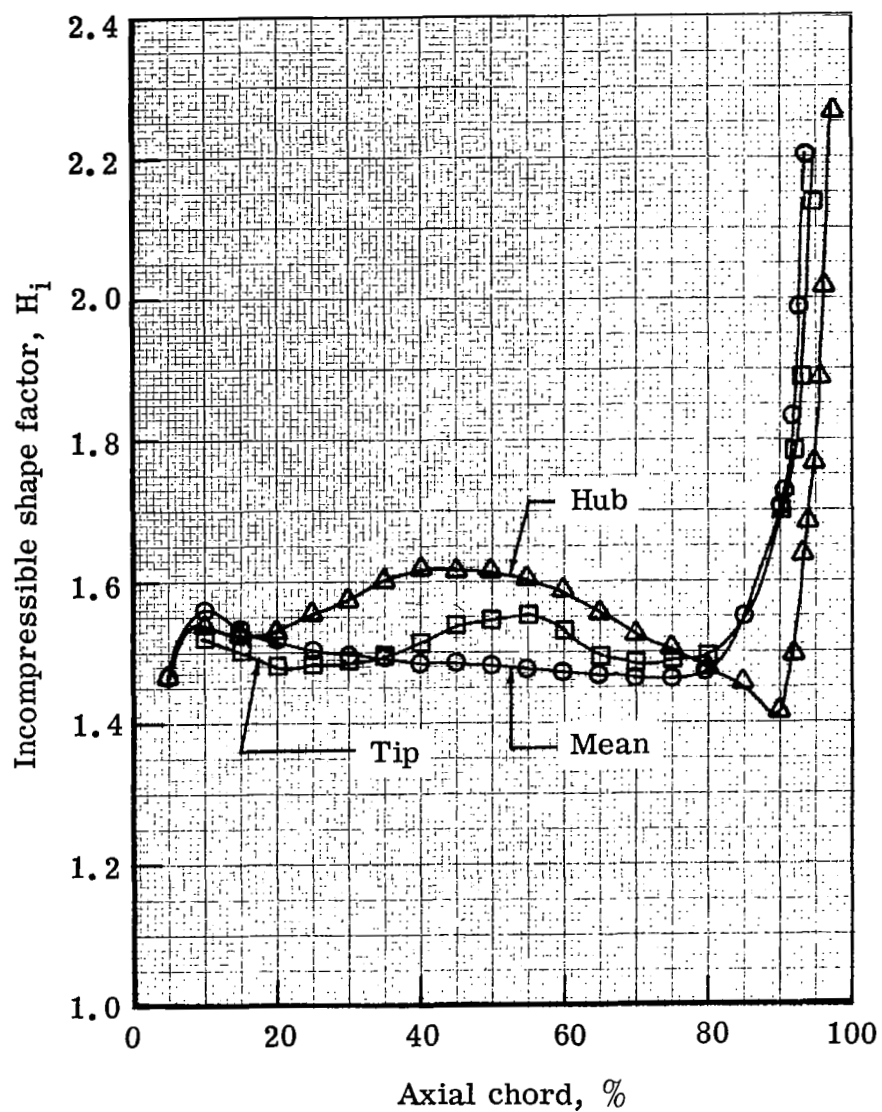


Figure 12. Jet flap blade suction surface incompressible shape factor distribution with jet off.

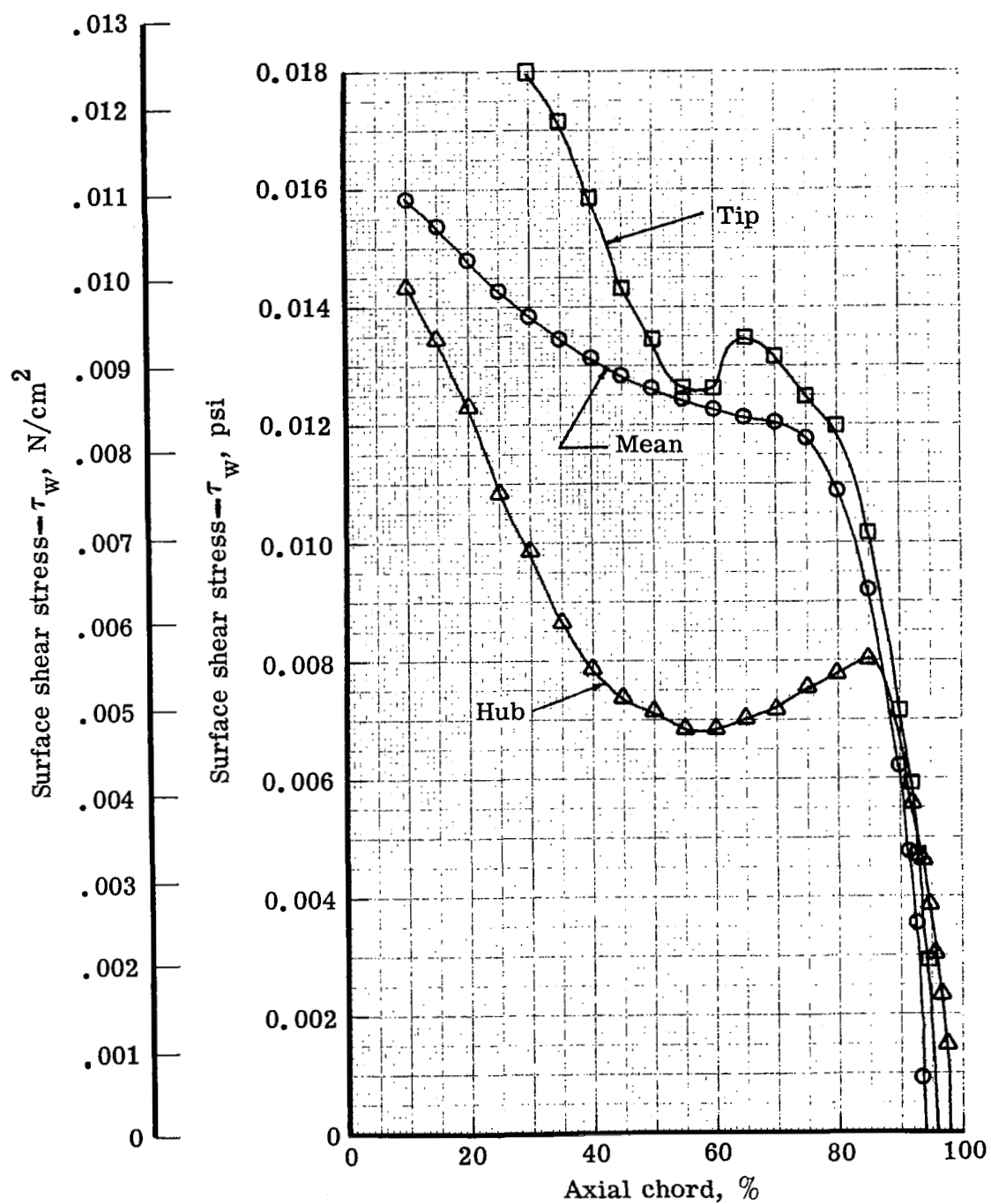


Figure 13. Jet flap blade suction surface wall shear stress distribution with jet off.

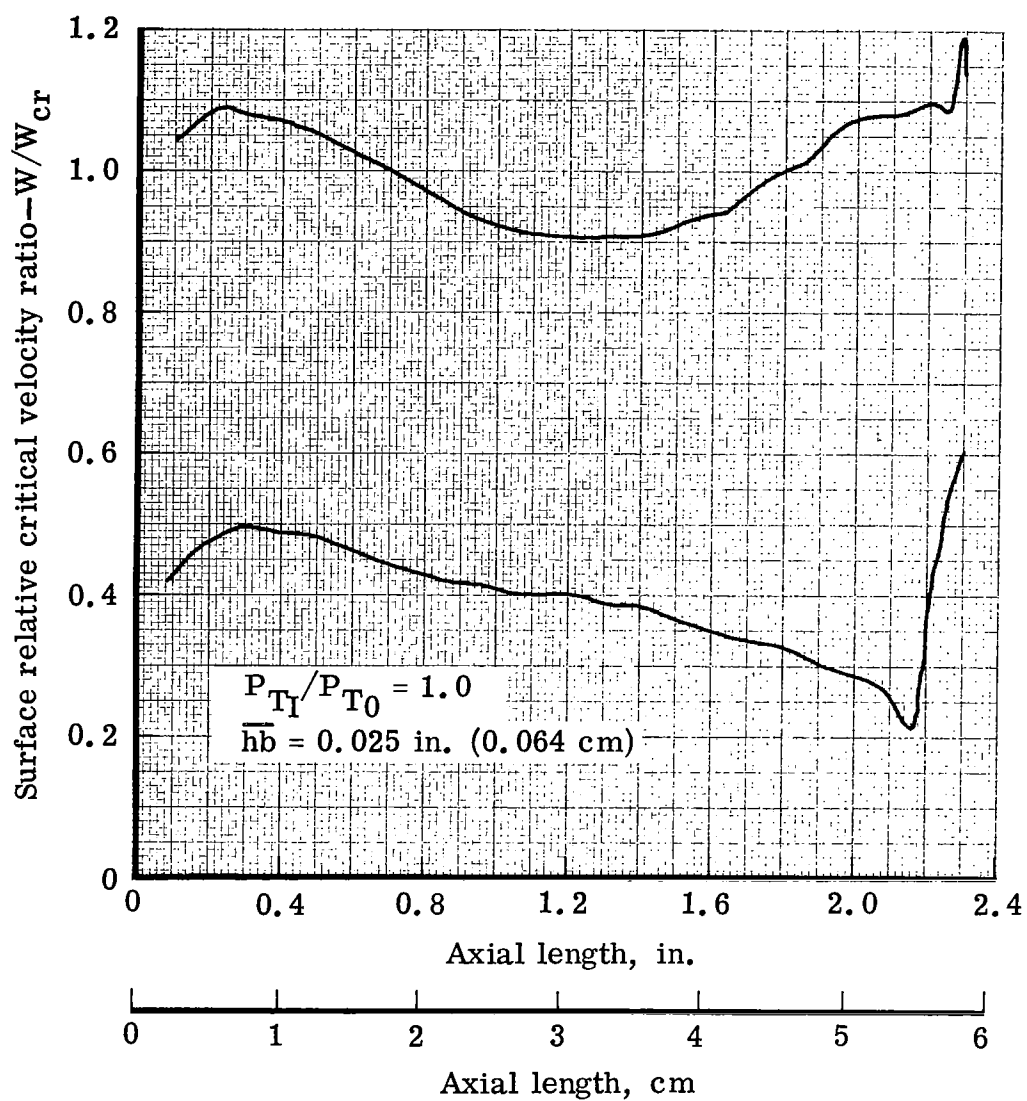


Figure 14. Jet flap blade hub section surface critical velocity ratio with jet on.

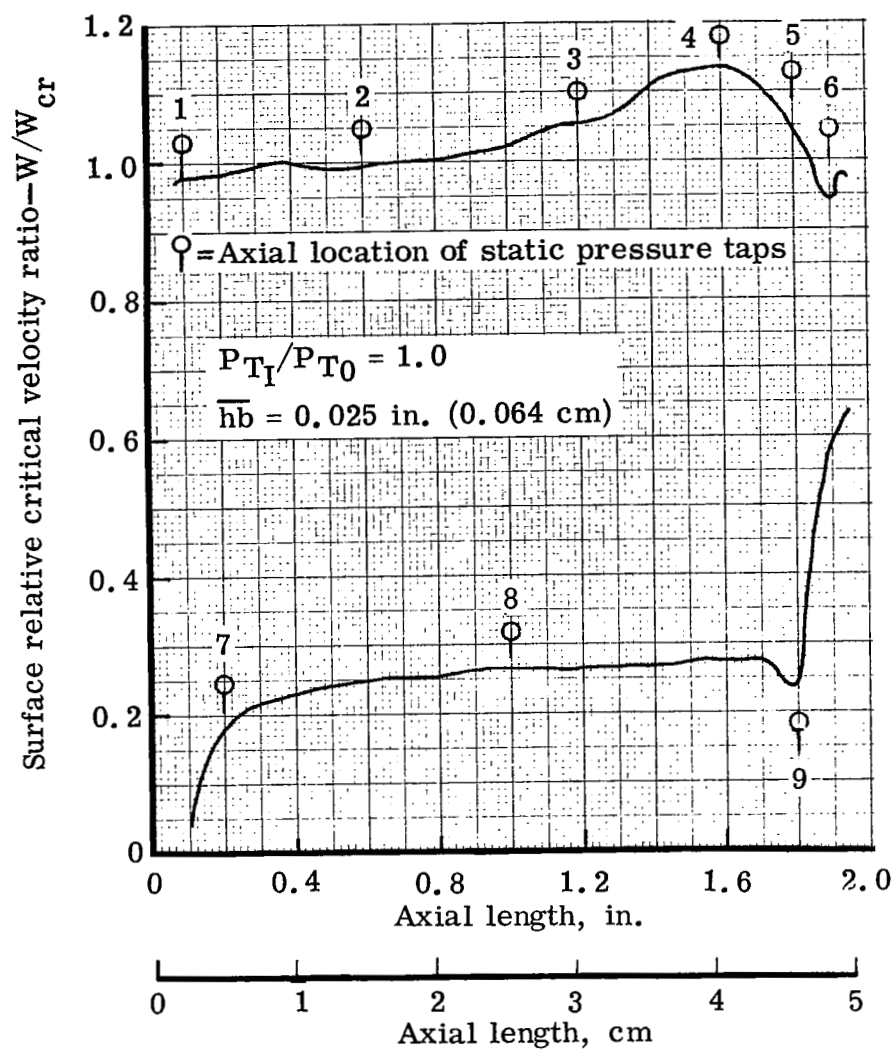


Figure 15. Jet flap blade mean section surface critical velocity ratio with jet on.

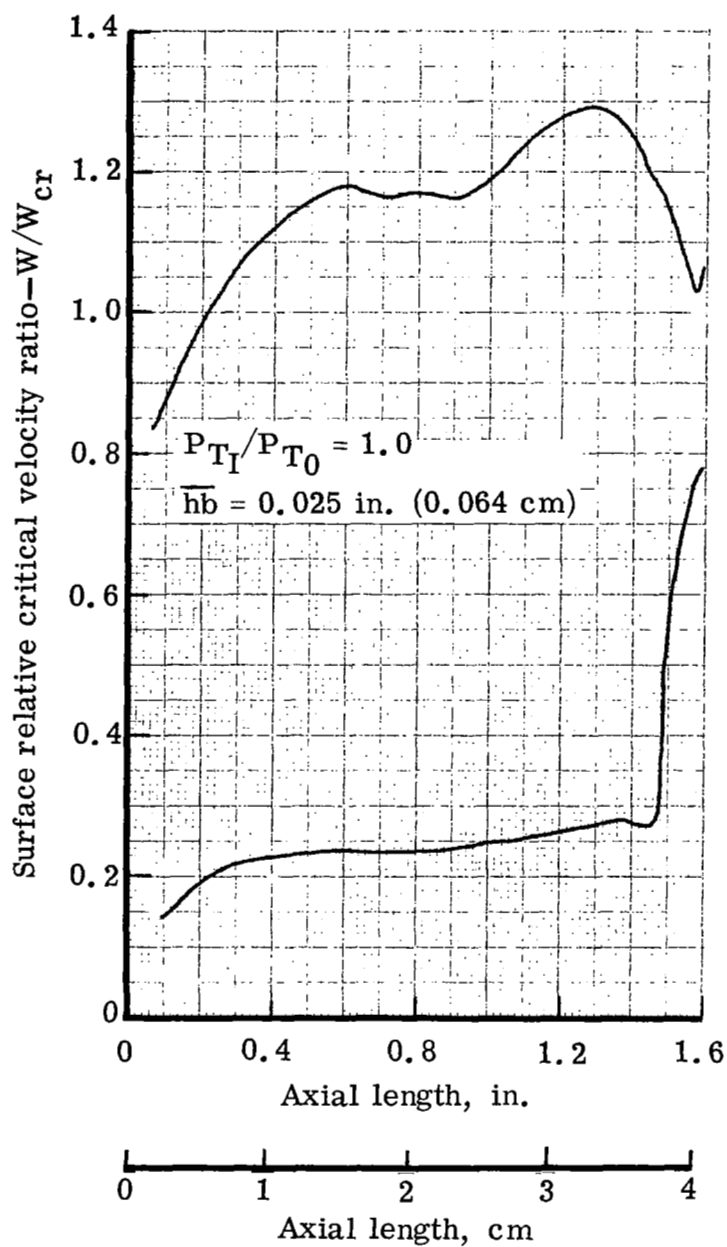


Figure 16. Jet flap blade tip section surface critical velocity ratio with jet on.

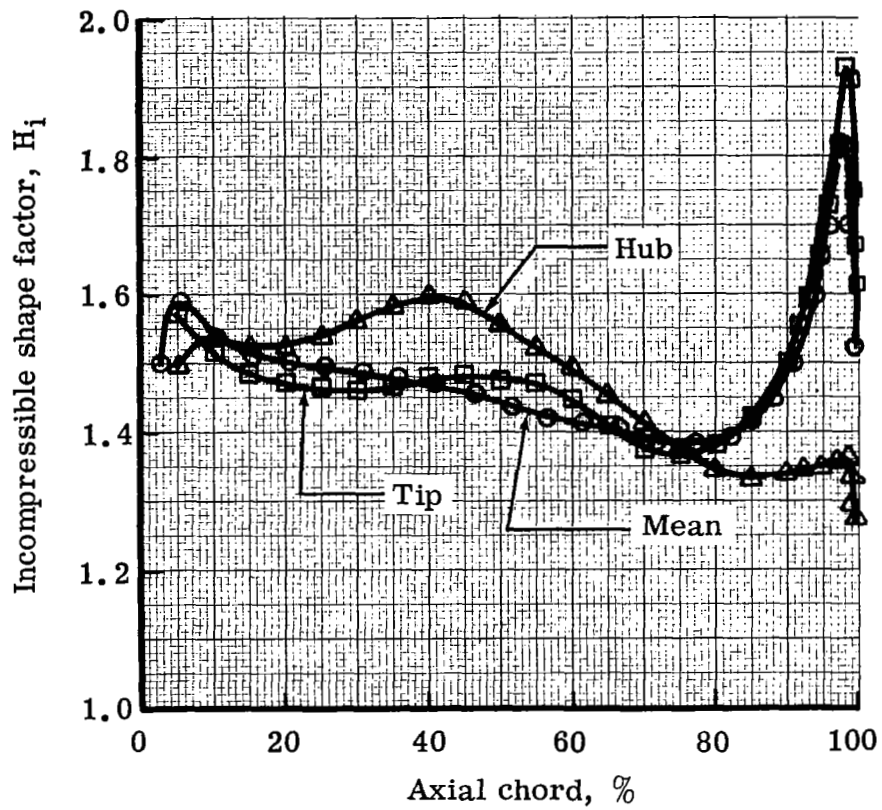


Figure 17. Jet flap blade suction surface incompressible shape factor distribution with jet on.

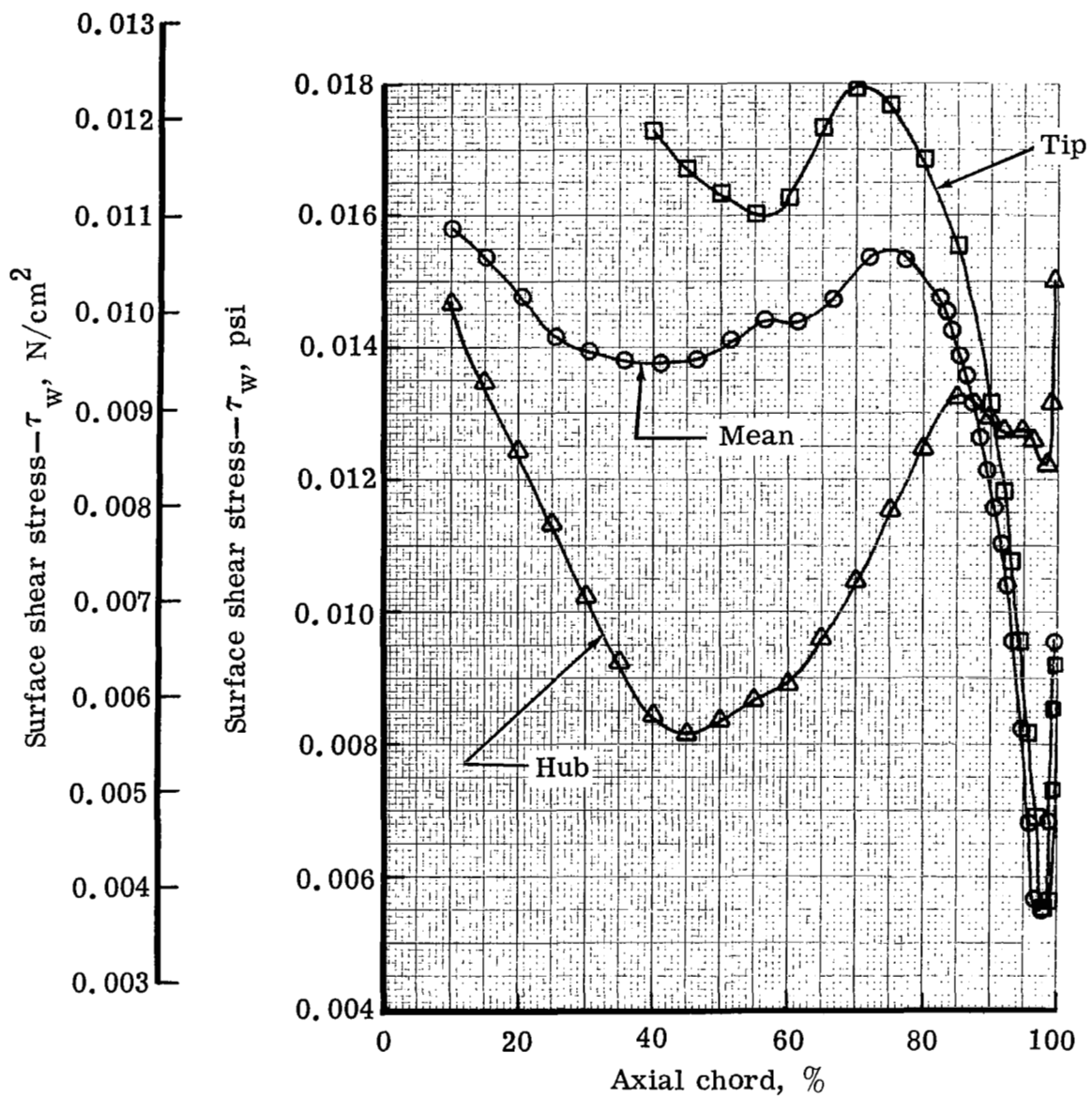


Figure 18. Jet flap blade suction surface wall shear stress distribution with jet on.

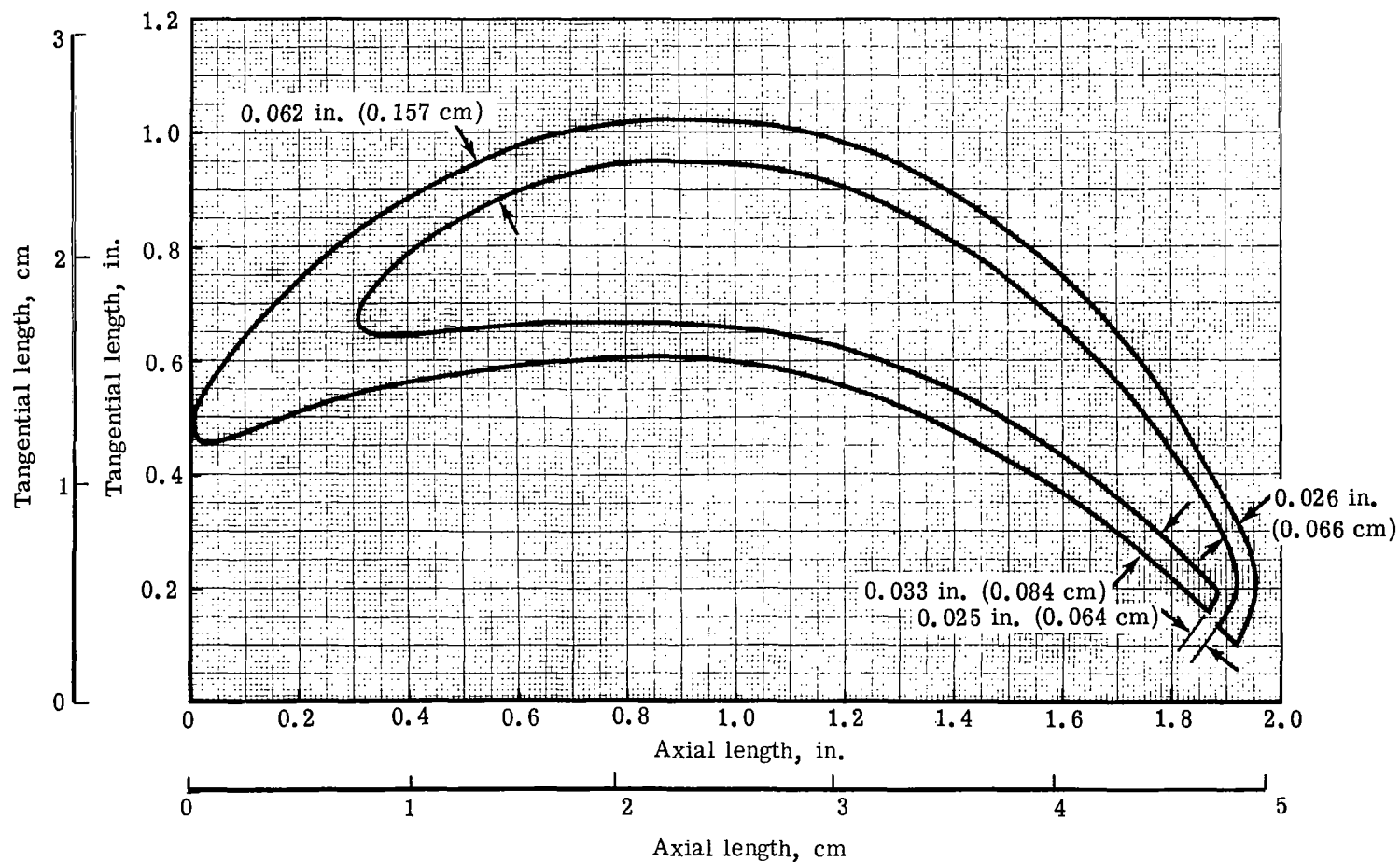


Figure 19. Jet flap blade mean section showing cavity geometry.

At hub section

Area = 0.45 in.² (2.90 cm²)

Total pressure = 16.259 psia (11.21 N/cm²)

Total temperature = 533.88°R (296.6°K)

$\dot{m}_j = 1.098/38 \text{ lb}_m/\text{sec}$ (0.013 kg/sec)

Radial Mach No. = 0.10

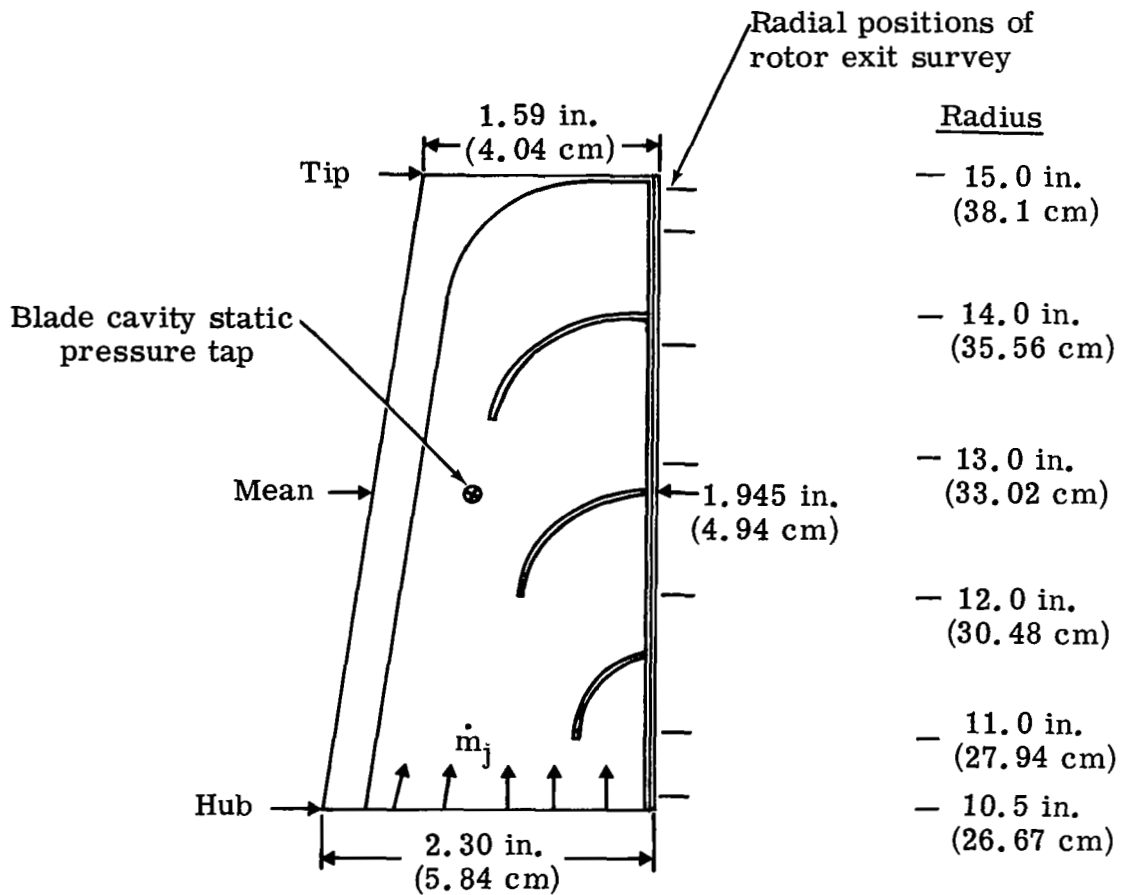


Figure 20. Jet flap blade interior baffle arrangement.

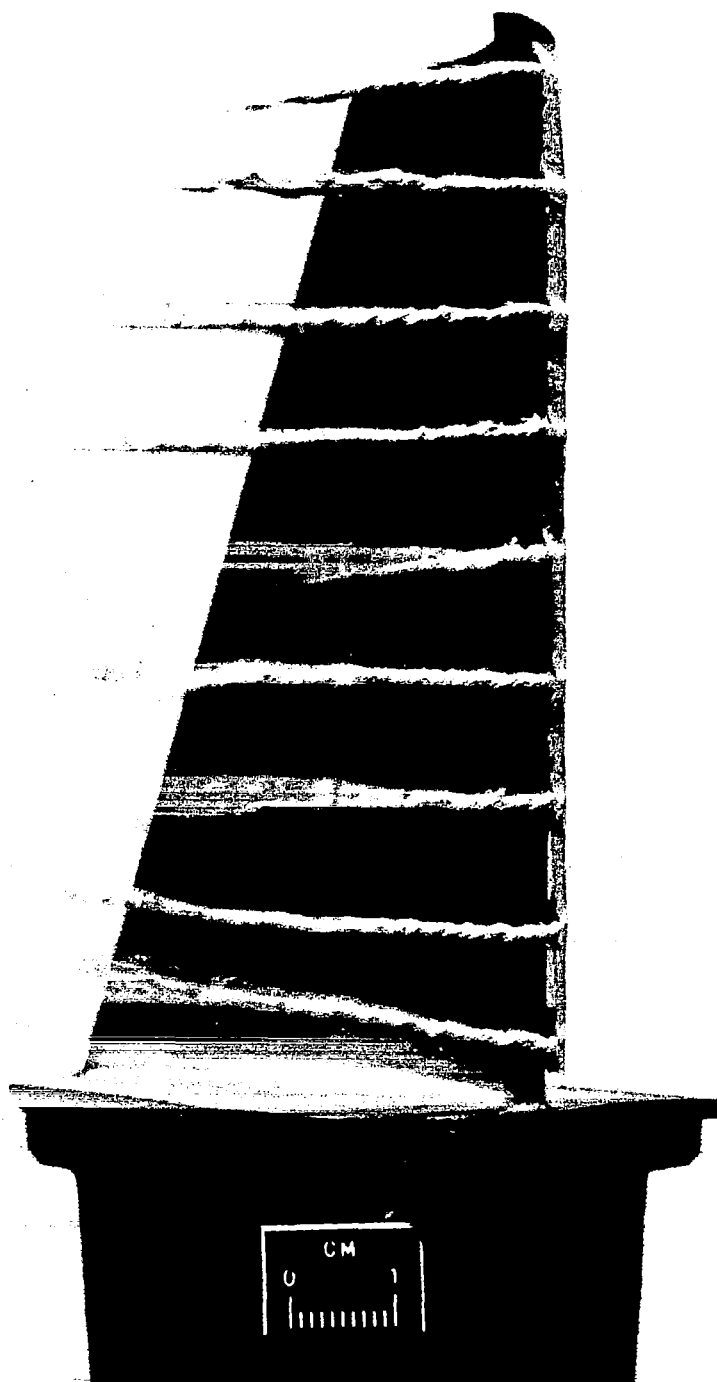
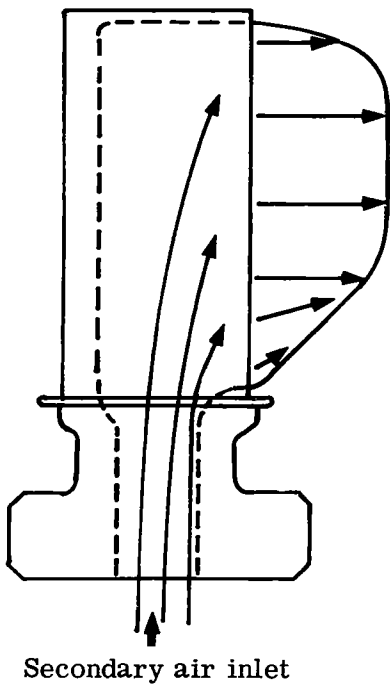
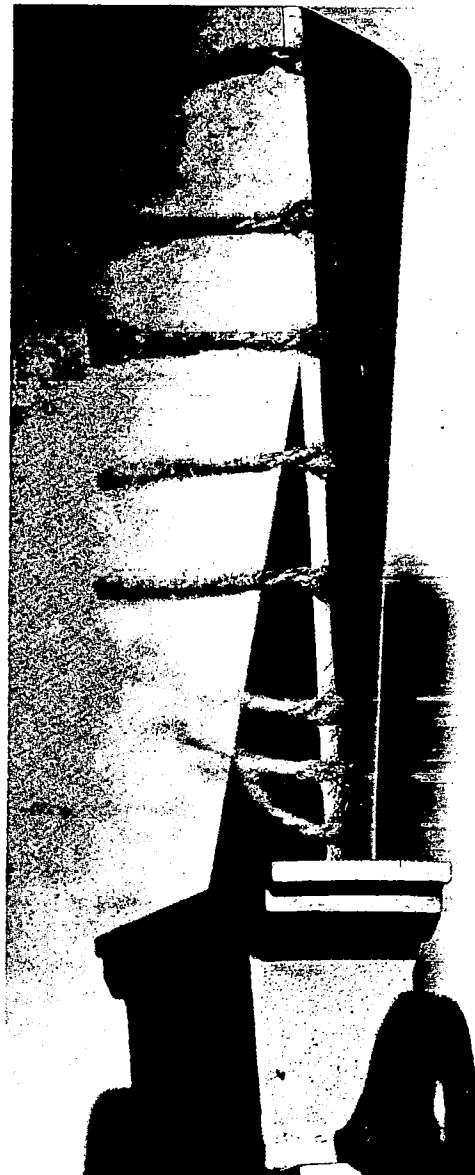


Figure 21. Low solidity jet flap flow distribution as shown by trailing edge tufts.



a. Schematic of jet flap flow pattern



b. Jet flap flow pattern as shown by tufts

Figure 22. Reference 2 jet flap flow pattern.

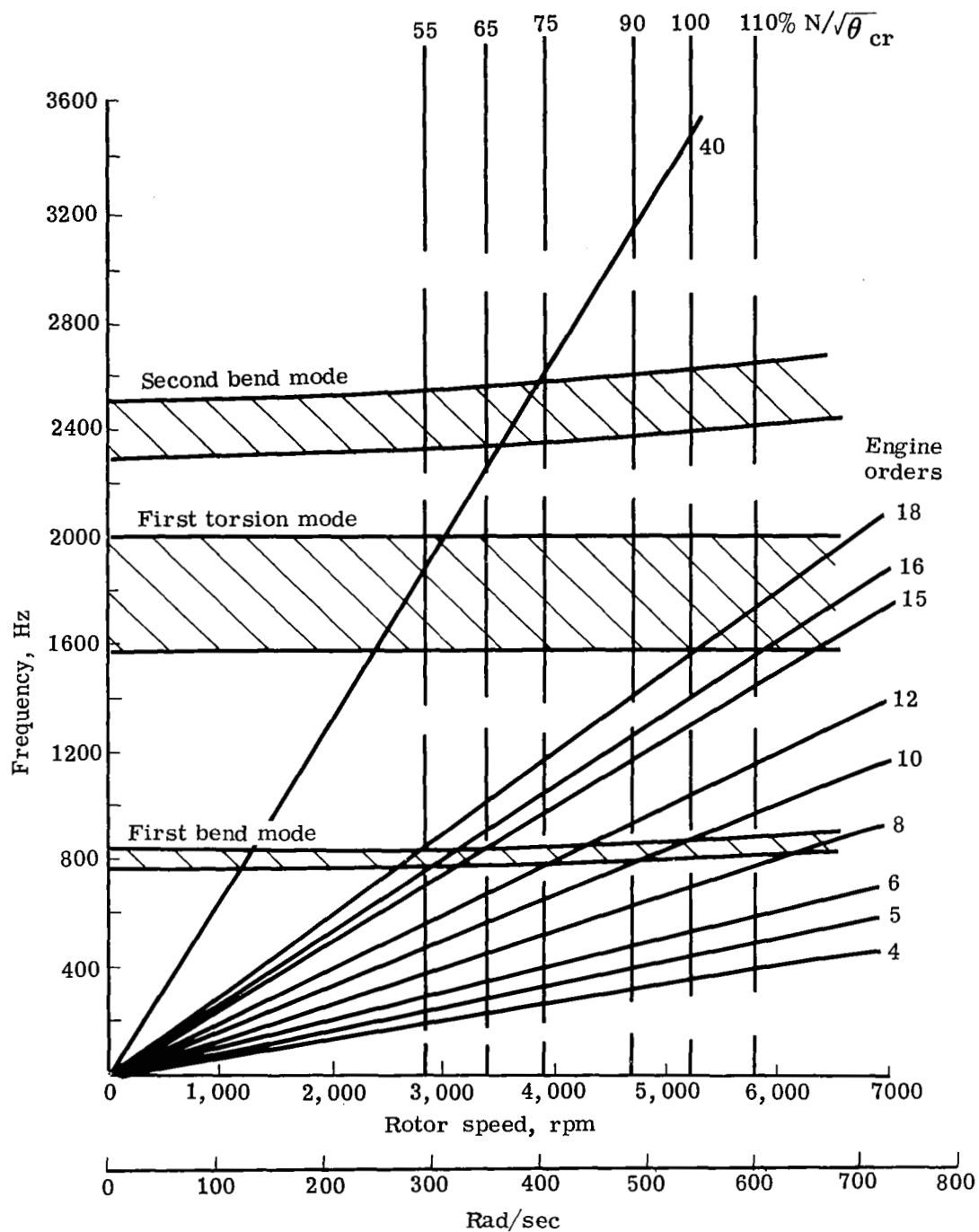


Figure 23. Low solidity jet flap rotor vibrational characteristics.

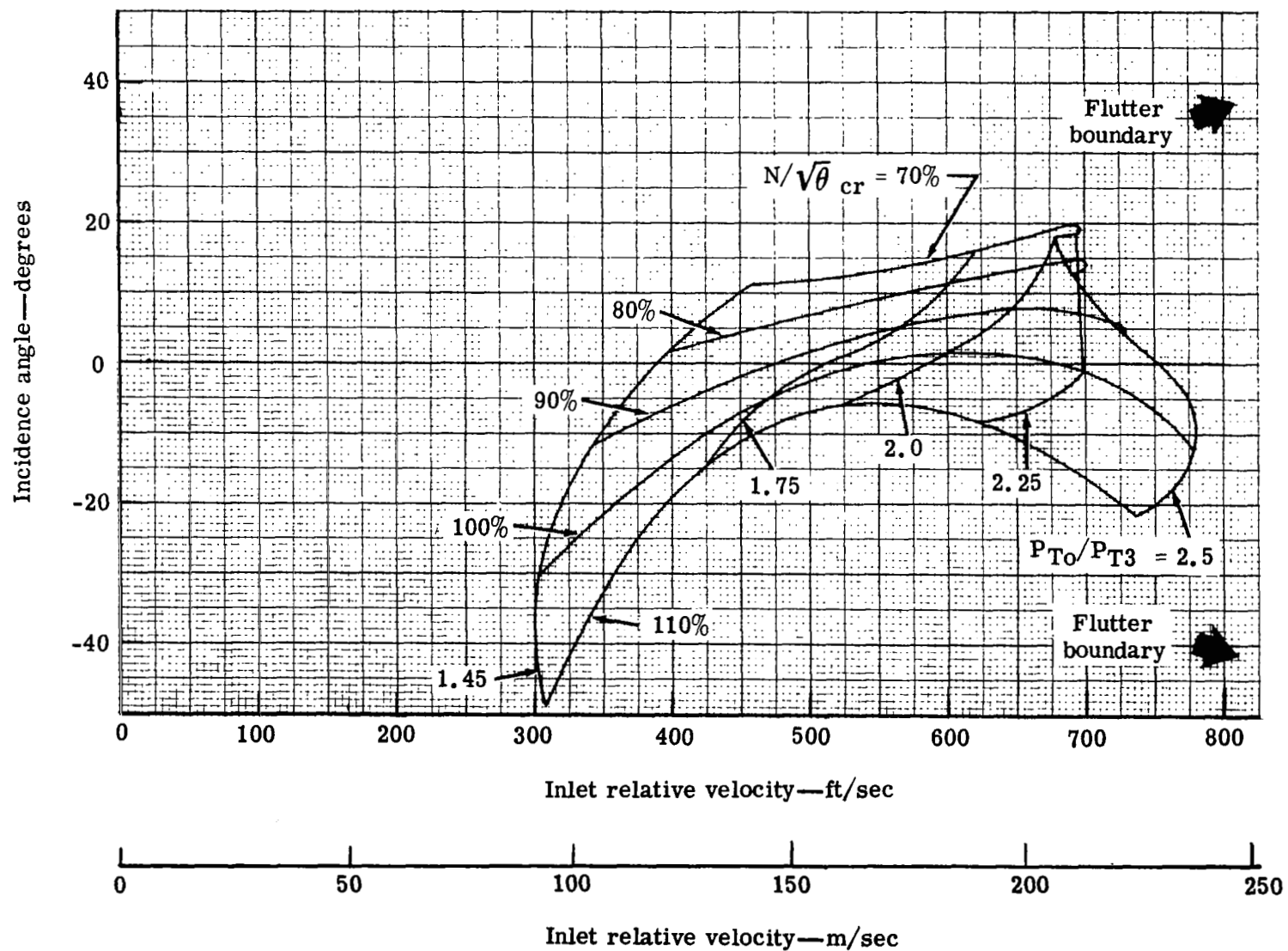


Figure 24. Low solidity jet flap airfoil flutter analysis.



Figure 25. Low solidity jet flap rotor assembly.

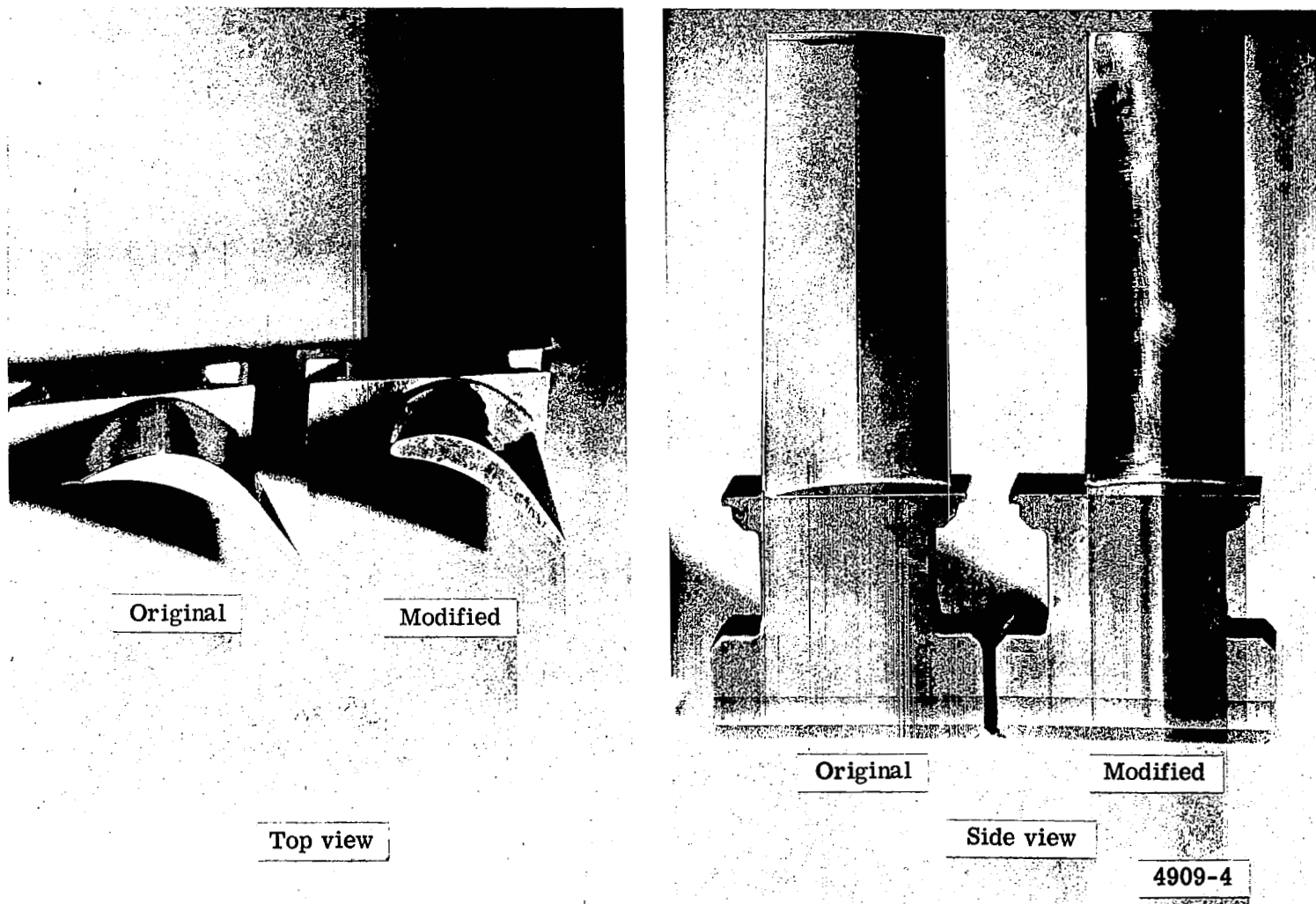


Figure 26. Top and side views of original and modified jet flap rotor blades.

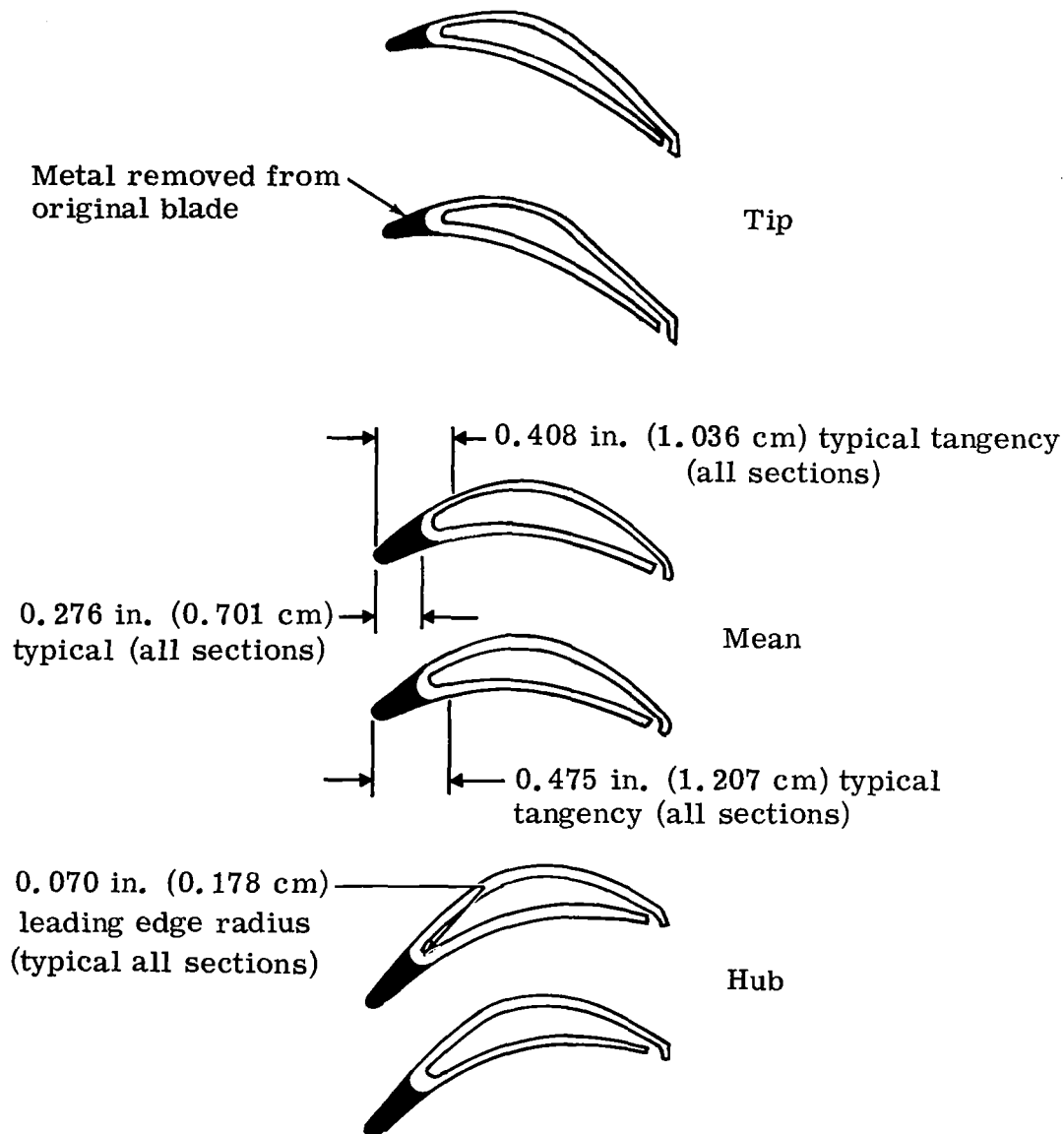


Figure 27. Original and modified jet flap rotor blade profiles and channels.

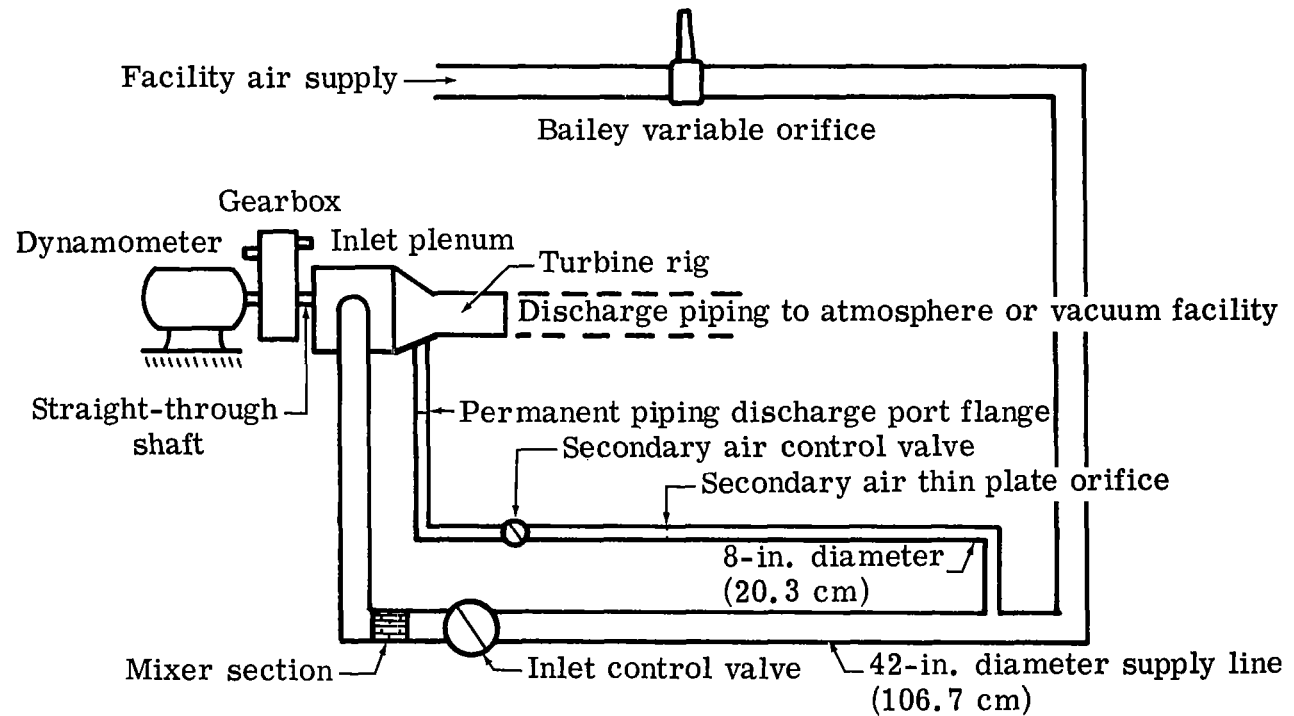


Figure 28. Schematic of test stand air supply system.

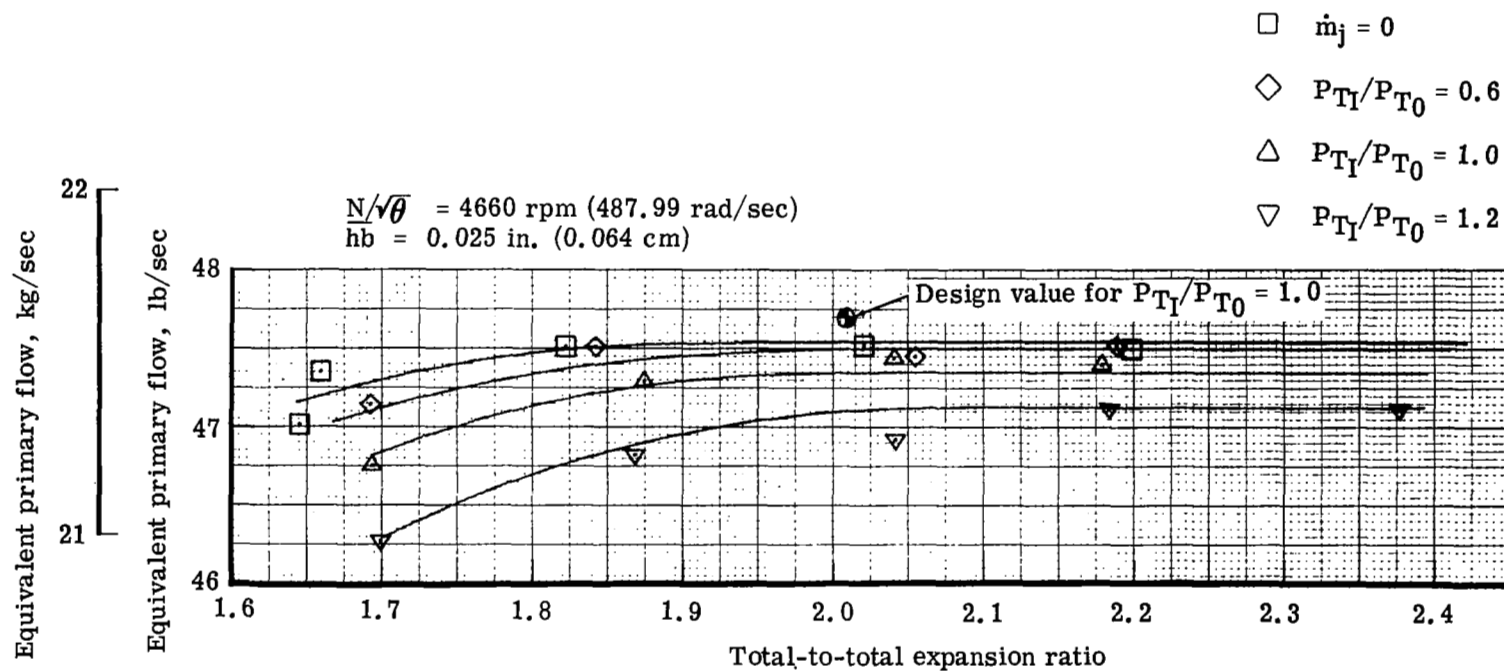


Figure 29. Variation of primary flow with expansion ratio and cavity pressure ratio at design speed.

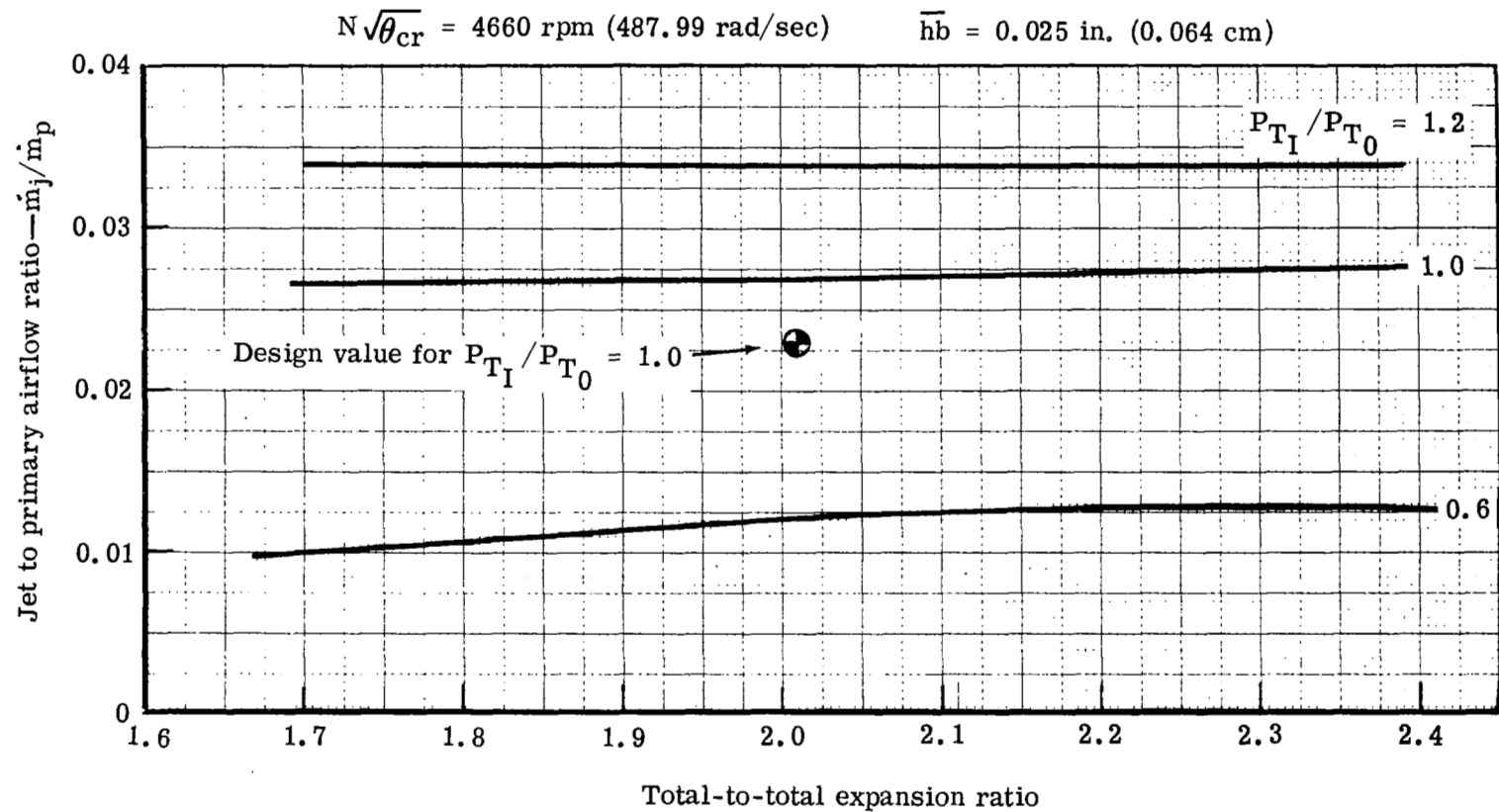


Figure 30. Variation of percent jet flow with expansion ratio and cavity pressure ratio at design speed.

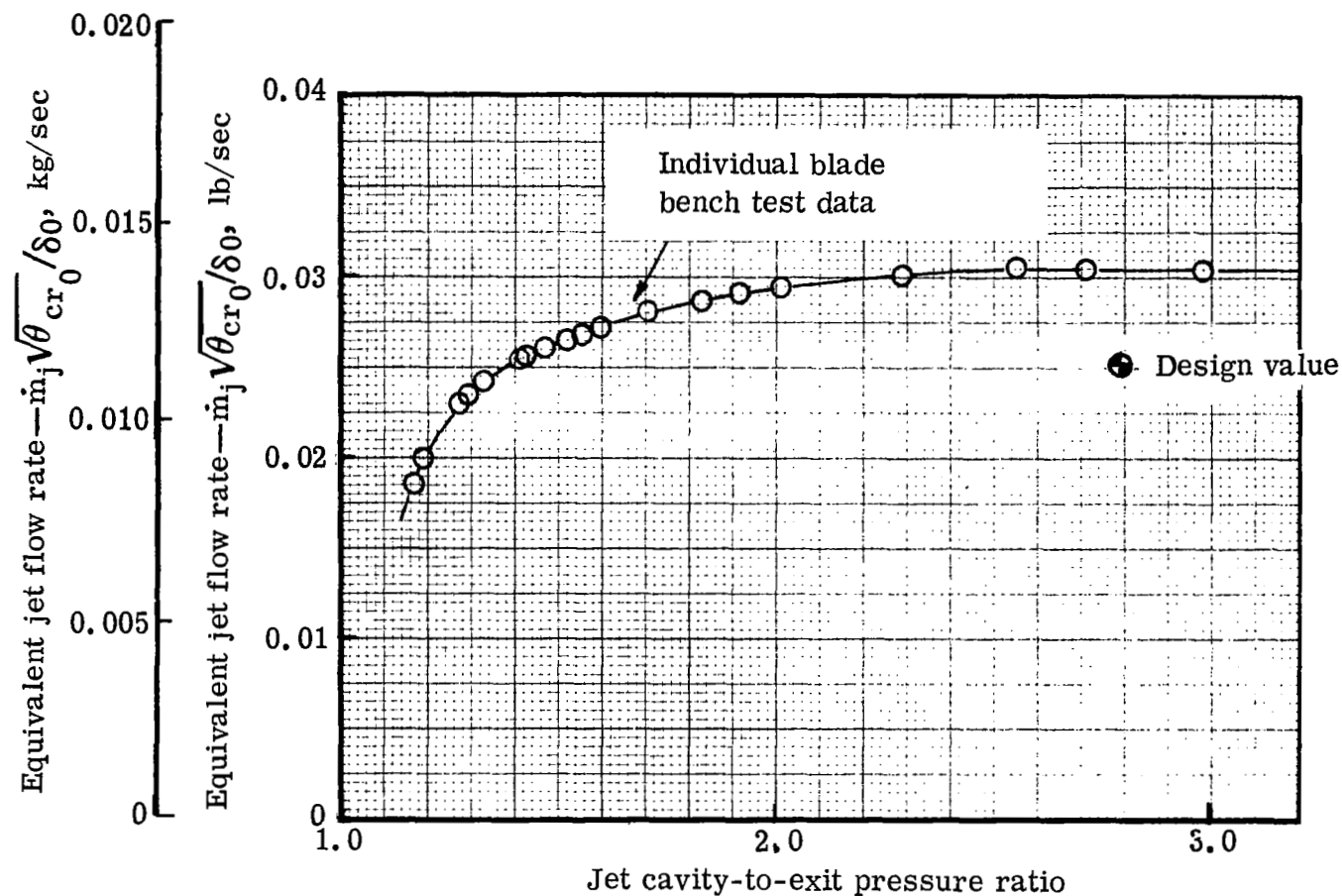


Figure 31. Variation of equivalent jet flow rate with jet cavity-to-exit pressure ratio—comparison of bench test data with design value for low solidity jet flap blade.

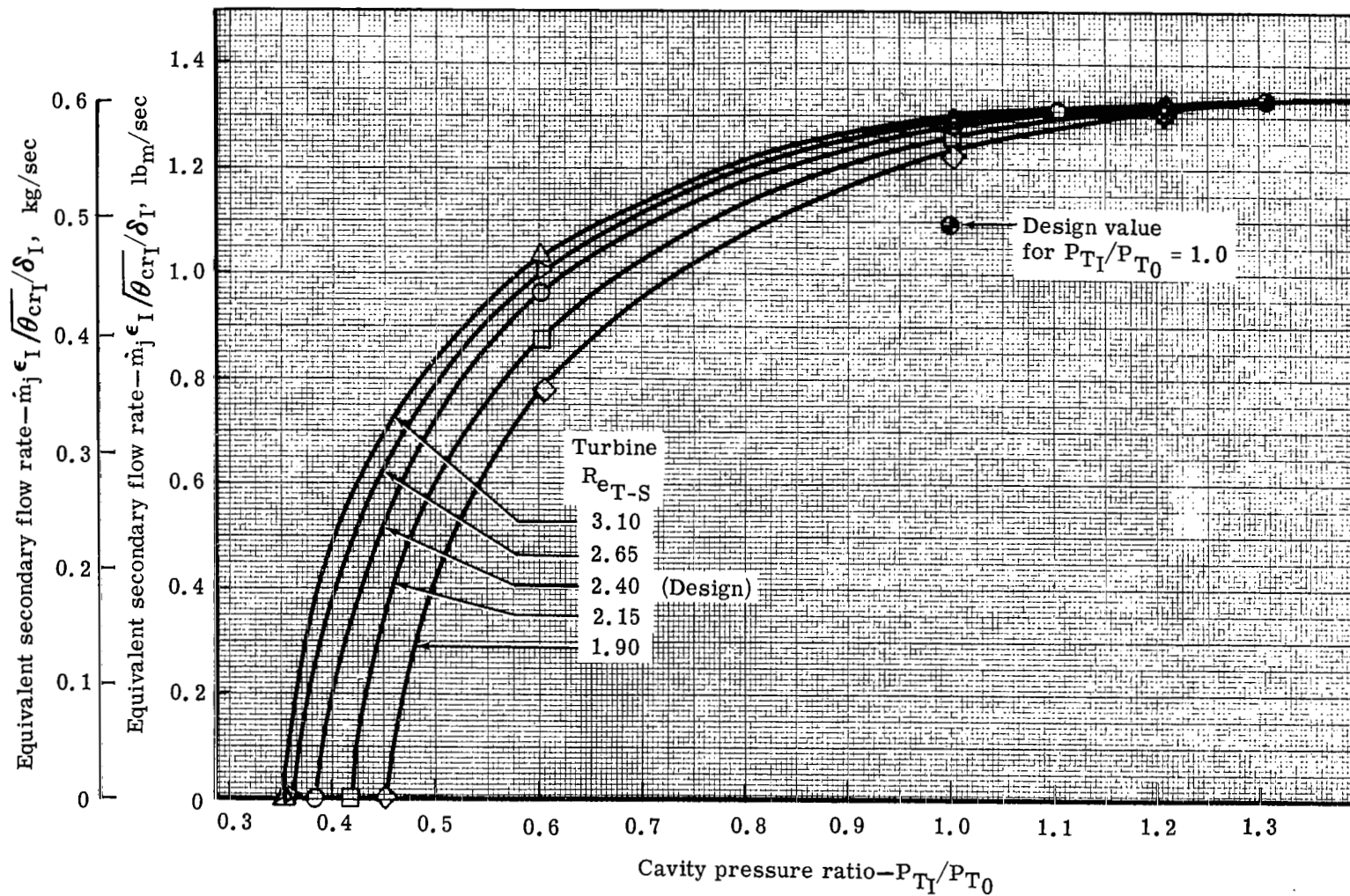


Figure 32. Variation of equivalent jet flow with expansion ratio and cavity pressure ratio at design speed.

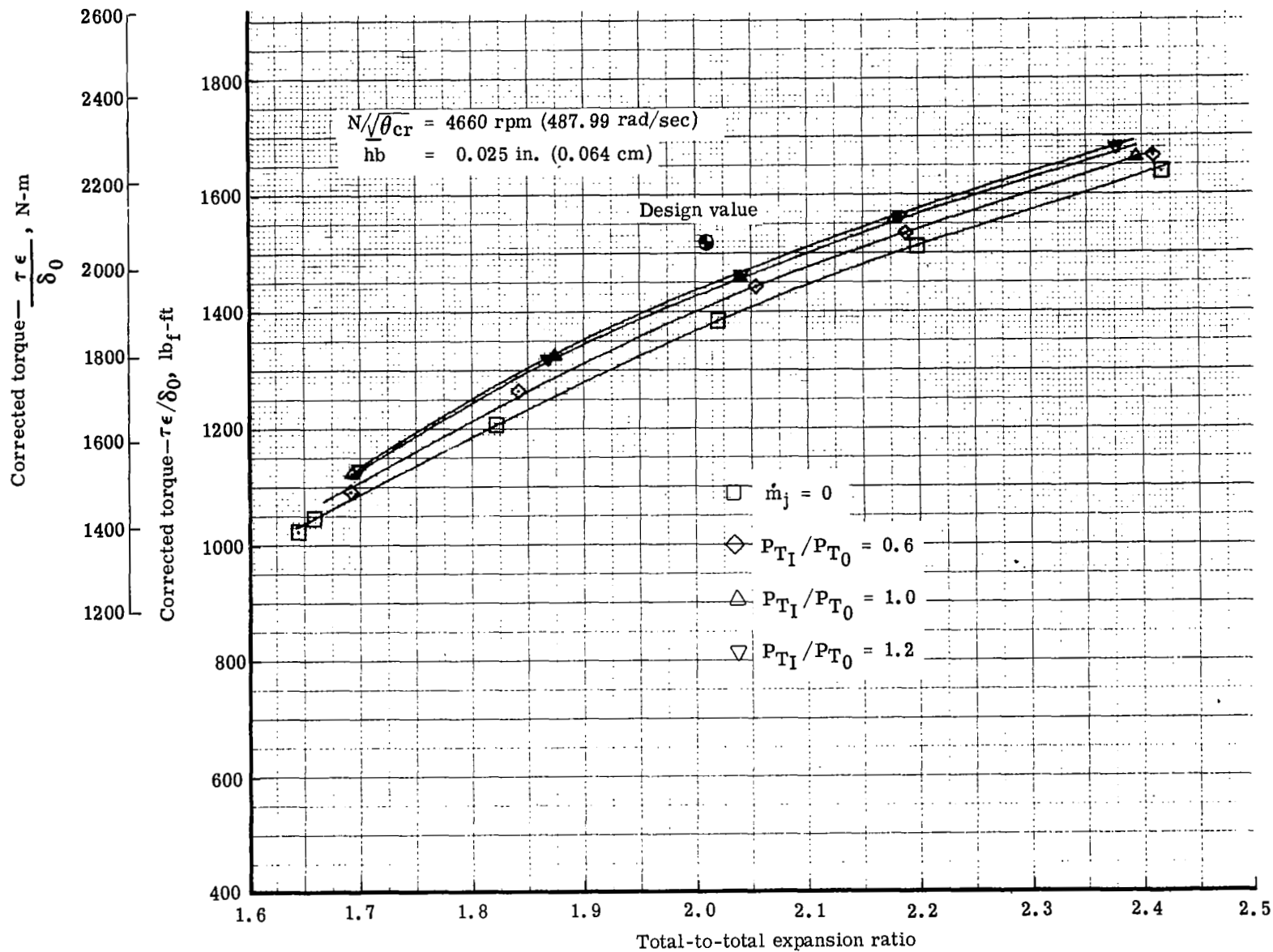


Figure 33. Variation of corrected torque with expansion ratio and cavity pressure ratio at design speed.

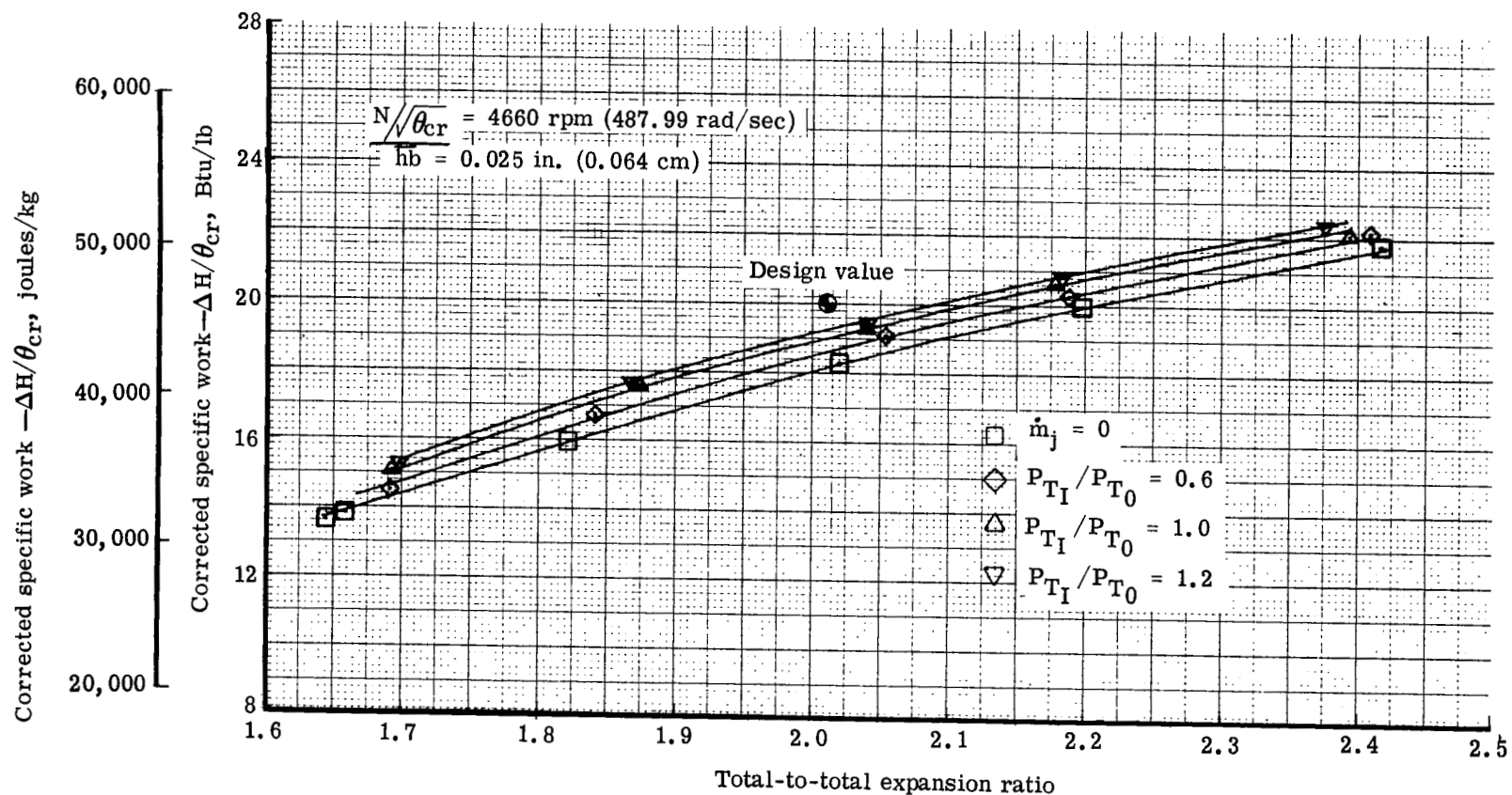


Figure 34. Variation of corrected specific work with expansion ratio and cavity pressure ratio at design speed.

$$N/\sqrt{\theta_{cr}} = 4660 \text{ rpm (487.99 rad/sec)}$$

$$\bar{h}b = 0.025 \text{ in. (0.064 cm)}$$

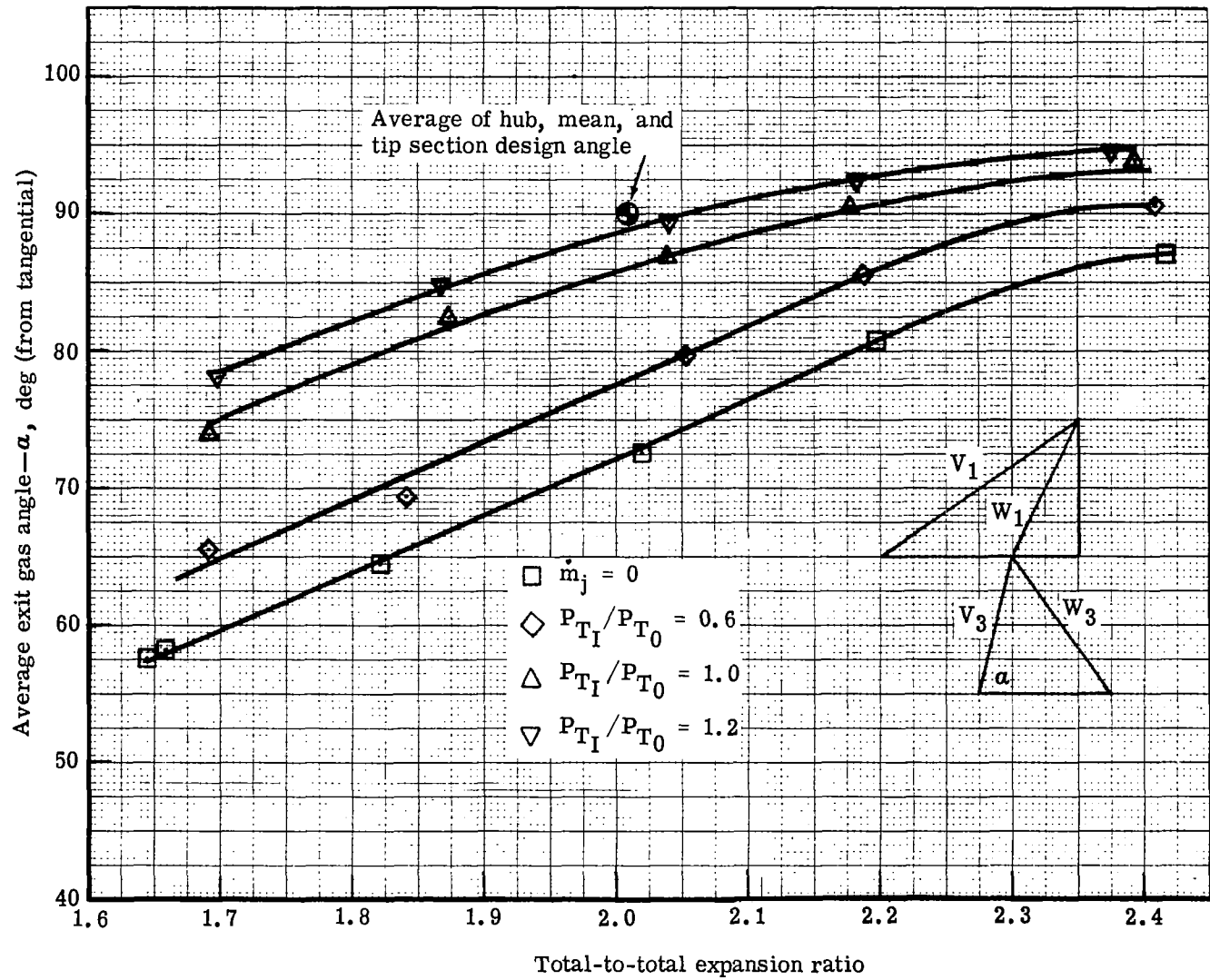


Figure 35. Variation of absolute exit angle with expansion ratio and cavity pressure ratio at design speed.

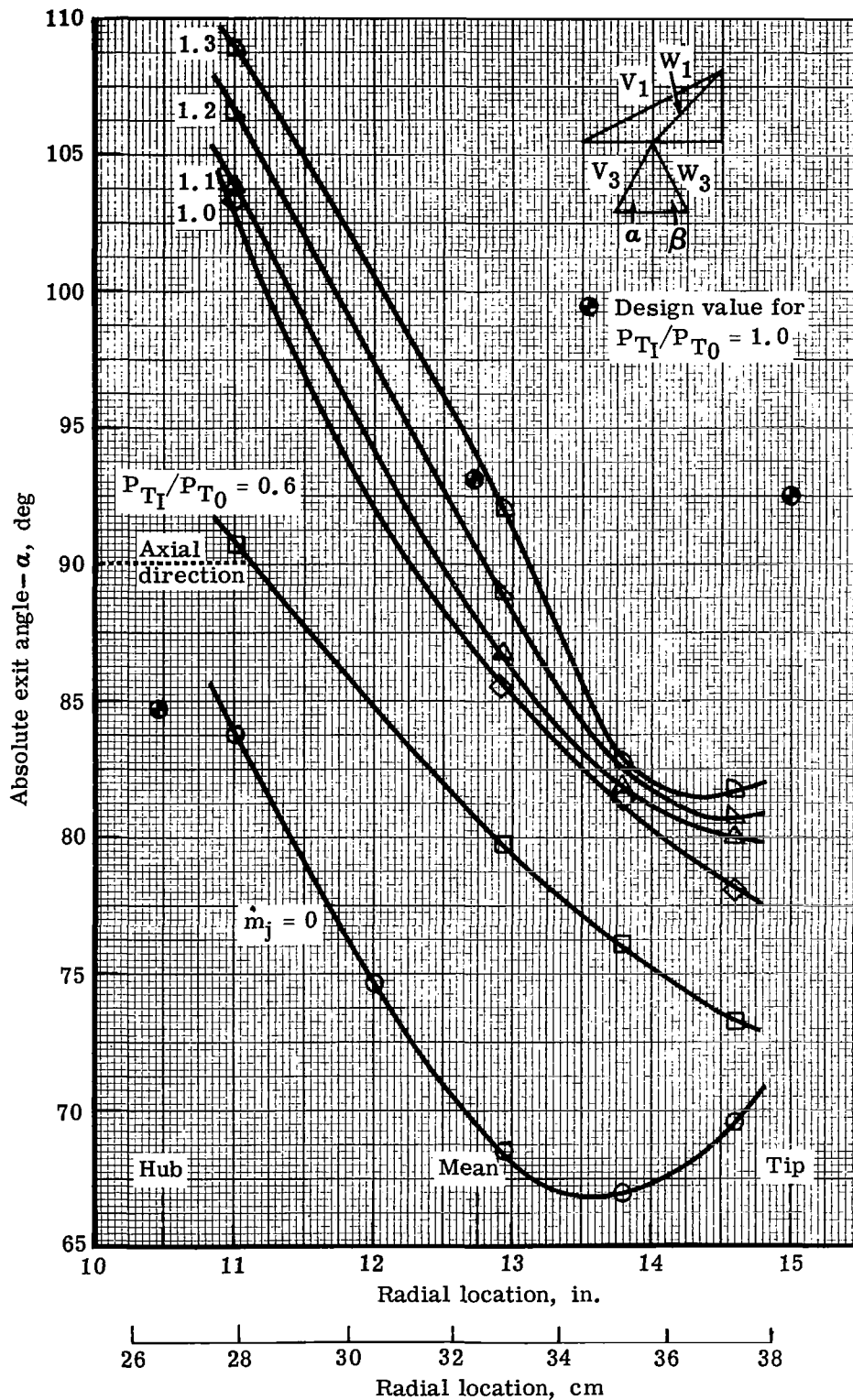


Figure 36. Radial variation of absolute exit angle with jet cavity pressure ratio at design speed and turbine expansion ratio.

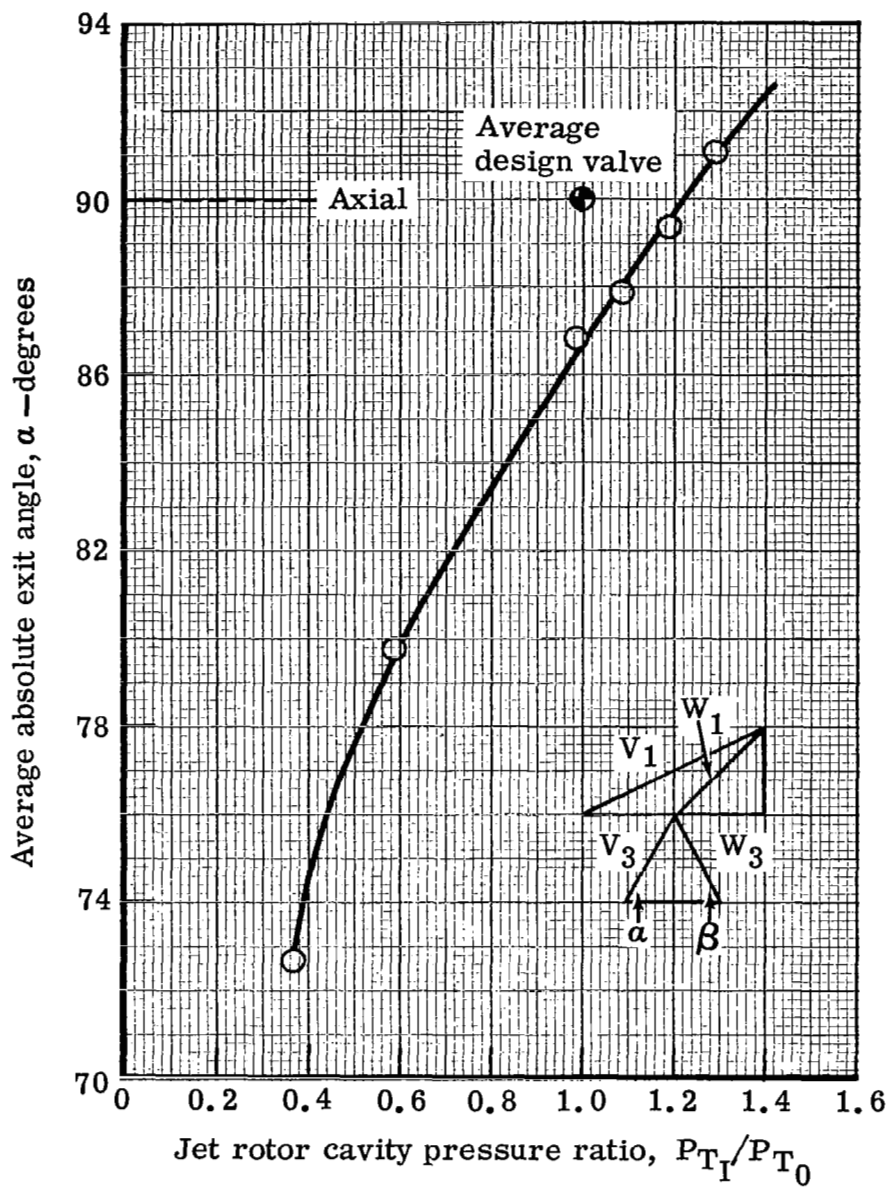


Figure 37. Variation of average absolute exit angle with cavity pressure ratio at design speed and expansion ratio.

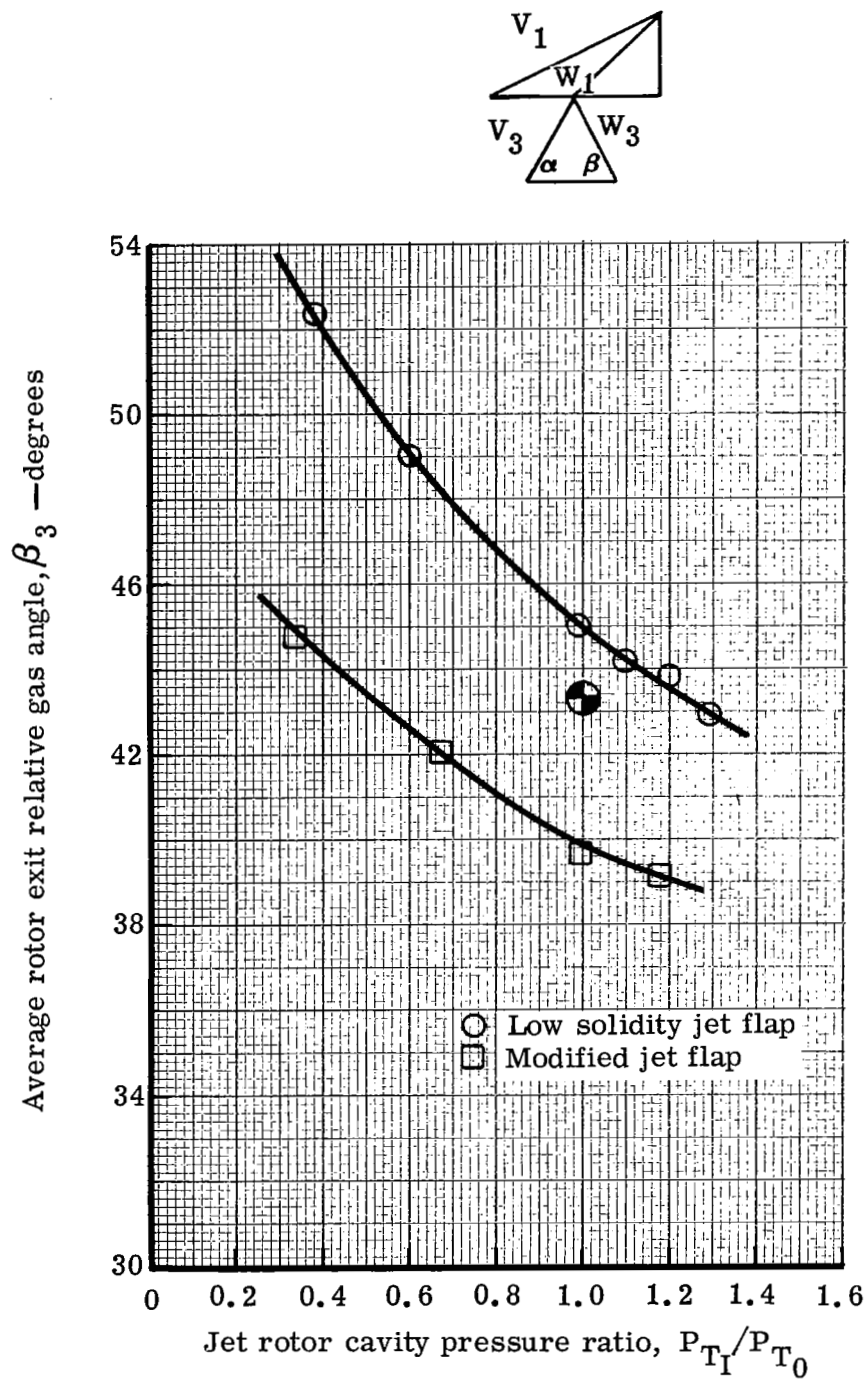


Figure 38. Variation of average rotor exit relative gas angle with rotor cavity pressure ratio for two jet flap blade designs at design speed and expansion ratio.

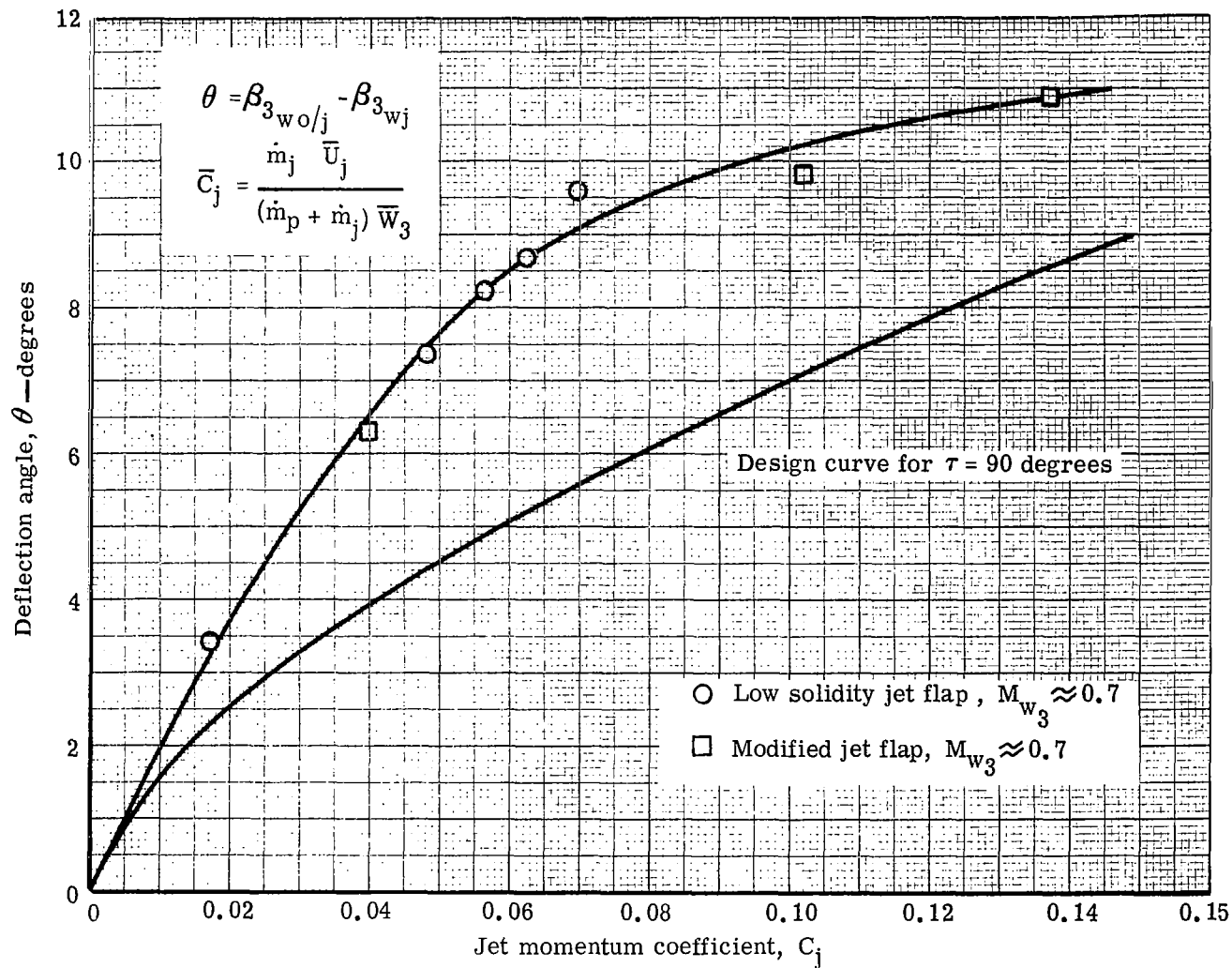


Figure 39. Comparison of jet deflection and momentum characteristics with design values for two jet flap blade designs with a relative exit Mach number of 0.7.

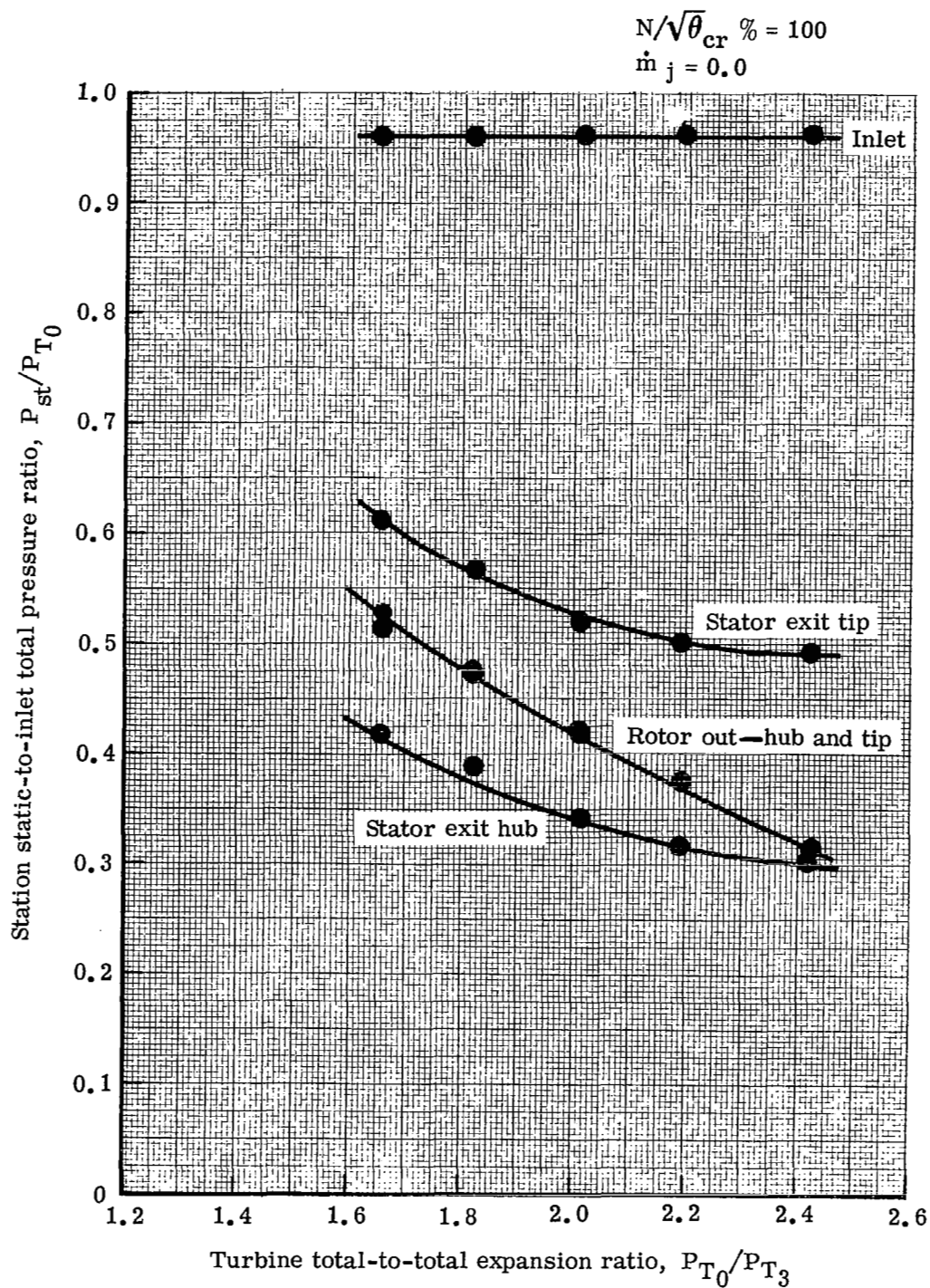


Figure 40. Variation of static pressure through turbine with expansion ratio at design speed and zero jet flow.

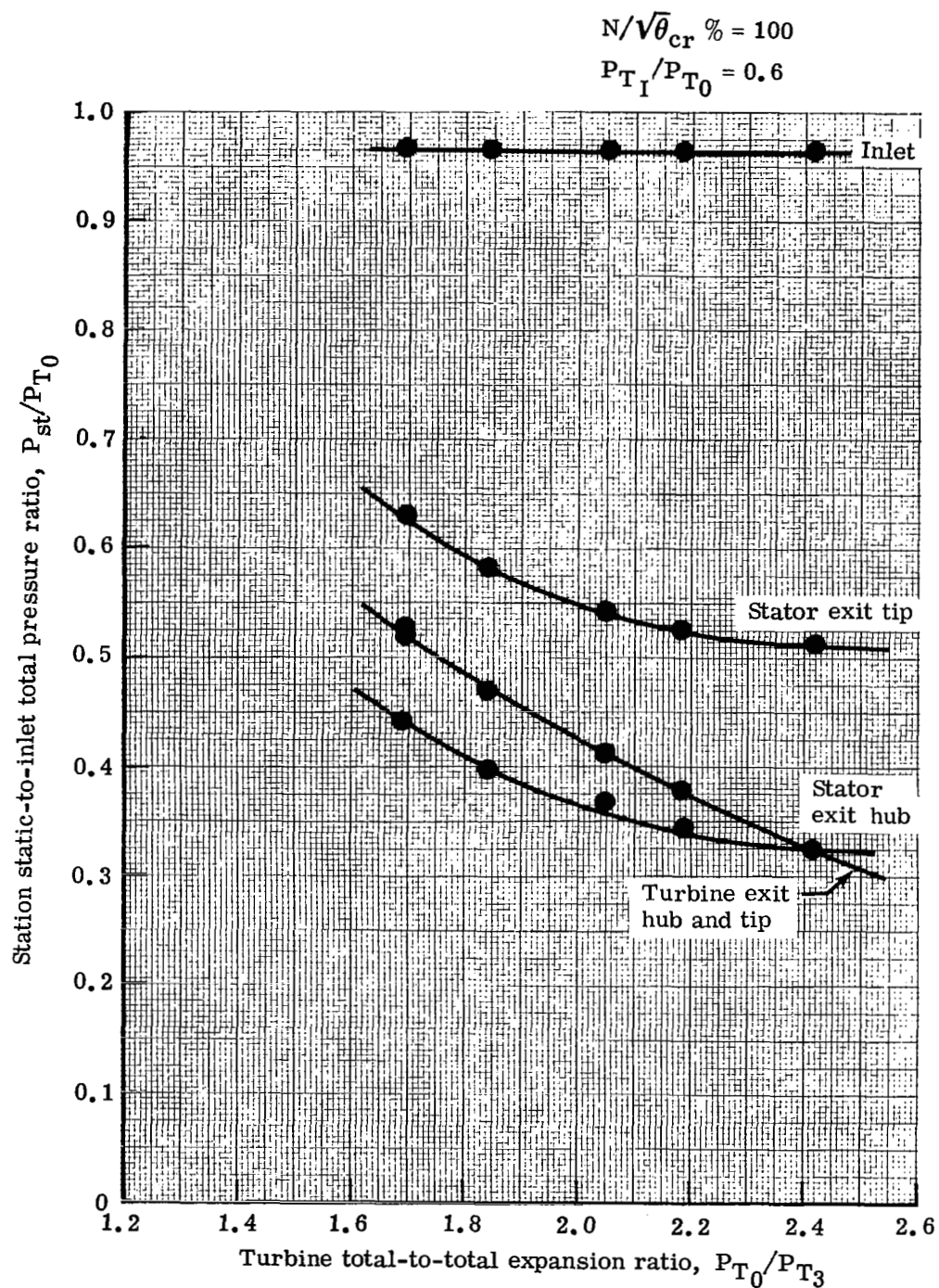


Figure 41. Variation of static pressure through turbine with expansion ratio at design speed and cavity pressure ratio equal to 0.6.

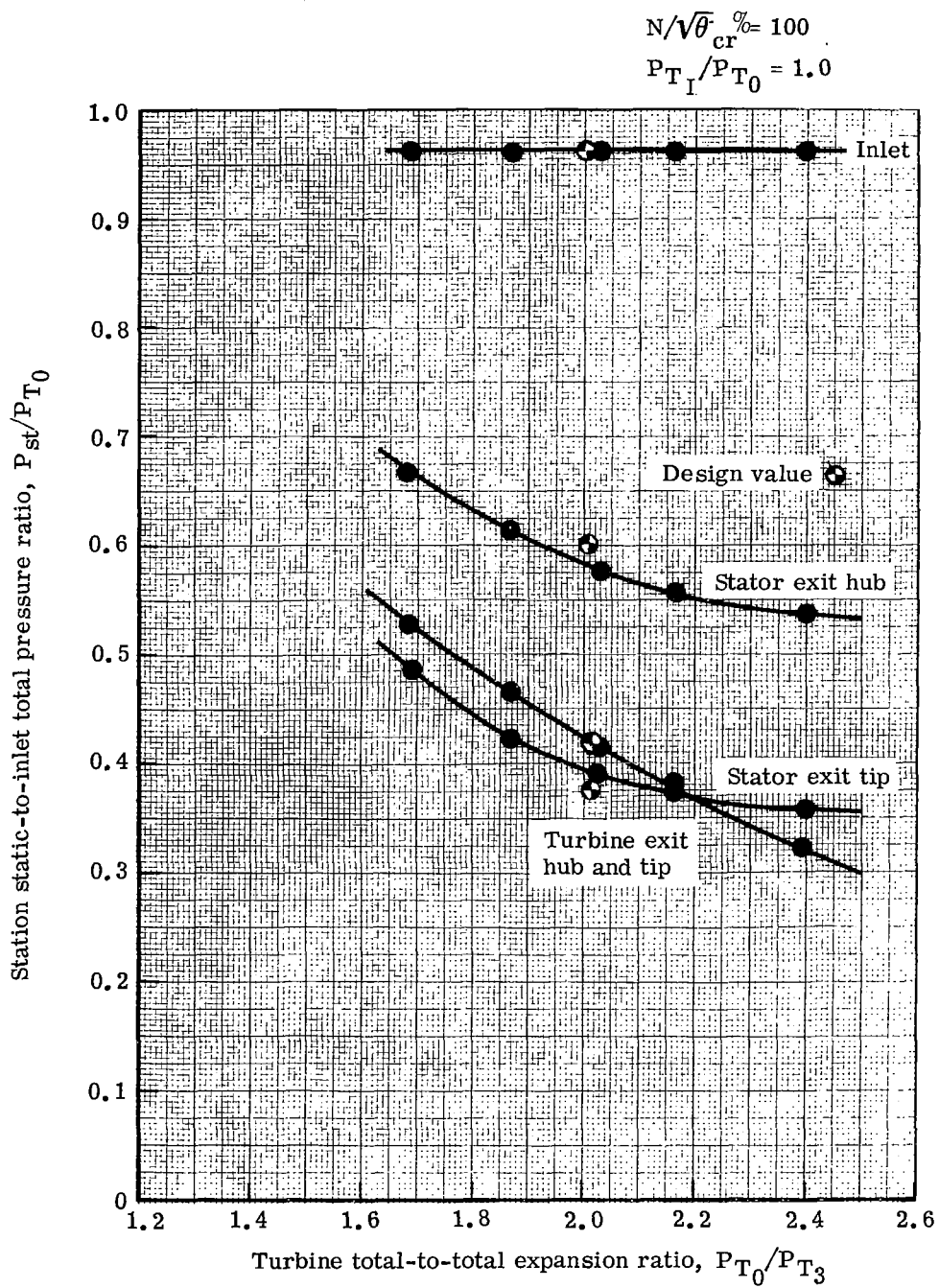


Figure 42. Variation of static pressure through turbine with expansion ratio at design speed and with cavity pressure ratio equal to 1.0.

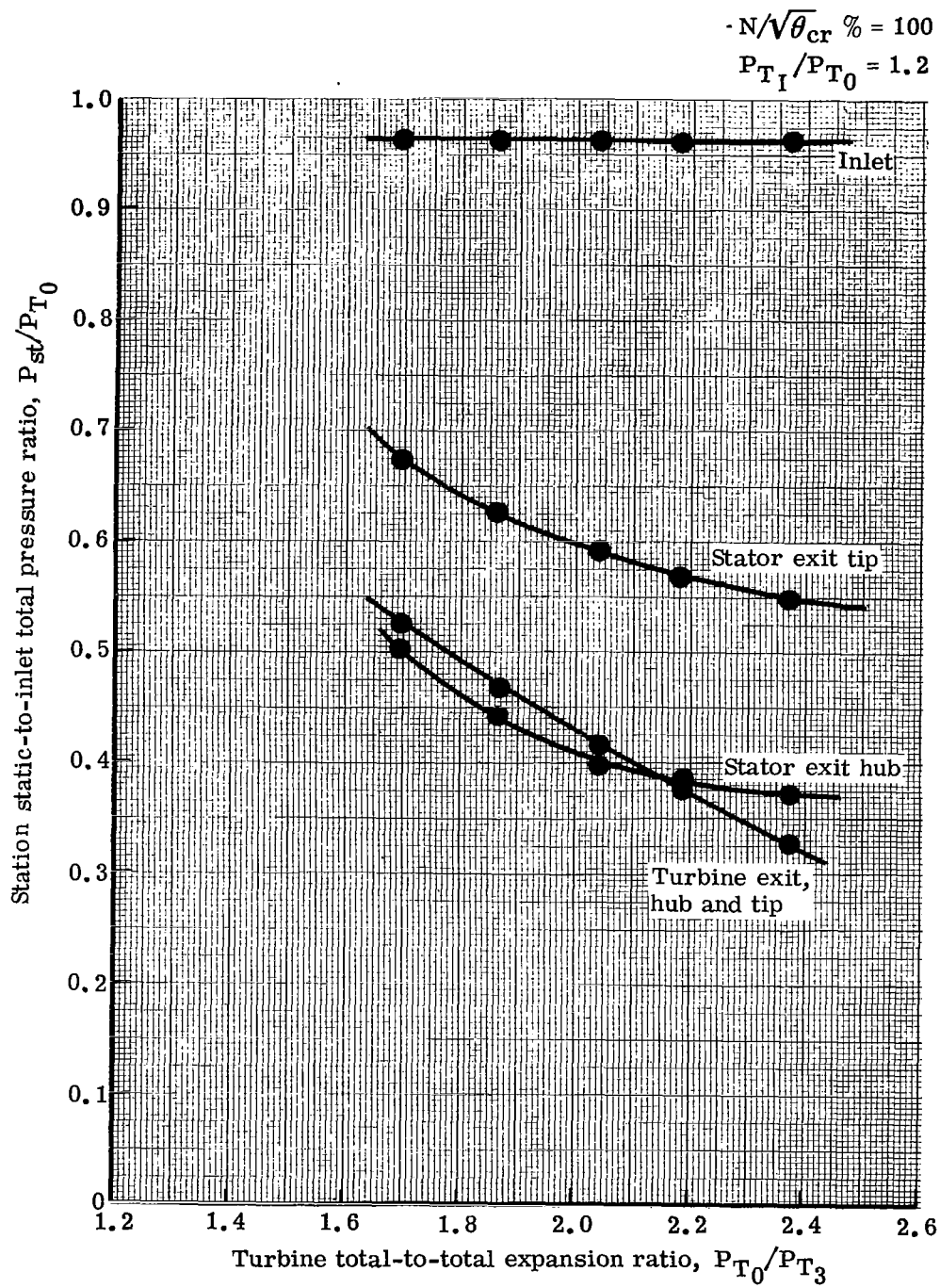


Figure 43. Variation of static pressure through turbine with expansion ratio at design speed and with cavity pressure ratio equal to 1.2.

$$\frac{N}{\sqrt{\theta}}_{cr} = 100\%$$

Design = Re_{TT}

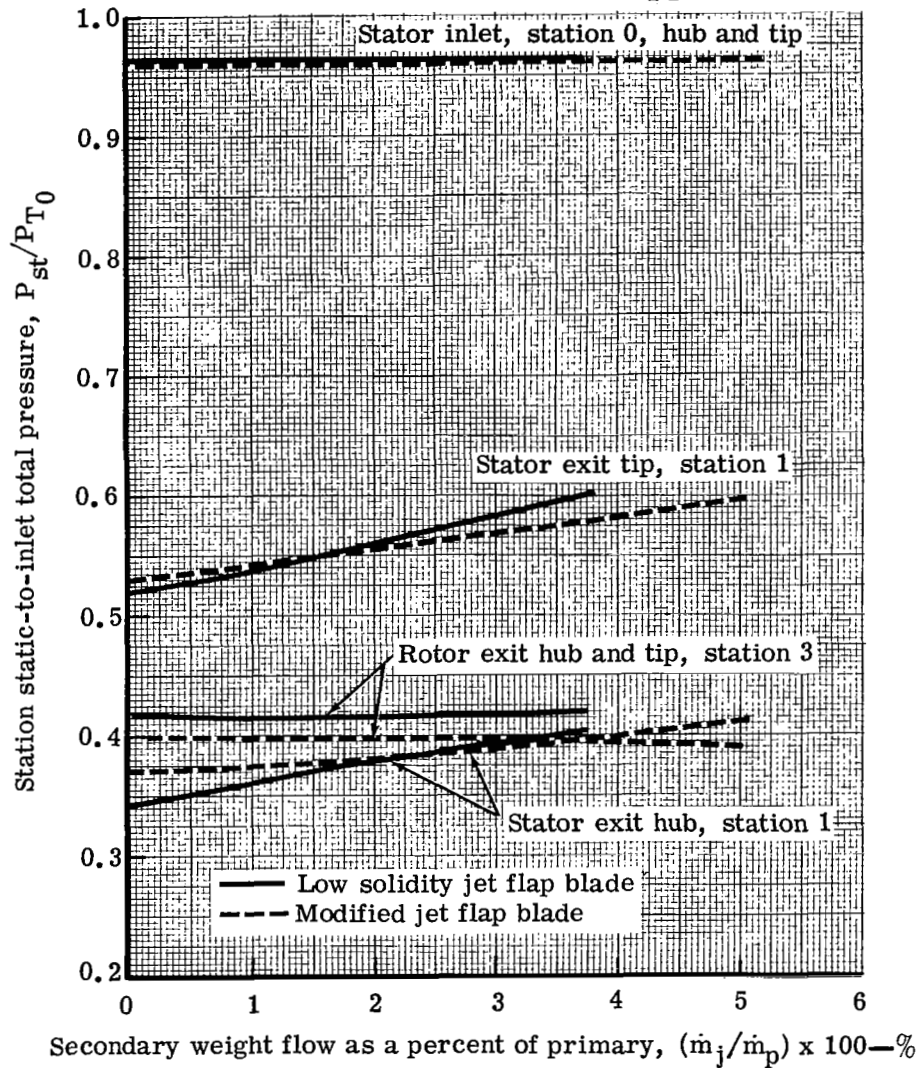


Figure 44. Comparison of static pressure variation through turbine for two jet flap blade designs.

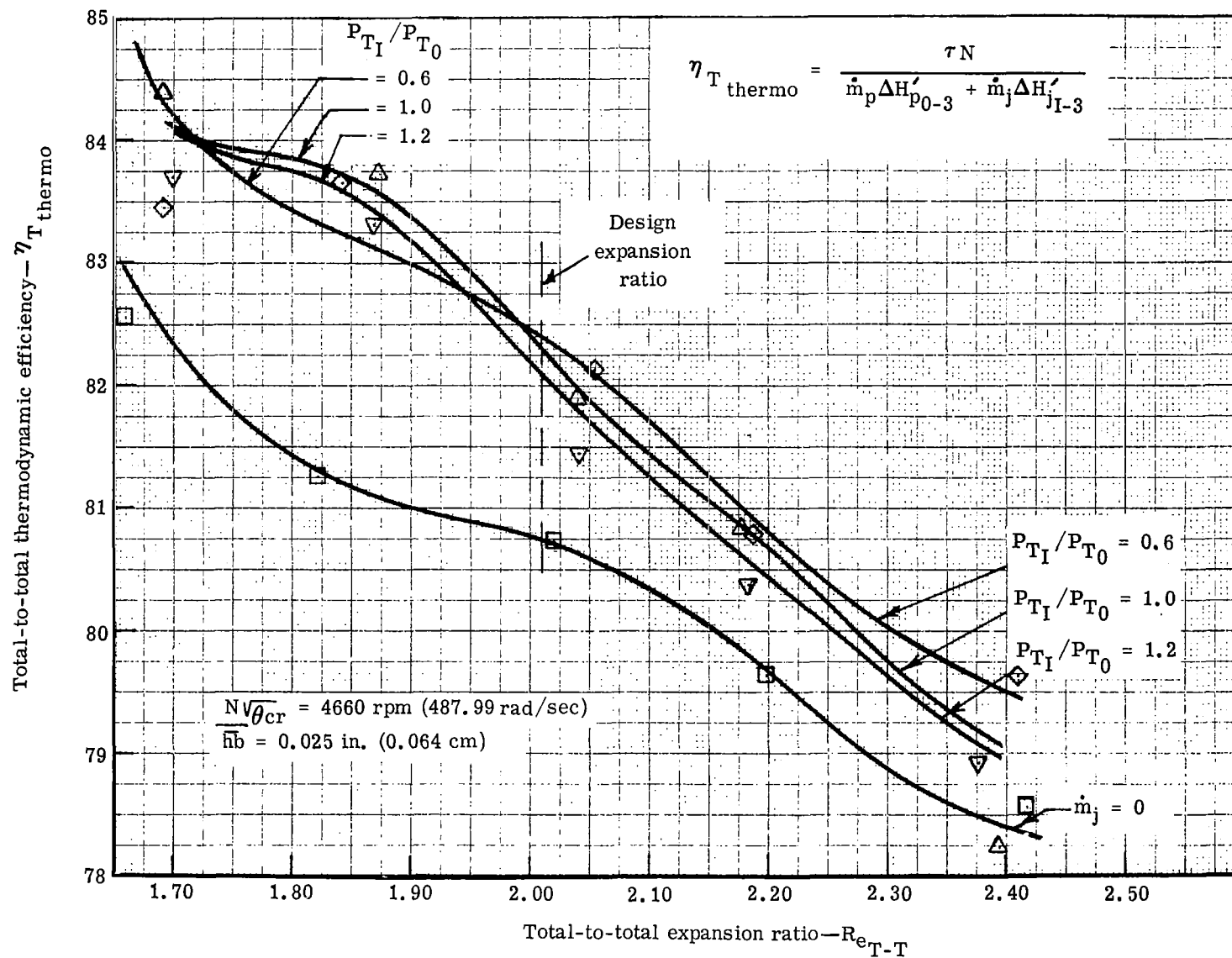


Figure 45. Variation of thermodynamic efficiency with expansion ratio and cavity pressure ratio at design speed.

$$N/\sqrt{\theta_{cr}} = 4660 \text{ rpm (487.99 rad/sec)}$$

$$hb = 0.025 \text{ in. (0.064 cm)}$$

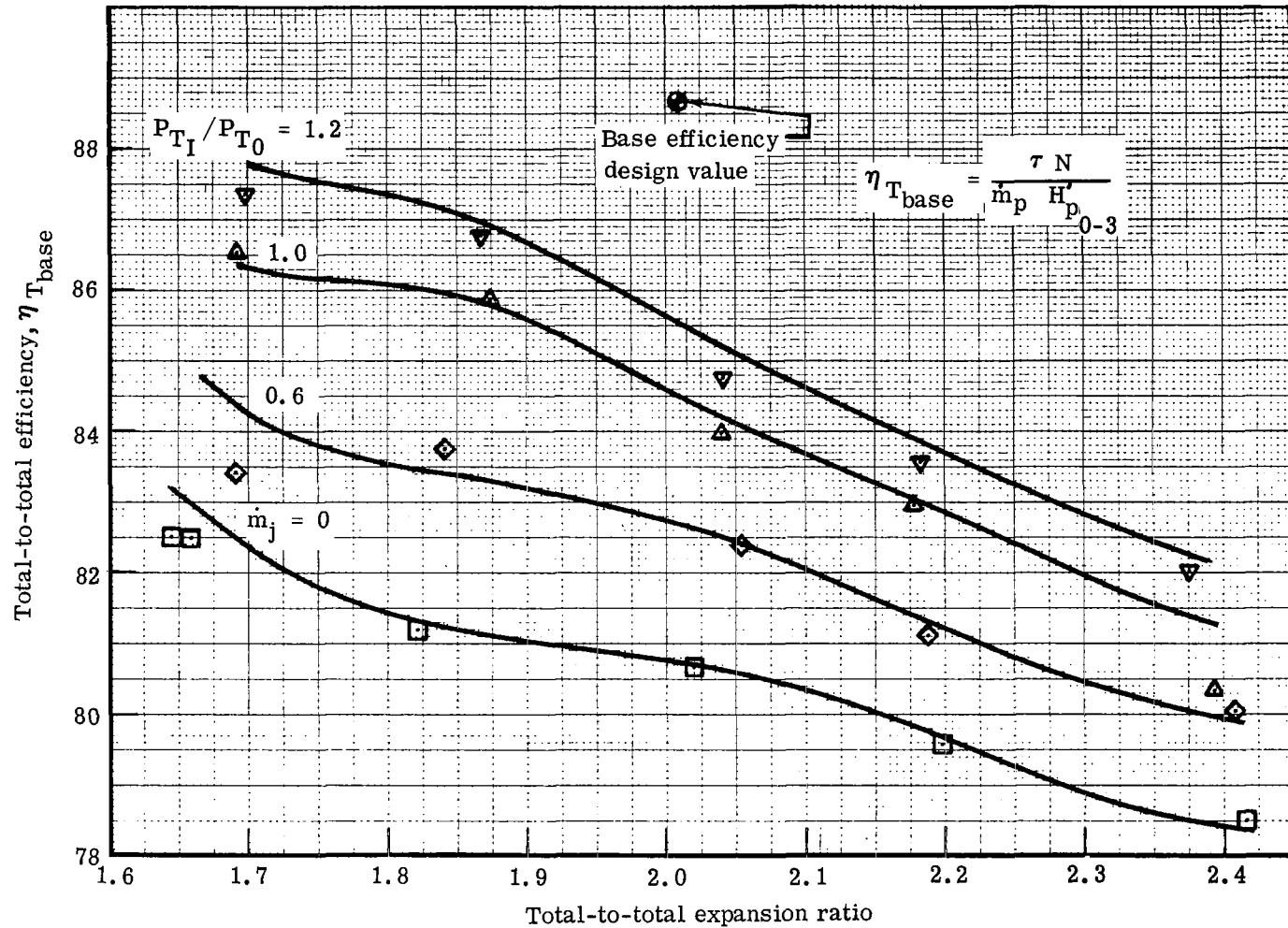


Figure 46. Variation of base efficiency with expansion ratio and cavity pressure ratio at design speed.

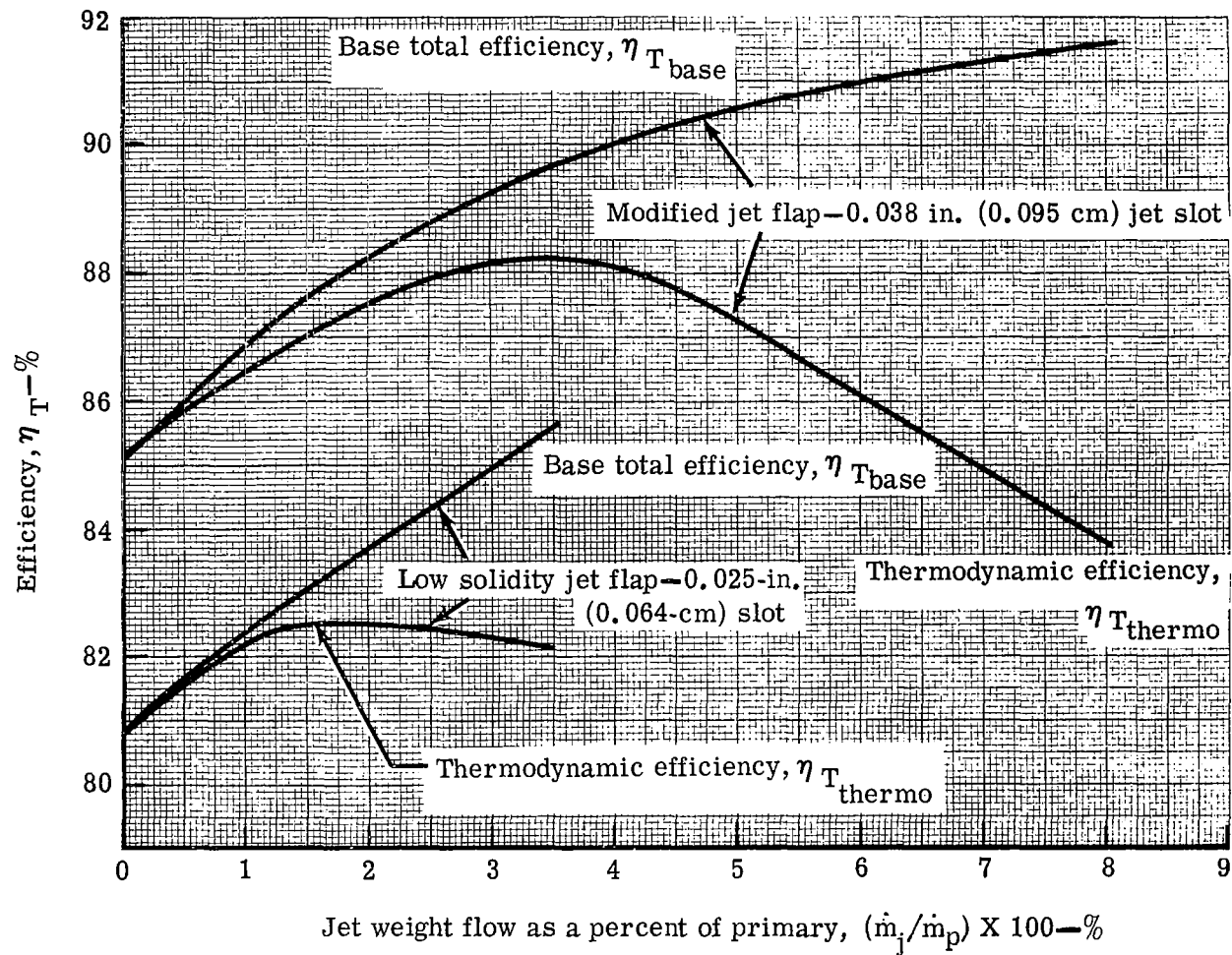


Figure 47. Variation of turbine efficiency with percent jet flow rate for two jet flap designs at design speed and expansion ratio.

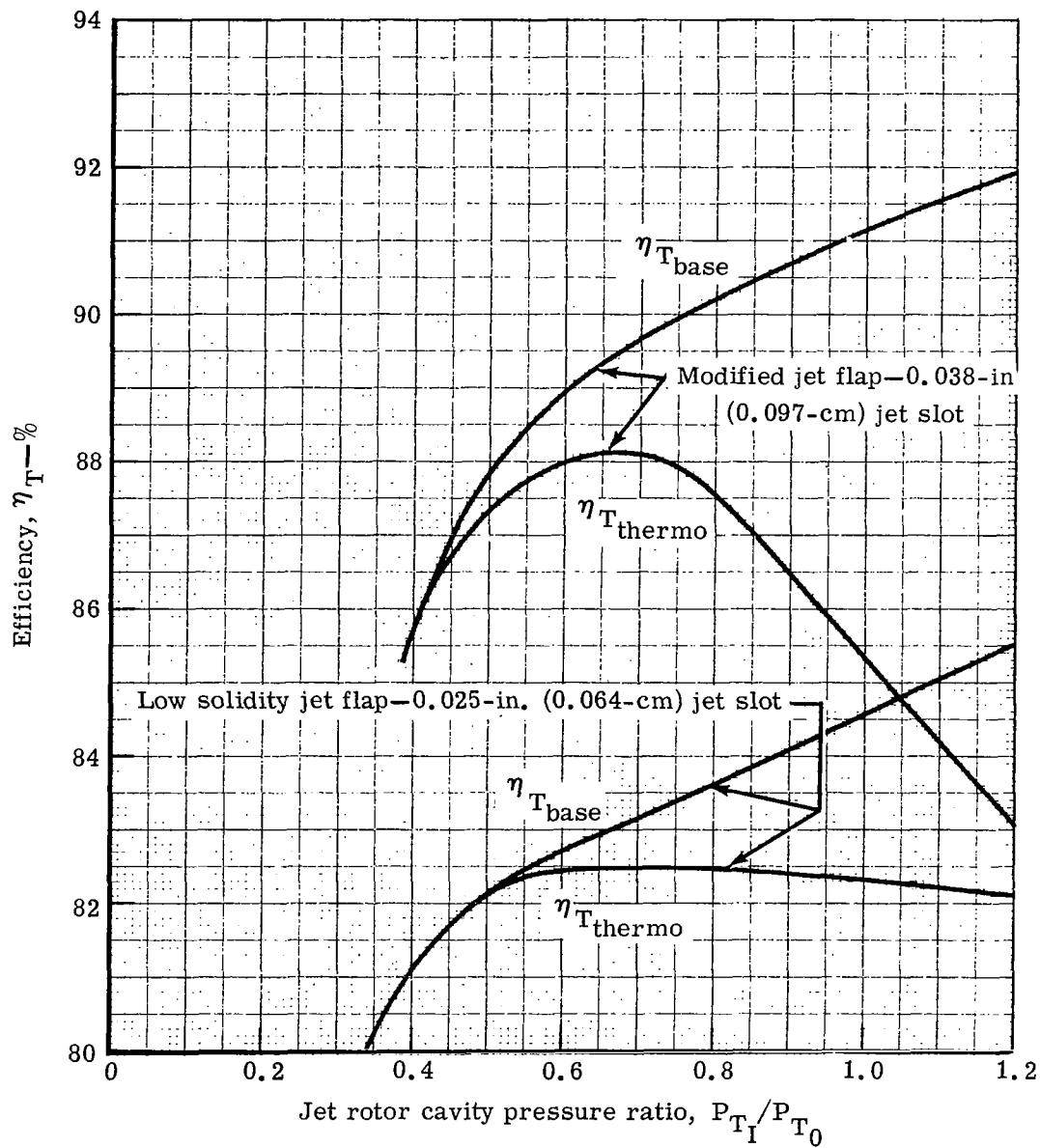


Figure 48. Variation of turbine efficiency with cavity pressure ratio for two jet flap designs at design speed and expansion ratio.

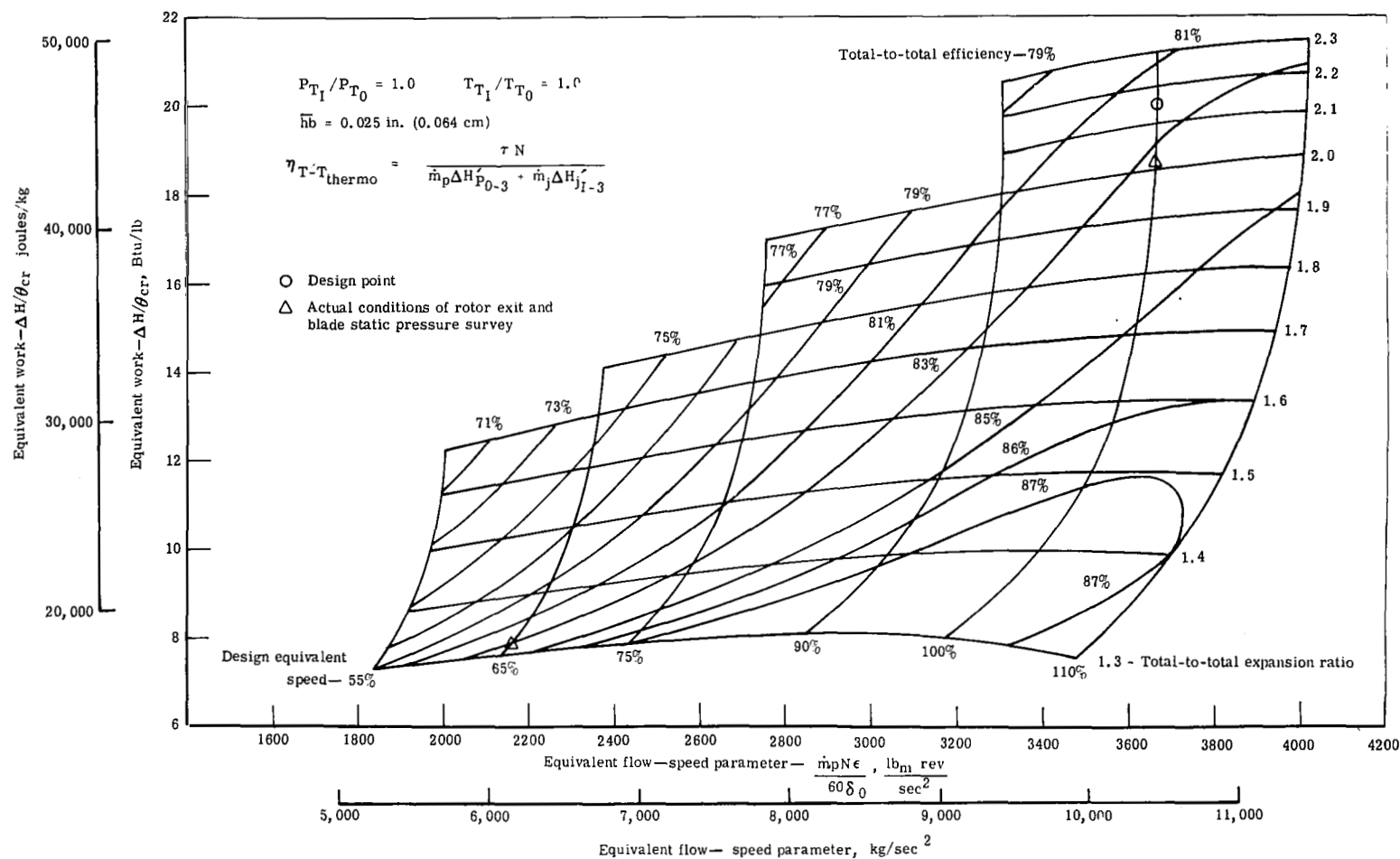


Figure 49. Overall performance map for low solidity jet flap blade with 0.025 in. (0.064 cm) jet slot and $P_{T1}/P_{T0} = 1.0$.

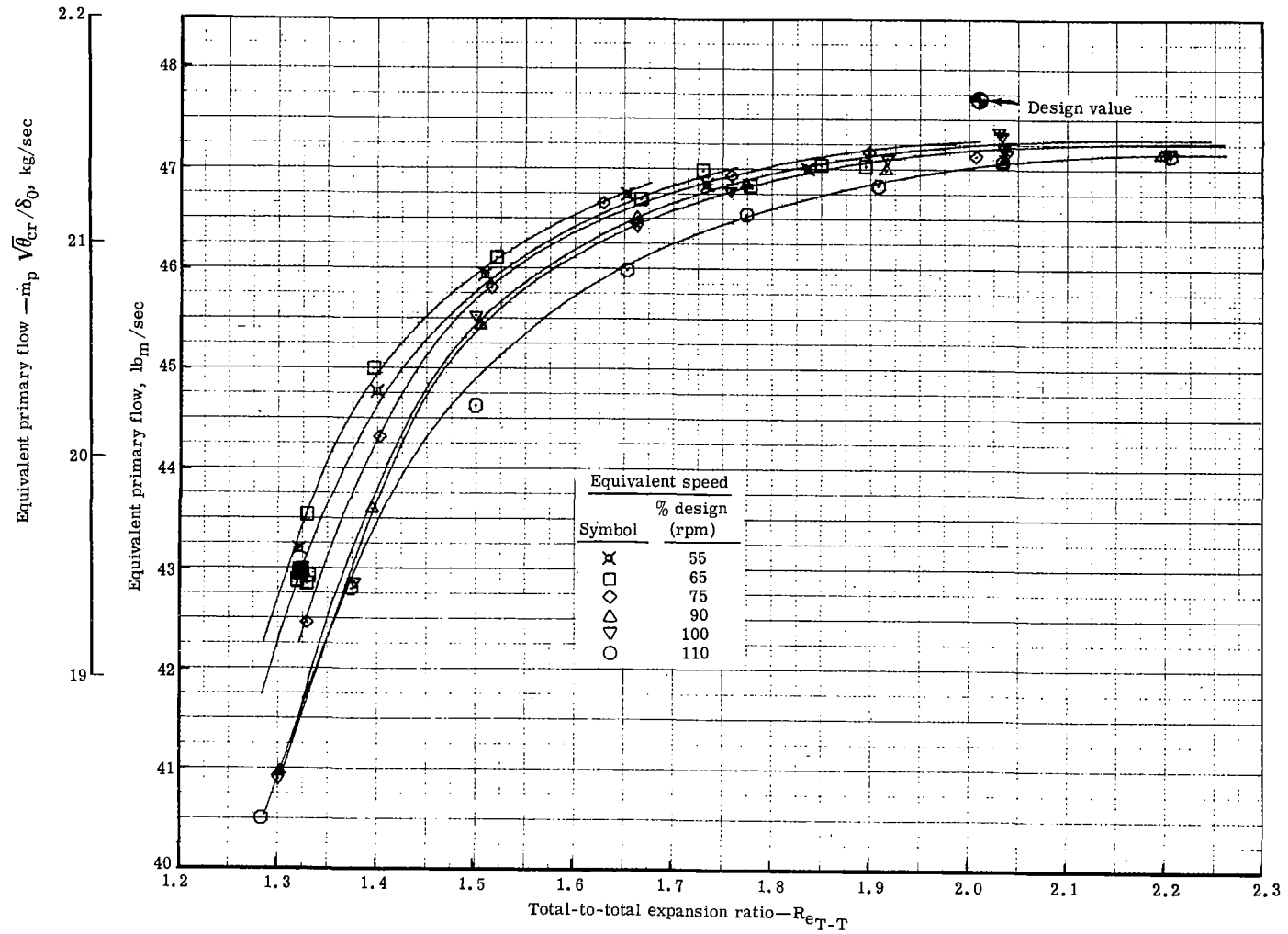


Figure 50. Variation of equivalent primary flow with expansion ratio and speed with $P_{T1}/P_{T0} = 1.0$ for low solidity jet flap turbine.

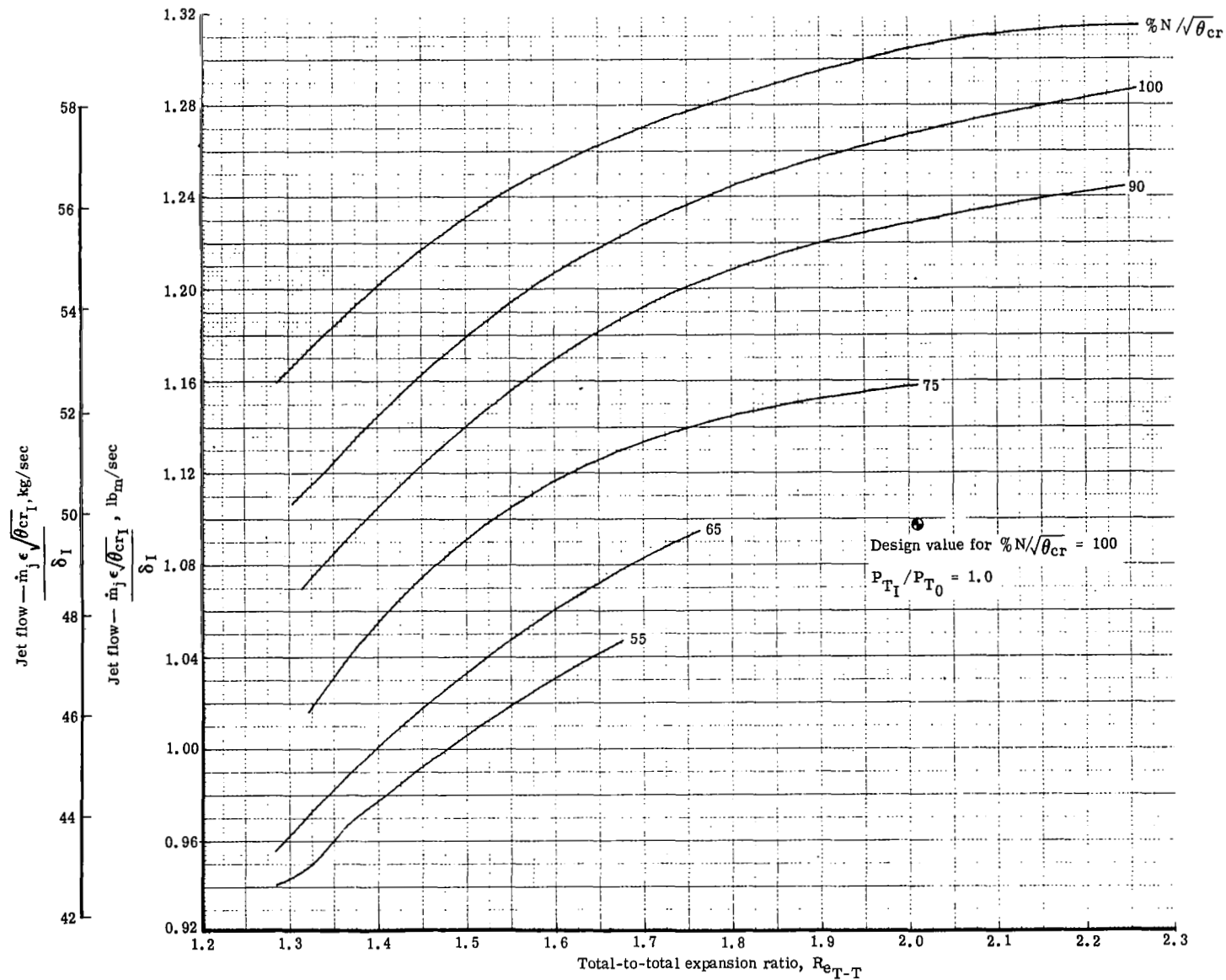


Figure 51. Variation of jet flow with turbine expansion ratio and speed with cavity pressure ratio equal to unity.

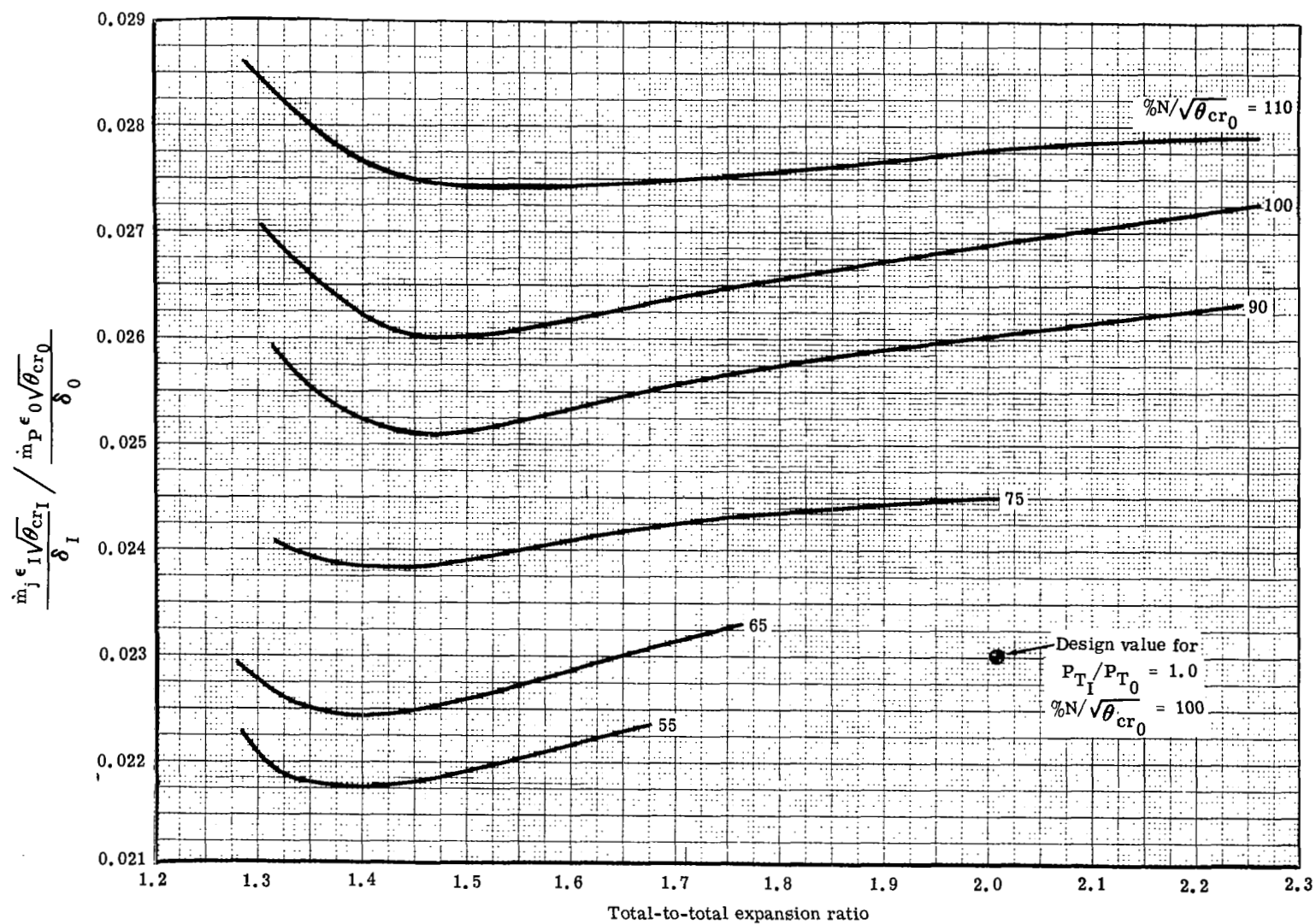


Figure 52. Variation of percent equivalent jet flow rate with expansion ratio and speed for low solidity jet flap with $P_{T1}/P_{T0} = 1.0$, $h\bar{b} = 0.025$ in. (0.064 cm).

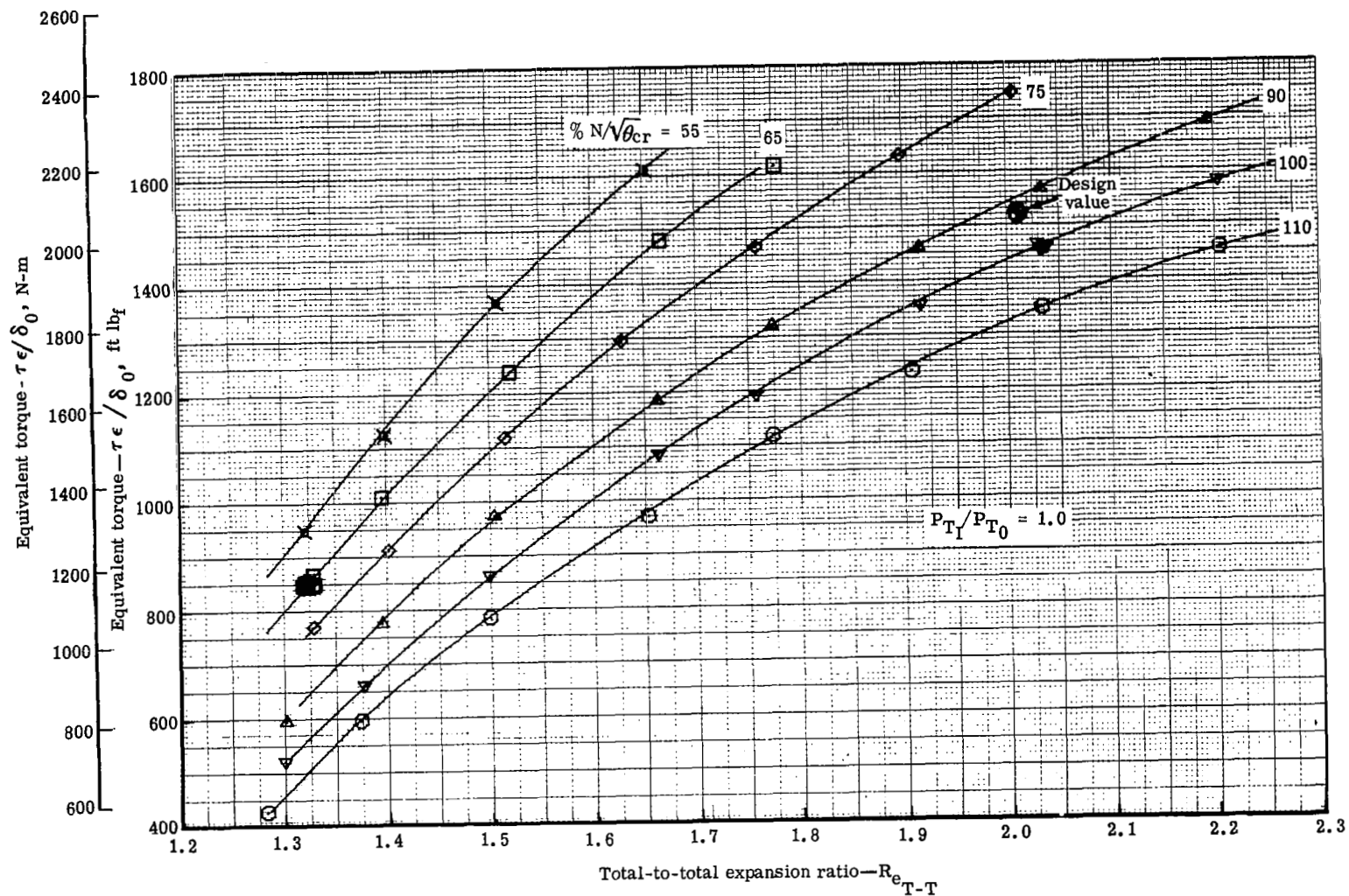


Figure 53. Variation of equivalent torque with speed and expansion ratio for low solidity jet flap with $P_{T_I}/P_{T_0} = 1.0$, $hb = 0.025$ in. (0.064 cm).

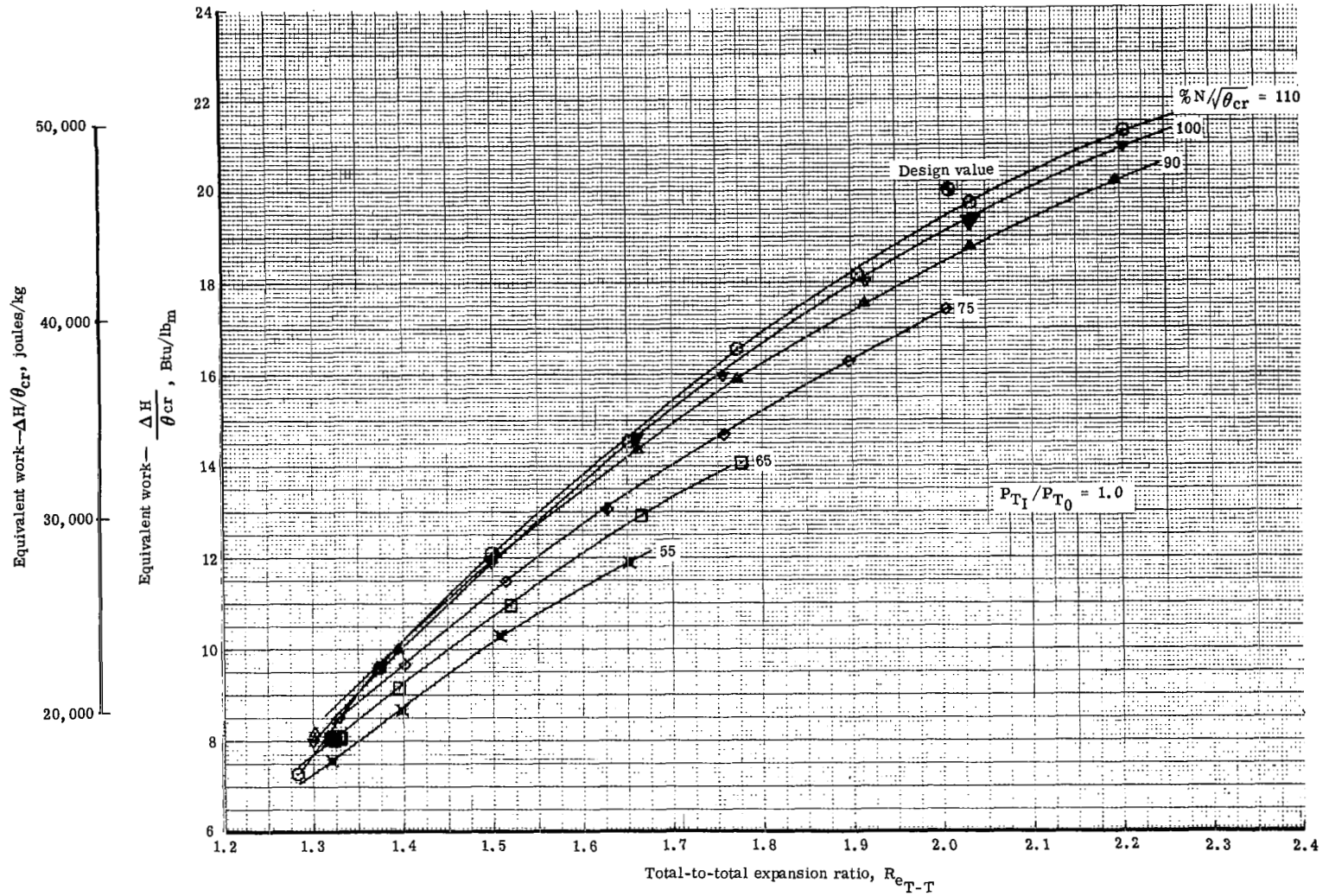


Figure 54. Variation of equivalent work with speed and expansion ratio for low solidity jet flap with $P_{T1}/P_{T0} = 1.0$, $\bar{h}b = 0.025$ in. (0.064 cm).

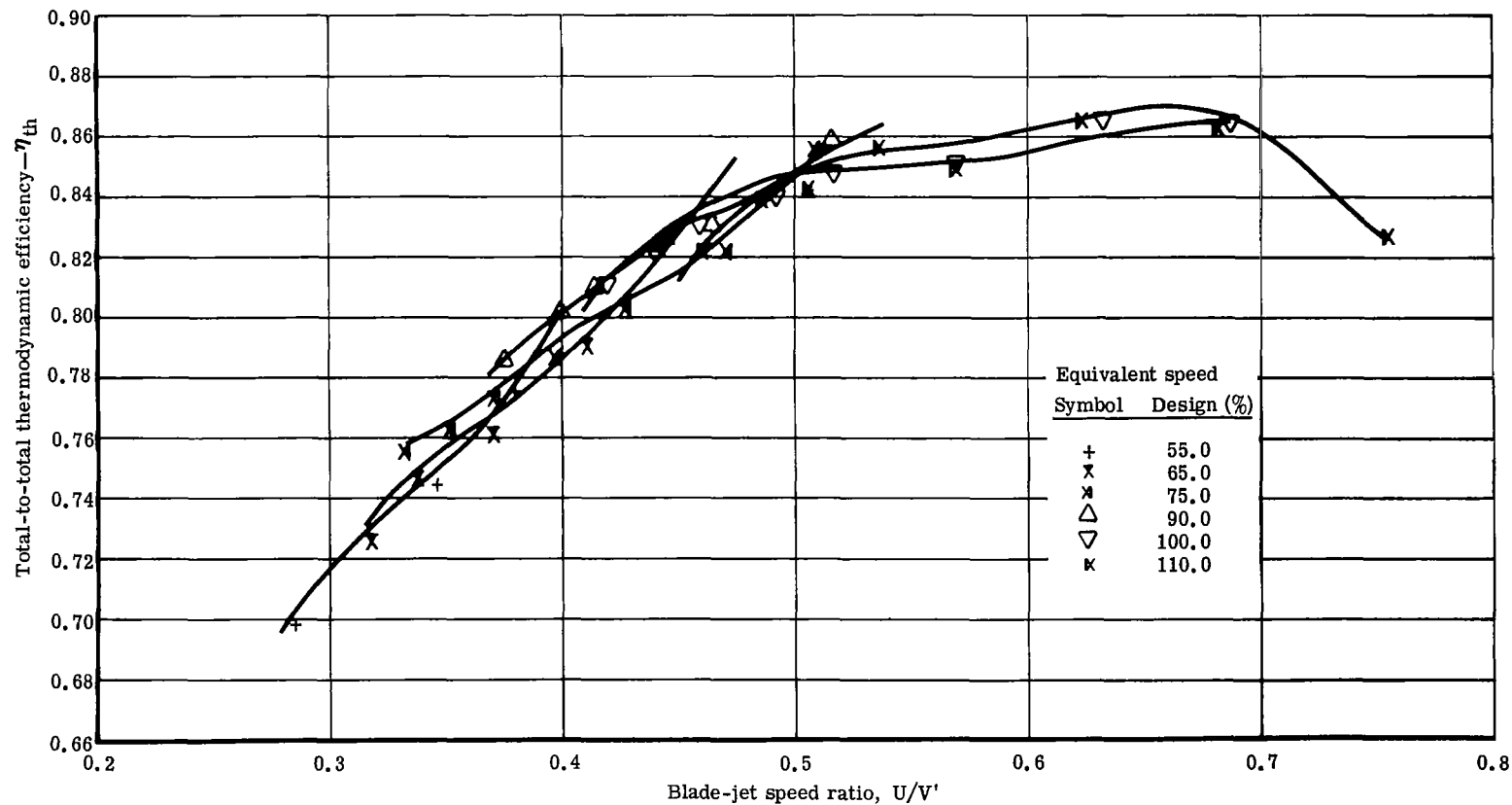


Figure 55. Variation of thermodynamic efficiency with jet speed ratio for low solidity jet flap turbine with $P_{T1}/P_{T0} = 1.0$, $\bar{h}\bar{b} = 0.025$ in. (0.064 cm).

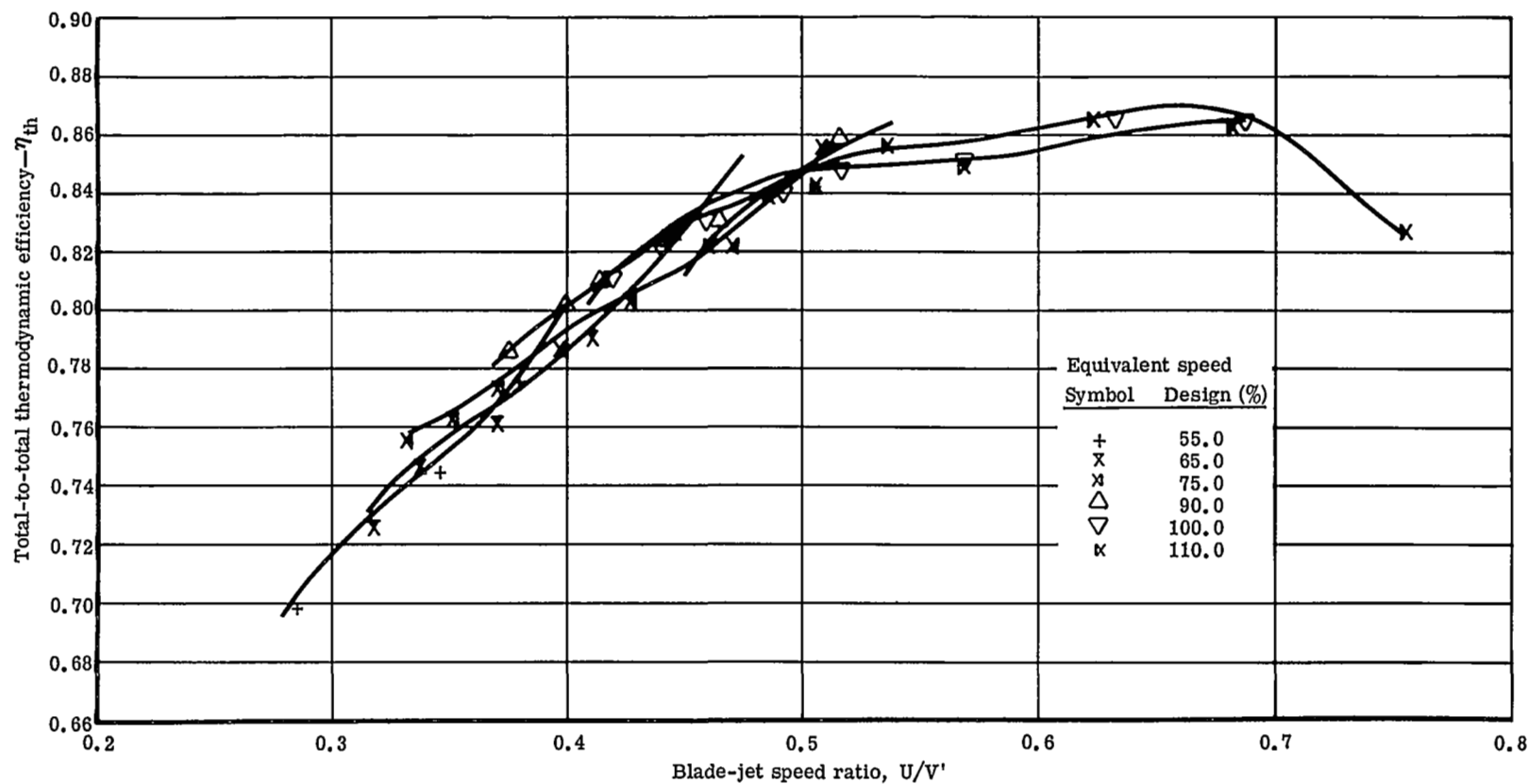


Figure 55. Variation of thermodynamic efficiency with jet speed ratio for low solidity jet flap turbine with $P_{T1}/P_{T0} = 1.0$, $\bar{h}\bar{b} = 0.025$ in. (0.064 cm).

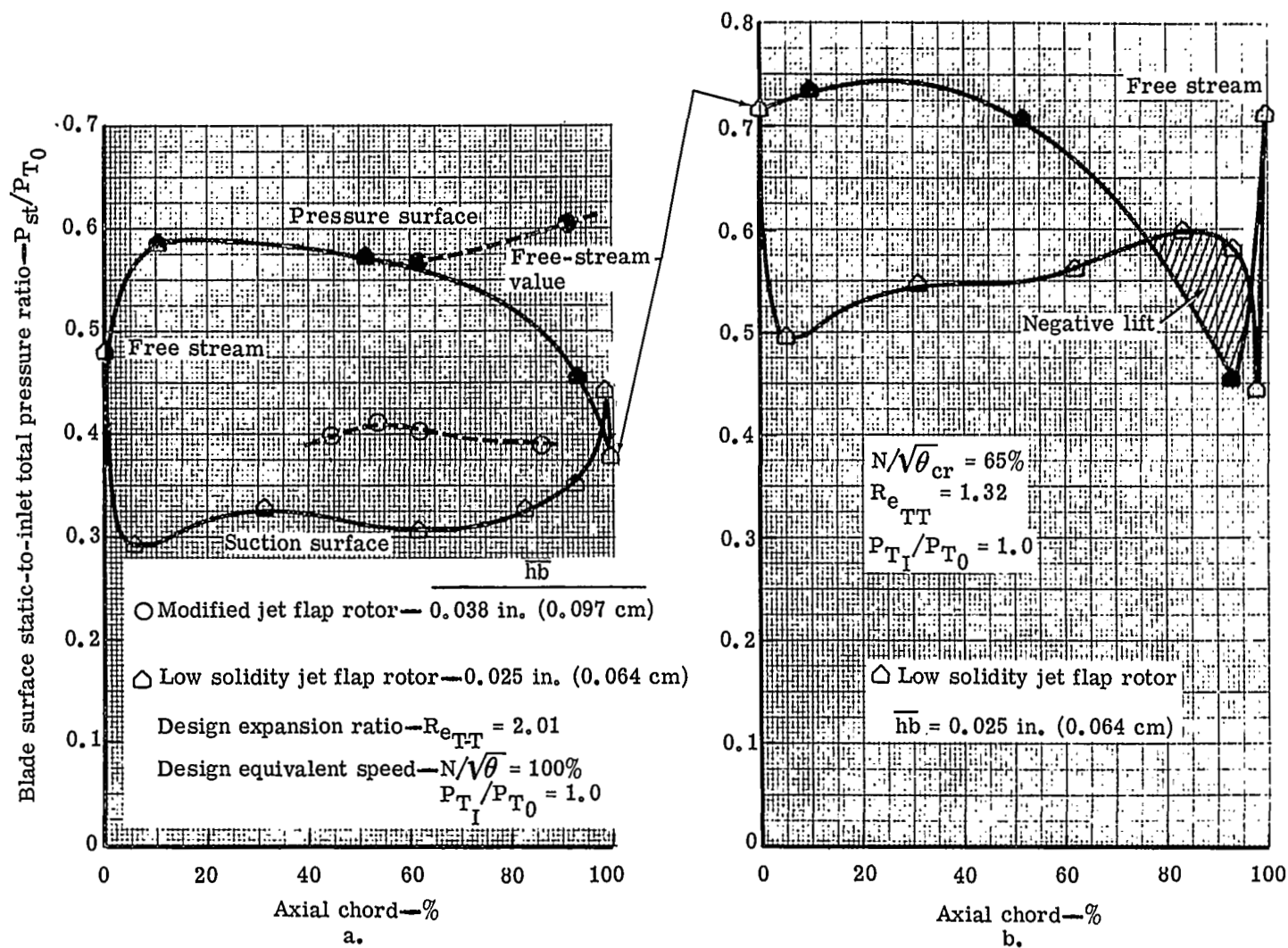


Figure 56. Mean section static pressure distributions on low solidity and modified jet flap blades.

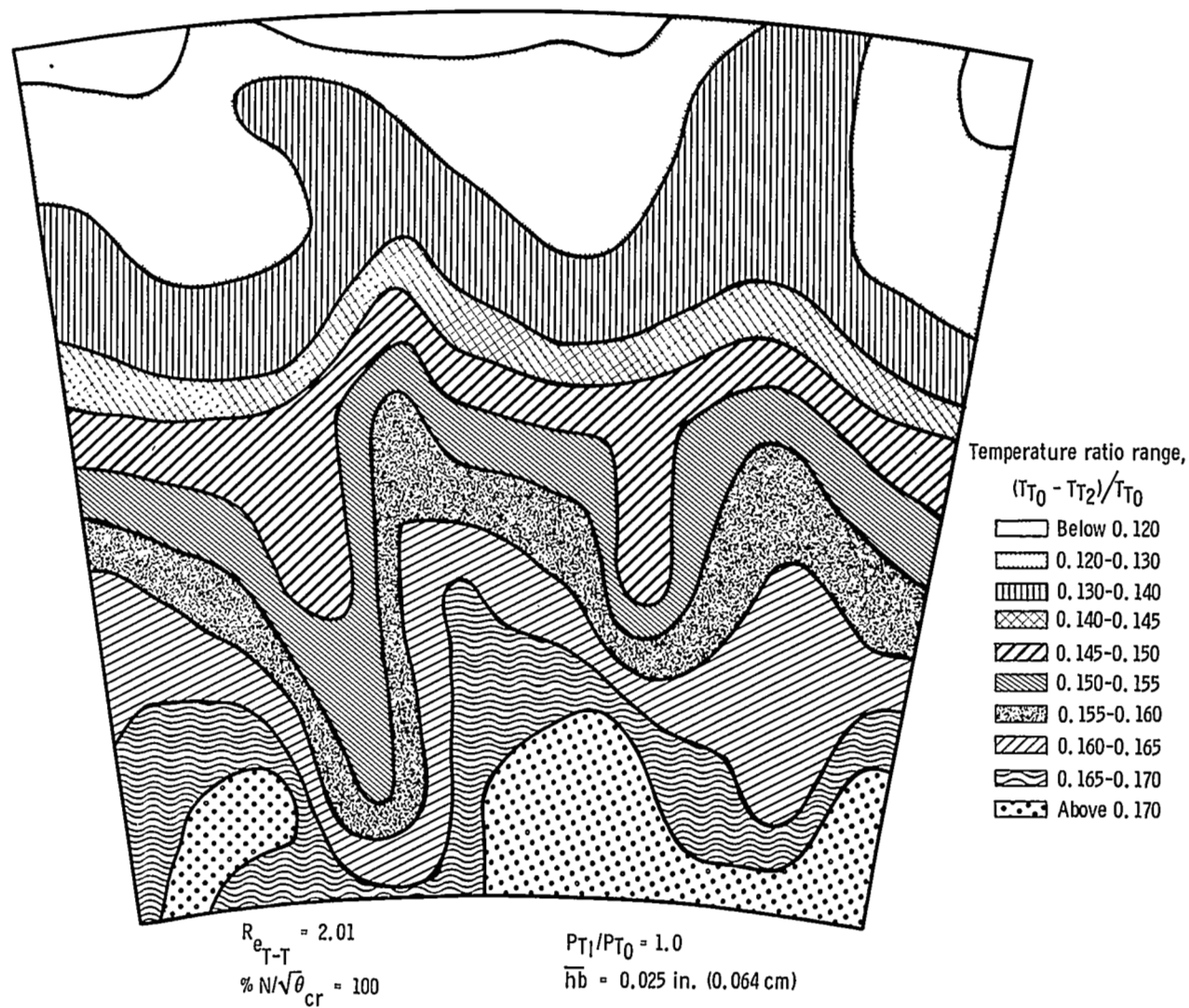


Figure 57. Turbine stage temperature ratio contours for low solidity jet flap blade at design speed and expansion ratio.

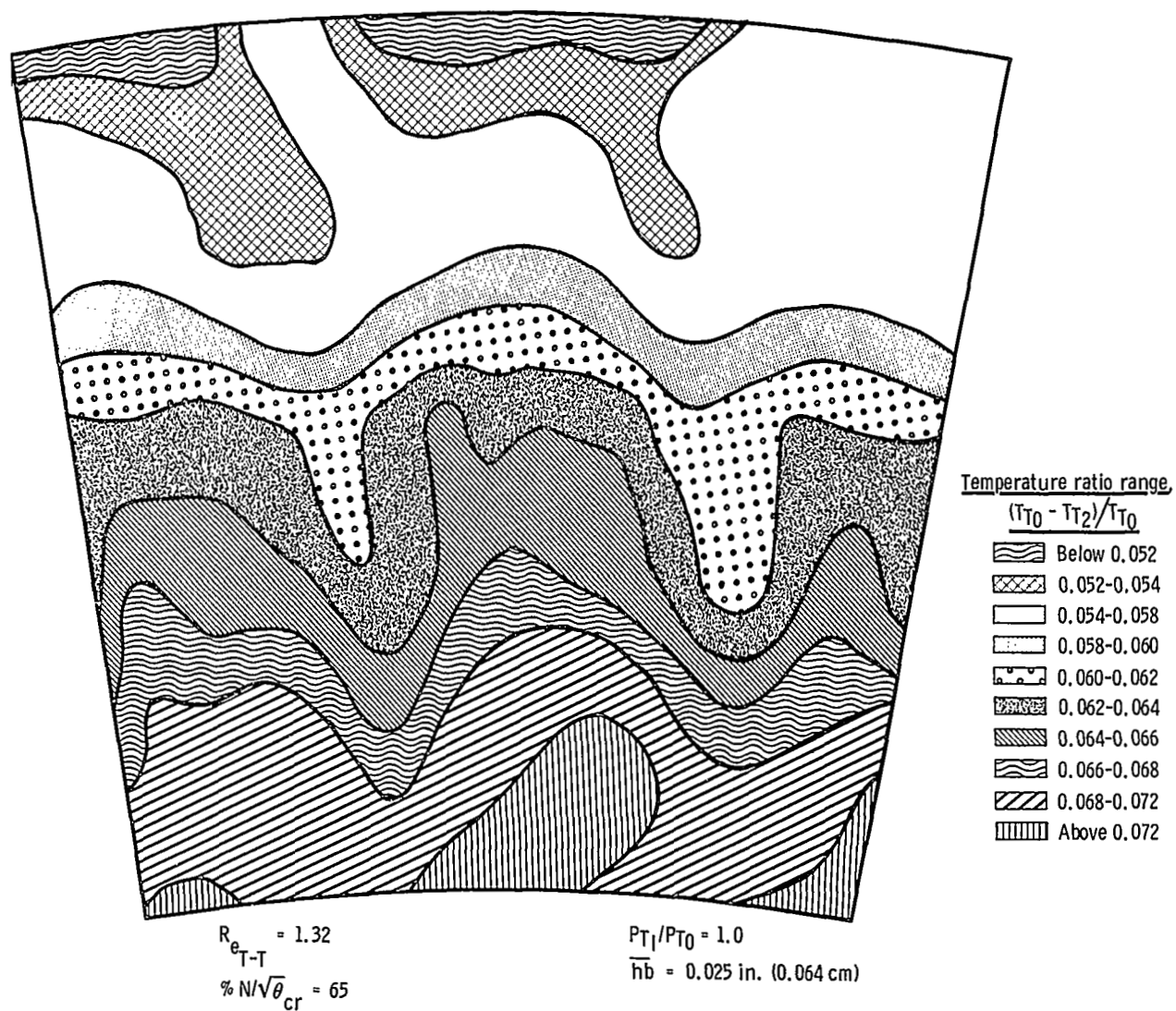


Figure 58. Turbine stage temperature ratio contours for low solidity jet flap turbine at $R_{e_{T-T}} = 1.32$, $N/\sqrt{\theta}_{cr} = 65\%$.

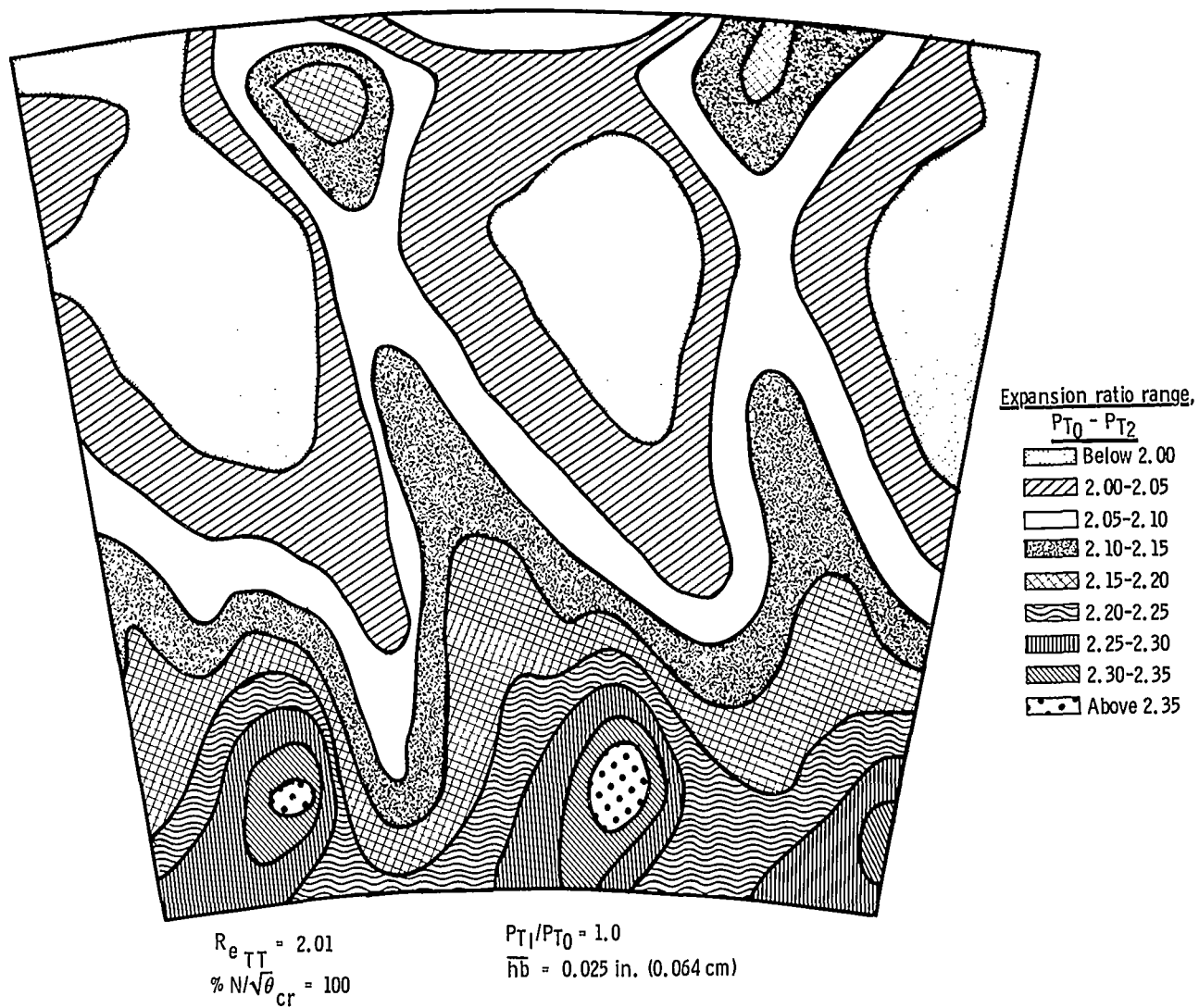


Figure 59. Turbine stage total pressure ratio contours for low solidity jet flap blade at design speed and expansion ratio.

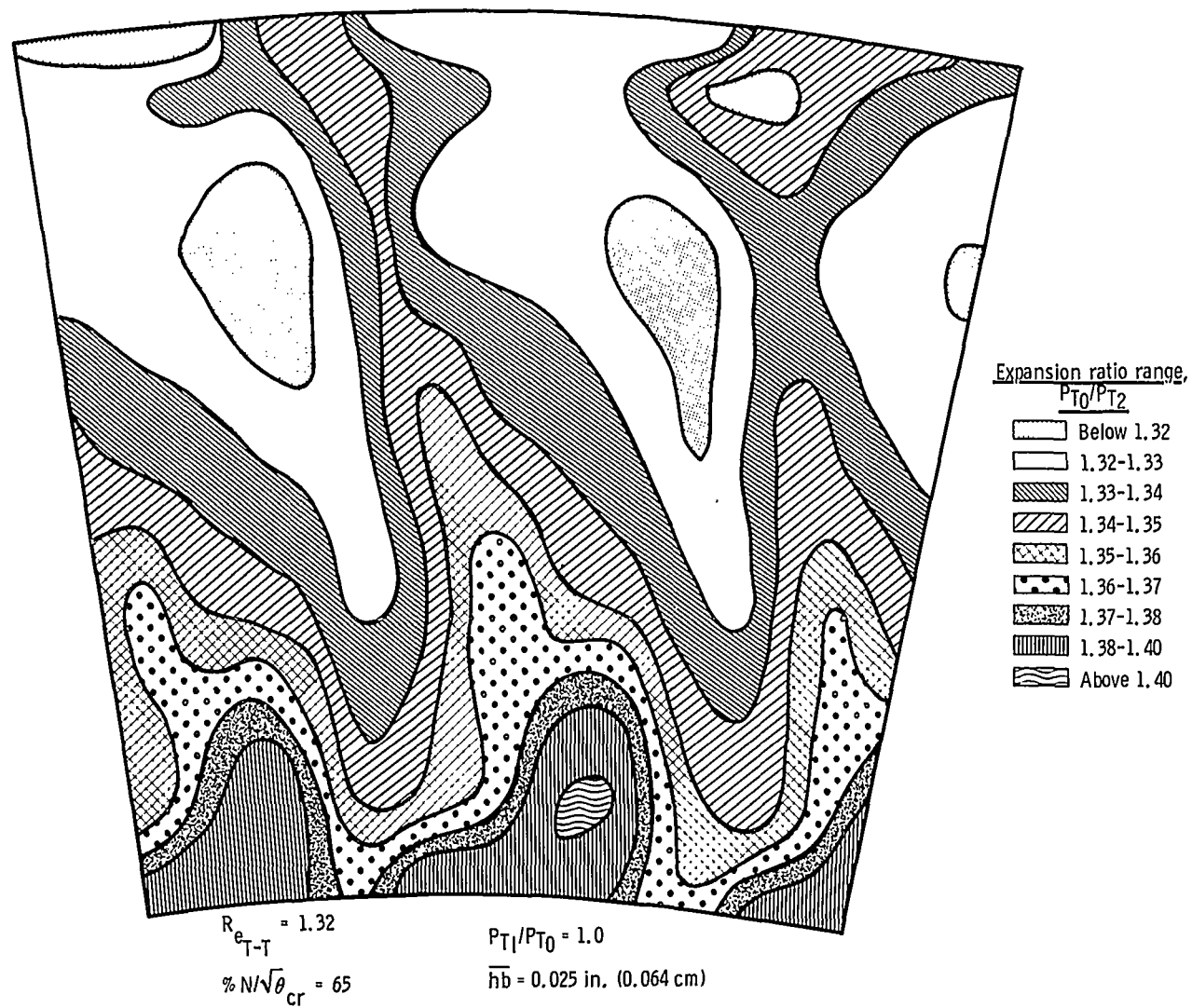


Figure 60. Turbine stage total pressure ratio contours for low solidity jet flap blade at $R_{e_{T-T}} = 1.32$, $N/\sqrt{\theta}_{cr} = 65\%$.

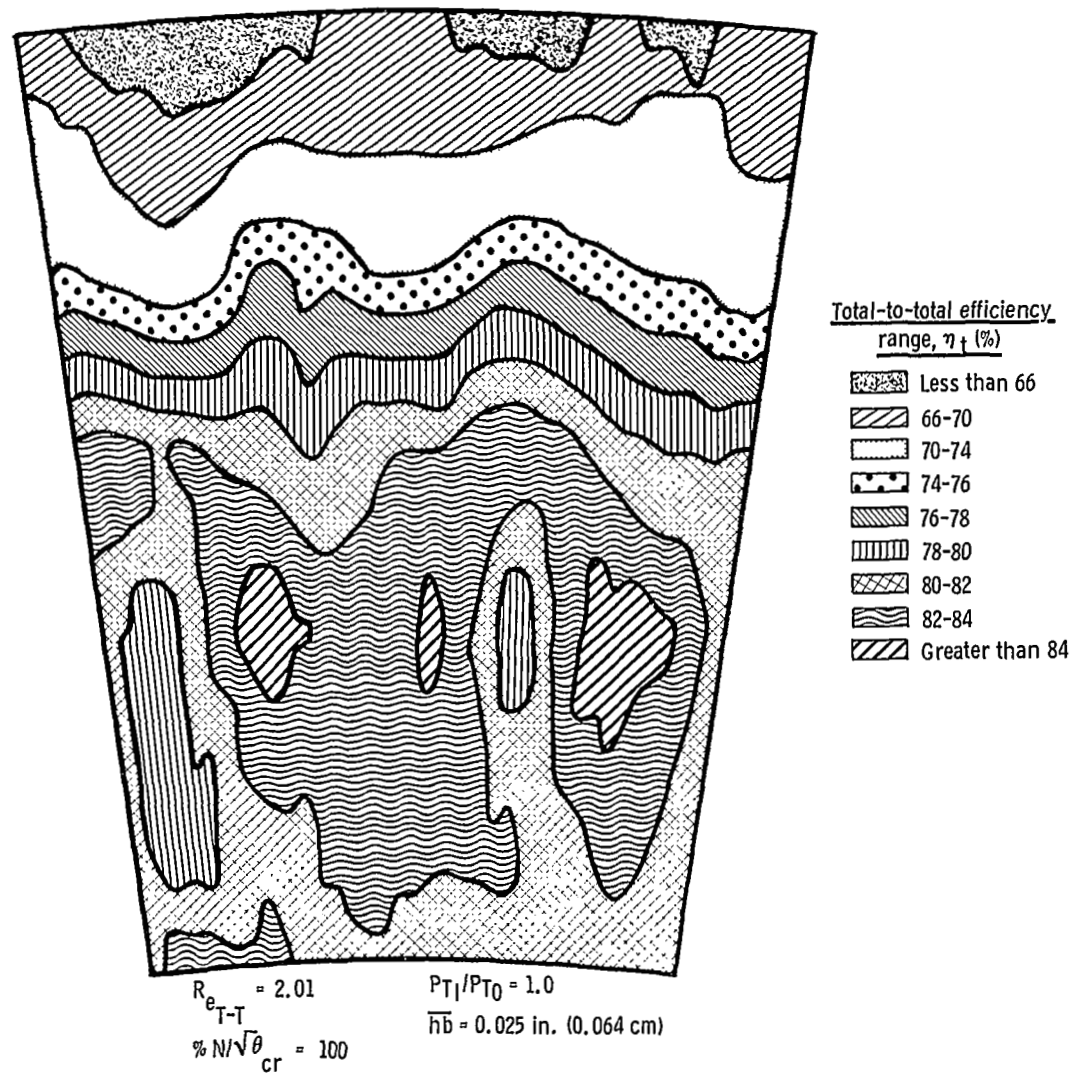


Figure 61. Total-to-total efficiency contours—100% speed, $R_{e_{T-T}} = 2.01$.

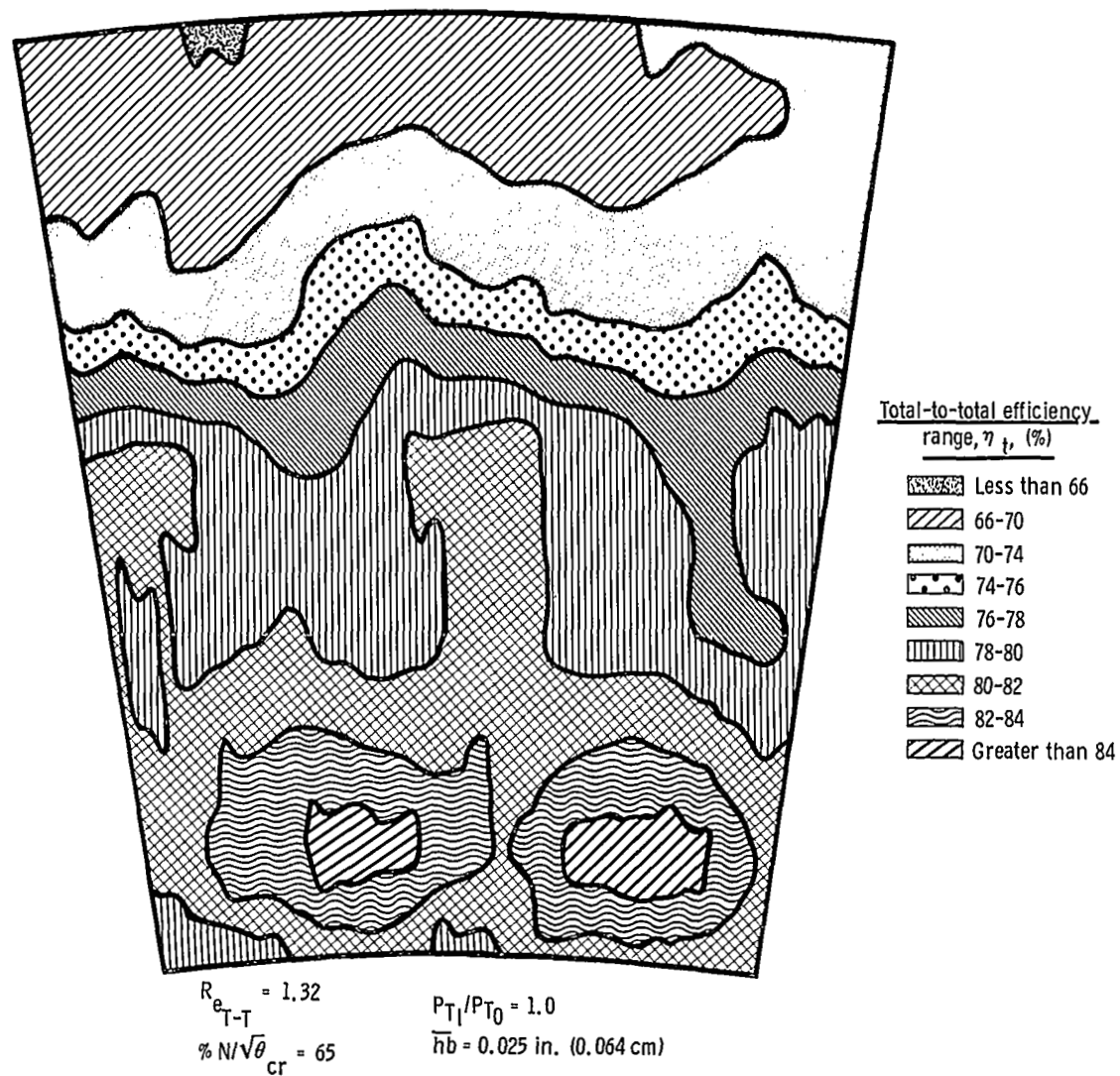


Figure 62. Total-to-total efficiency contours—65% speed, $R_{e_{T-T}} = 1.32$.

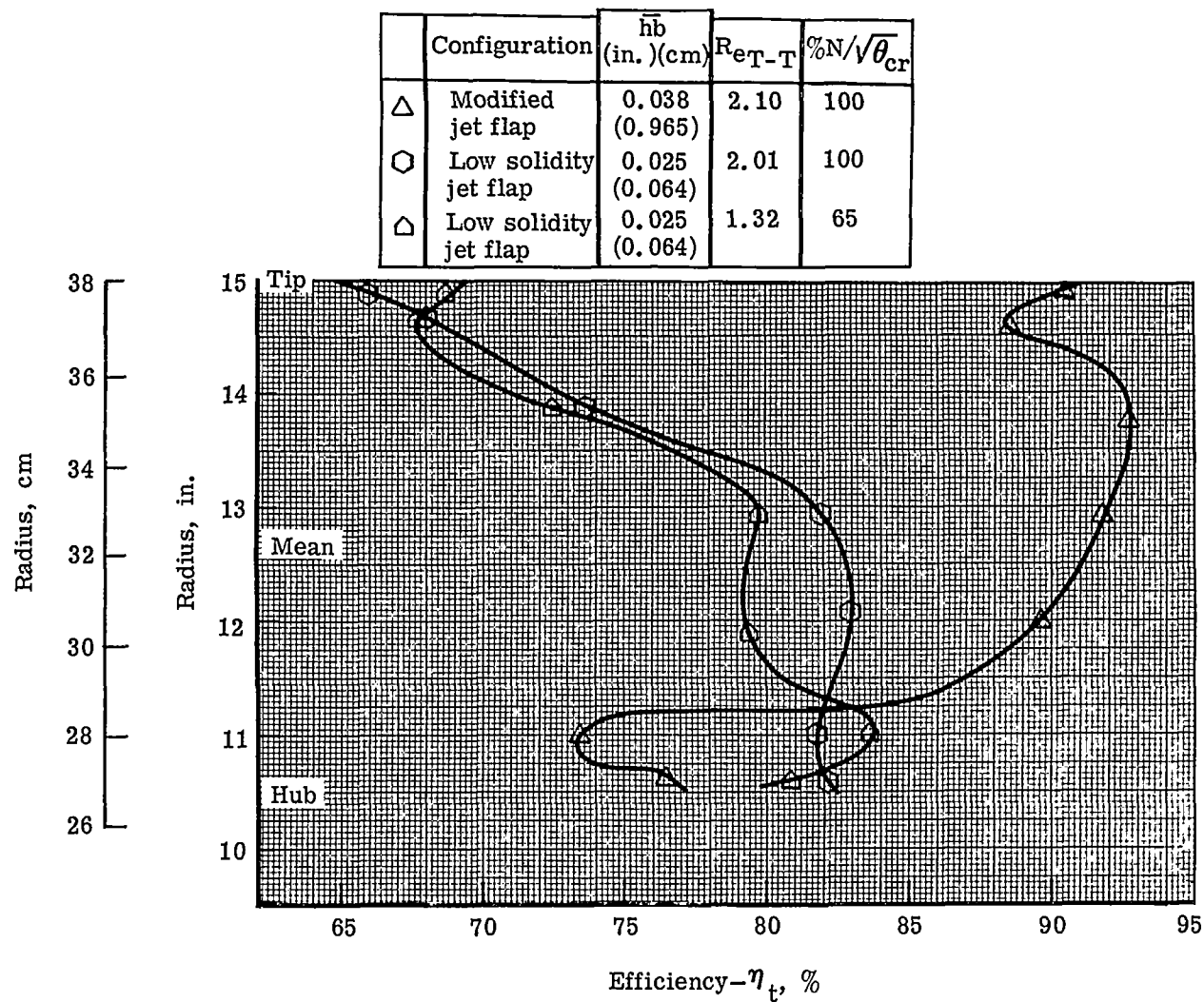


Figure 63. Comparison of efficiency (based on temperature) for the modified and low solidity jet flap turbines with $P_{T1}/P_{T0} = 1.0$.